IMPACT DAMAGE ASSESSMENT OF SANDWICH COMPOSITE MATERIALS USING NON-DESTRUCTIVE TECHNIQUES

By

TENDAI CHIPANGA

Thesis submitted in fulfilment of the requirements for the degree

Doctor of Engineering: Mechanical Engineering

in the Faculty of Engineering and the Built Environment (FEBE)

at the Cape Peninsula University of Technology

Supervisors: Prof Jasson Gryzagoridis and Dr Ouassini Nemraoui

Co-supervisor: Dr Fareed Ismail

Bellville Campus, Cape Town

December 2024

DECLARATION

I, Tendai Chipanga, declare that the contents of this thesis represent my own unaided work, and that the thesis has not previously been submitted for academic examination towards any qualification. Furthermore, it represents my own opinions and not necessarily those of the Cape Peninsula University of Technology.

Signed

23/12/2024

Date

ABSTRACT

Impact damage in sandwich composite structures is a prevalent concern due to their inherent vulnerability to even low-velocity impacts, which forms the central focus of this study. In critical sectors such as aerospace, marine, automotive, and civil engineering, early identification of damage mechanisms is essential to prevent premature structural failure during service. Sandwich composites are widely employed for their advantageous combination of lightweight construction, high strength, energy absorption, and durability. However, their susceptibility to impact damage, particularly barely visible impact damage (BVID) poses significant challenges, as such damage may not be detectable through visual inspection yet can severely compromise structural integrity.

The anisotropic nature of composite materials further complicates their response under service loads, making their behaviour under impact conditions difficult to predict. The absence of comprehensive characterisation data tailored to specific composite configurations and applications necessitated this investigation.

This study examines the low-velocity impact response and damage tolerance of sandwich composites fabricated via the autoclave process. A detailed damage assessment was conducted on specimens comprising glass fibre-reinforced polymer (GFRP) and carbon fibre-reinforced polymer (CFRP) face sheets, with a polyvinyl chloride (PVC) foam core. Initial mechanical testing was performed to determine key material properties relevant to impact performance.

Subsequent impact testing was carried out to evaluate damage behaviour under low-velocity conditions. Damage mechanisms were characterised using X-ray micro-computed tomography (micro-CT), a non-destructive technique that revealed matrix cracking, intra-laminar and inter-laminar delamination, fibre breakage, foam shearing, and densification across varying impact energy levels. BVID was shown to significantly reduce residual strength, thereby undermining structural integrity. ImageJ software was employed to validate the quality of the reconstructed CT images.

To complement the experimental findings, a numerical study was conducted using nonlinear finite element (FE) analysis in Abaqus, integrated with a Fortran compiler. The computational framework incorporated a user-defined material subroutine (VUMAT) implementing 3D Hashin failure criteria. Notably, this study extended existing modelling approaches by integrating both ductile and shear damage into the PVC Crushable Plasticity model, an enhancement not commonly addressed in prior work.

The inclusion of ductile damage enabled the simulation of progressive stiffness degradation due to plastic deformation, while shear damage was critical for capturing delamination and core-skin debonding phenomena. The foam core's post-yield behaviour prior to densification was effectively represented through ductile damage modelling, and shear damage accounted for sliding and tearing effects.

Comparative analysis between experimental and numerical results demonstrated strong agreement in terms of failure patterns, load histories, and energy absorption characteristics. These findings provide a valuable framework for evaluating and optimising newly developed composite materials for diverse engineering applications. Furthermore, the developed FE modelling approach contributes to the advancement of generalised methodologies for simulating deformation and failure in sandwich composite structures.

Keywords: sandwich composites, failure mechanisms, low-velocity impact, barely visible impact damage, finite element analysis, 3D Hashin failure criteria, damage tolerance, crushable plasticity, ductile damage, shear damage, autoclave manufacturing

ACKNOWLEDGEMENTS

I wish to thank:

God who predestined before the foundations of this world that I would undertake this research and providing the resources and means to do so. My knowledge that You, God was present even in dark moments propelled me to remain resolute despite many challenges faced during the execution of this research. I am forever indebted to You. Honour and Glory be given back to You.

My late supervisor Professor Jasson Gryzagoridis for his outstanding guidance and insights. Your premature departure on earth could not allow you to witness the final closure of this research project we started together. However, I am forever indebted to your contributions and belief in me to contribute to the body of knowledge.

A special thanks to supervisors Drs Nemraoui and Ismail for ensuring that this thesis was completed despite the many huddles we faced. Dr Nemraoui, your great efforts in ensuring that all the required documents were provided timeously is greatly appreciated.

The Director of Centre for Materials Engineering (CME) Prof Rob Knutsen at University of Cape Town (UCT) for allowing me to use their lab to do some of the experimental work. I want to also thank Penny Louw for her assistance with machine set up and testing.

The Central Analytical Facilities (CAF) at University of Stellenbosch headed by Prof Anton du Plessis for facilitating X-ray micro-computed tomography tests. My special thanks go to Muofhe Tshibalanganda and Carlyn Wells who were on the ground to assist with the actual tests.

Mr Hellmut Bowles who assisted me with debugging some of the numerical simulation errors. Your efforts are greatly appreciated.

My family for their supportive role. Your encouragement and patience to allow me time to undertake this research is sincerely appreciated.

The partial financial assistance of the University Research Grant (URF) is acknowledged. Opinions expressed in this thesis and the conclusions arrived at, are those of the author, and are not attributed to the funder.

DEDICATION

I dedicate this work to my loving wife Unity, our late son Marvellous Anashe, son Makatendeka Theophilus and daughter Tiffany Mutsawashe.

RESEARCH OUTPUTS

The following research outputs are contributions by the candidate to scientific knowledge and development on the specific research project during its execution.

1. Tendai Chipanga, Jasson Gryzagoridis, Low Velocity Impact Damage Assessment on Sandwich Type Composite Materials. Peer-reviewed-Extended Abstract presented at South African Institute of Mechanical Engineers (SAIMechE) Central Branch Mechanical Engineering Post Graduate Student Conference, 2018. Unpublished.

2. Tendai Chipanga, Jasson Gryzagoridis, Experimental Investigation and Computation of Flexural Modulus of CFRP Composite Specimens Using Two Loading Configurations. *Journal: AIP Conference Proceedings*,
AIP Conf. Proc. 2933, 020013 (2023).
https://doi.org/10.1063/5.0174639

3. Tendai Chipanga, Ouassini Nemraoui, Fareed Ismail, Damage Assessment of Low-Velocity Impacted Sandwich Composite Structures Using X-ray Micro-Computed Tomography, *Journal of Engineering*, vol.2024, Article ID 6147948, 2024.
http://doi.org/10.1155/2024/6147948

4. Tendai Chipanga, Ouassini Nemraoui, Fareed Ismail, “Quasi-Static Flexural Behaviour of PVC Foam Core Sandwich Composite Structures”. Peer-reviewed-Extended Abstract presented at South African Institute of Mechanical Engineers (SAIMechE) Central Branch Mechanical Engineering Post Graduate Student Conference, 2024. Unpublished.

TABLE OF CONTENTS

LIST OF FIGURES

LIST OF TABLES

LIST OF APPENDICES

GLOSSARY

Terms/Glossary	**Definition/Explanation**
Anisotropic	material properties at a point that vary with direction in which they are measured and with no specific number of axes along which the properties must differ.
Areal weight	weight of reinforcement material for a given area.
Orthotropic	type of material that has unique and independent mechanical properties along the three mutually perpendicular axes.
Damage resistance	measure of the ability of sandwich structure to resist damage when subjected to a foreign body.
Damage tolerance	measure of the ability of a sandwich structure to perform satisfactorily with impact damage and without reparation.
Emissivity	the ratio of energy radiated from a material's surface to that radiated from a perfect emitter or blackbody observed at the same temperature and wavelength.
Fabric crimp	measure of the yarn waviness.
Fabric drapeability	ability to conform to shapes.
Fibre volume fraction	the ratio of the cross-sectional area of the fibre to the total cross-sectional area of the unit cell and is denoted by V^f.
Matrix volume fraction	the ratio of the cross-sectional area of the matrix to the total cross-sectional area of the unit cell and is denoted by V^m .
Macromechanics	the study of composite material behaviour wherein the material is assumed to be homogenous, and the effects of the constituent materials are detected only as averaged apparent properties of the composite material.
Micromechanics	the study of composite material behaviour wherein the interaction of the constituent materials is examined in detail as part of the definition of the behaviour of the heterogeneous composite material.
Impact factor	the ratio of the maximum dynamic deformation to the static deformation.

Prepreg	contracted and common term for fabric material pre-impregnated with a resin system.
Strain energy release rate	rate of energy release as crack grows. If this rate of energy release is greater than the critical strain energy release rate of the material, the crack will grow catastrophically.
Warp	is the longitudinal direction of the fabric or laminate.
Weft or Fill	the transverse direction of the fabric or laminate.

ABBREVIATIONS AND ACRONYMS

ASTM	American Society for Testing and Materials
BVID	Barely Visible Impact Damage
CFRP	Carbon Fibre Reinforced Polymer
CT	Computed Tomography
DWT	Drop Weight Testing
FDD	Focus to Detector Distance
FE	Finite Element
FEA	Finite Element Analysis
FEM	Finite Element Method
FOD	Focus to Object Distance
FRC	Fibre Reinforced Composite
GFRP	Glass Fibre Reinforced Polymer
IT	Infrared Thermography
K.E	Kinetic Energy
LVID	Low Velocity Impact Damage
NDE	Non-Destructive Evaluation
NDI	Non-Destructive Inspection
NDT	Non-Destructive Testing
P.E	Potential Energy
PVC	Polyvinyl Chloride
SHM	Structural Health Monitoring
TTU	Through Transmission Ultrasonic

UT	Ultrasonic Testing
VID	Visibly Impact Damage

CHAPTER 1
INTRODUCTION

1.1 Background of the Research Problem

Composite materials' usage is fast taking over from the traditional or conventional materials in many industries such as marine, aircraft, water and sanitation, oil, and gas, to mention just a few. Thus, the applications' areas are wide-ranging, including shipbuilding, machine building, transportation, and construction. The benefits derived from using composite materials include lightweight, high specific strength and stiffness, superior corrosion, and outstanding thermo-mechanical properties. However, because composites are brittle, their main disadvantage is that they are vulnerable to low-energy impacts, which may cause internal damage (D. H. Li et al., 2014). Despite the advantages offered by sandwich composites, comprehensive studies are still necessary to understand their behaviour and the complex mechanisms involved under impact conditions commonly encountered in practical applications (Y. Chen et al., 2017).

In general, impact damage is undesirable when using composite materials due to the type of failure modes that occur, such as matrix cracking and skin core delamination. It becomes even more undesirable when invisible damage is inflicted on the composite structure during service, as in the case of low-velocity impact (Katunin et al., 2015).

Low-velocity impacts can be practically induced in composites in many ways, such as dropped tools during servicing or routine maintenance work, hailstorms, birds in the case of space-moving objects and vehicles, transportation, and handling before installation, and also during installing parts or components either as standalone or in assembly (Jang & Kim, 2017). Low-velocity impact, as has been described by many researchers, causes Barely Visible Impact Damage (BVID). Many studies focussed BVID on laminates. However, the contribution of this work is on sandwich composite structures. Sandwich composite structures have the additional benefit of having customisable material properties for the face sheet and core. Thus, the face sheet and core materials can be tailored to meet specific performance requirements such as thermal conductivity, acoustic insulation, and impact resistance. It is, therefore, evident that composite materials require inspection at various stages during their life to derive maximum benefits from their use. Thus, composite components should uncompromisingly meet the quality test during manufacturing, transportation, and handling during installation. Decisions pertaining to the structural integrity of the components are made based on information obtained from relevant non-destructive testing methods.

1.2 Statement of the Problem

Detecting low-velocity impact damage in composite sandwich structures remains a significant challenge, particularly when relying on visual inspection. Such damage is often subtle or invisible on the surface, yet it can critically undermine the structural integrity of the material. These hidden defects pose serious risks in safety-critical applications, such as aerospace, marine, and automotive engineering, where reliability is paramount.

Effective and consistent methods for detecting and evaluating impact damage are essential to ensure the continued performance and safety of these structures. However, current techniques often fall short in fully characterising the complex failure mechanisms that occur during impact events. A comprehensive understanding of damage progression, from initial impact to complete penetration, is necessary to optimise material usage and extend service life.

One of the key limitations in current research is the lack of detailed insight into the simultaneous occurrence of multiple failure modes, such as delamination, core crushing, and face sheet cracking. Additionally, the interfaces between dissimilar materials within the sandwich structure are particularly sensitive to stress concentrations, which can accelerate damage propagation. These complexities make it difficult to apply a universal approach to damage detection and modelling.

To address these challenges, an in-depth investigation is required to bridge the existing knowledge gap. This includes developing or selecting advanced inspection methodologies and robust damage progression models that can accurately capture the intricate behaviour of sandwich composites under impact loading. Such advancements will contribute to improved structural efficiency, enhanced damage tolerance, and extended operational lifespans of composite structures in demanding environments.

1.3 Impact Damage

Impact is defined by Razali et al. (2014) as the collision between two or more bodies, where the interaction between the bodies can be elastic, plastic, fluid, or a combination of these. According to Phadnis et al. (2016), low-velocity impact occurs when the contact duration of impact is longer than the time period of the lowest vibrational mode of the structure. Robinson and Davies (1992) define low-velocity impact as one in which the through-thickness stress wave plays no significant part in stress distribution. Topac et al. (2017) state that velocities between 1 to 10 ms^{-1} are considered low. Ahmed & Wei (2015) concur that low velocity is considered up to 10 ms^{-1}. Safri et al. (2018) also state that low-velocity impacts occur at a velocity below 10 ms^{-1} and further categorised immediate impacts to occur between 10 ms^{-1} to 50 ms^{-1}, high-velocity (ballistic) impacts between 50 ms^{-1} to 1000 ms^{-1} and hyper velocity impacts to have a range of 2 kms^{-1} to 5 kms^{-1}. Razali et al. (2014) mention that there are four general types of impact damages, namely low (<11 ms^{-1}), high (> 11 ms^{-1}), ballistic (> 500 ms^{-1}) and hyper velocity (> 2000 ms^{-1}). This categorisation differs from what was proposed by Safri et al. (2018) and can be a potential source of error when determining energy absorption levels for various impact damage regimes. In this study, a low-velocity range of 1 to 10 ms^{-1} will be considered in the analyses.

Xu & Chen (2013) mention that low velocity impacts cause matrix cracking delamination and breakage of fibres of composites. According to Sánchez-Sáez et al. (2008), composites are sensitive to accidental damages, and there is a significant loss of strength of up to 40% due to low-velocity impacts. The difference between ballistic and low-velocity impacts is that in the former, the damage is localised and clearly visible, while in the latter, because it involves a long contact time between the impactor and the target, produces global structural deformation with undetected internal damage at points far from the contact region (Farooq & Gregory, 2009).

There is consensus among researchers that many factors influence the response of composites to impact. For example, Qiu et al. (2014) mention that these factors are fibre orientation, layup sequence, geometry of composites, indenter shape and impact energy.

Olsson (2000, 2003) concluded that small-mass impactors cause higher impact loads and earlier damage initiation than large-mass impactors with the same kinetic energy. Thus, at the same impact energy, large mass impacts are governed by a quasi-static impact response, while small mass impacts are governed by a wave-controlled response. He also showed that short impact times result in a response governed by wave propagation. In summary, the response is governed by the mass ratio between the impactor and the component in addition to the impact velocity.

Damage inflicted on composite structures can be evaluated by different non-destructive methods. However, there is no “one-size-fits-all” as far as the use of these methods is concerned. The choice of a particular method is based on several factors, such as the type of composite, the nature of the damage and the geometries of the structures. Thus, selecting better and more efficient methods of undertaking damage assessment for different applications warrants further research. Gryzagoridis et al. (2011) acknowledge that most testing methods deal with identifying and locating the presence of defects but are unable to further characterise these defects in terms of depth.

This study will employ Infrared Thermography (IT) and X-ray micro-computed tomography (X-ray μ-CT) non-destructive testing methods to better characterise the defects inflicted by low-velocity impacts. Better characterisation of defects will assist in improving the effectiveness of damage models for low-velocity impact regimes. Furthermore, service life management of critical components is imperative if catastrophic disasters are to be minimised. To this end, in critical industries such as aerospace, the development of fully fledged structural health monitoring systems (SHM) is now a requirement.

The research methodology processes adopted in this study are illustrated in Figure 1.1.

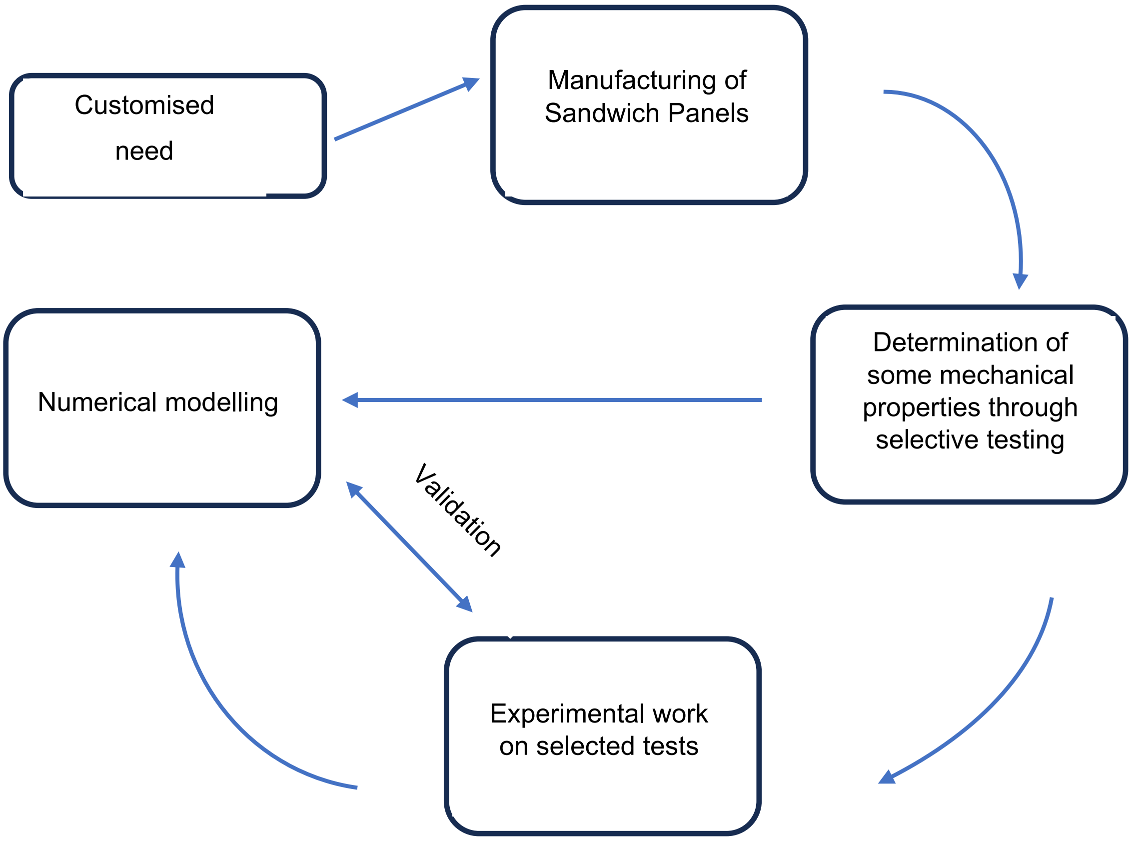

Figure 1.1: Adopted research methodology processes

1.4 Delineation of the Research

- Only low-velocity impacts will be covered as opposed to ballistic and hypervelocity impacts.
- Transverse loading is assumed for experimental and numerical analysis purposes, although impacts are sometimes random.
- Use of NDT techniques for manufacturing quality control is not covered since all the manufacturing of the specimens was outsourced. However, for purposes of promoting quality results, the specimens were inspected for flaws before specific and desired tests were conducted.
- Tests will be done on sandwich composites with carbon fibre-reinforced polymer (CFRP) and glass fibre-reinforced polymer (GFRP) facings/ skins and closed-cell polyvinyl chloride foam core.

1.5 Research Questions

1. Is it possible to quantify the amount of damage inflicted upon the composite (sandwich type) structure due to low-velocity impact?
2. Is it possible to determine how the presence of defects in (sandwich-type) composite materials affect their performance?
3. Can any non-destructive method fully characterise the presence of low-velocity impact damage induced on sandwich structures?

1.6 Objectives of the Research

1. To detect BVID induced by low-velocity impacts on sandwich-type composites.
2. To characterise the type, position, and size of the defects beneath the surface.
3. To quantify the amount of damage inflicted on the components.
4. To predict damage initiation and progression through modelling.

1.7 Layout of the Thesis

The layout of this thesis is as outlined below:

CHAPTER ONE: This chapter outlines and presents the background and motivation of the research, statement of the problem, research aim and objectives, research questions and delineation of the study.

CHAPTER TWO: This chapter focuses on the literature regarding sandwich composite materials, with particular emphasis on impact damage, impact response and potential non-destructive evaluation techniques for assessing impact damage on sandwich composite structures. Parameters and factors that could potentially affect the performance of sandwich composite structures are covered.

CHAPTER THREE: This chapter discusses the manufacturing processes adopted to produce the panels that were later cut into coupons to undertake different tests. The respective experimental setups are for quasi-static three point bending and drop weight impact tests.

CHAPTER FOUR: This chapter details the three-point bending test results for purpose of determining the flexural moduli and the compressive strength of the respective specimens. The flexural experimental and analytical data are compared to validate the results. Furthermore, the chapter also presents analyses of the results of the drop weight impact tests and damage assessment of the impacted specimens using X-ray micro-computed tomography. The identification of damage mechanisms especially for barely visible impact damage are presented. The damage evolution from indentation to full perforation is presented to show the severity of damage and the associated damage mechanisms.

CHAPTER FIVE: This chapter provides information on modelling of the impact damage phenomenon. The computational Abaqus finite element (FE) framework implemented the 3D Hashin Failure Criteria through user-defined material subroutine. The procedure of linking Abaqus to the Fortran Compiler is provided. Inputs, modelling procedures, results, discussion and validation of the results are covered.

CHAPTER SIX: This chapter contains the summary of the research, recommendations and the future studies linked to this research.

APPENDICES: All raw data and supplementary results are contained in this section, and relevant in-text references are provided in the respective thesis chapters.

REFERENCES: All sources of information for the search are presented under this section in corresponding chapters. The information is presented in a reference format as stipulated by the thesis institutional requirements.

1.8 Conclusion

The background to the research problem has been outlined, and the research objectives have been stated. The research questions that seek to guide the overall study and its delineation are stated.

The next chapter will present a review of the literature on sandwich composite materials, including relevant non-destructive testing techniques that are used to carry out damage assessment on these structures.

CHAPTER 2
LITERATURE REVIEW

2.1 General Characterisation of Sandwich-Type Composite Materials

Composite materials may either be classified as matrix or reinforcement-based. For structural applications, E-glass, carbon, aramid, and boron, in that order of importance, are the polymer matrix composite reinforcing fibres used (Mostafa et al., 2017). The structural reinforcement composites, in particular the sandwich composites, are of interest in this study. The sandwich composites are a subdivision of structural composites, as depicted in Figure 2.1.

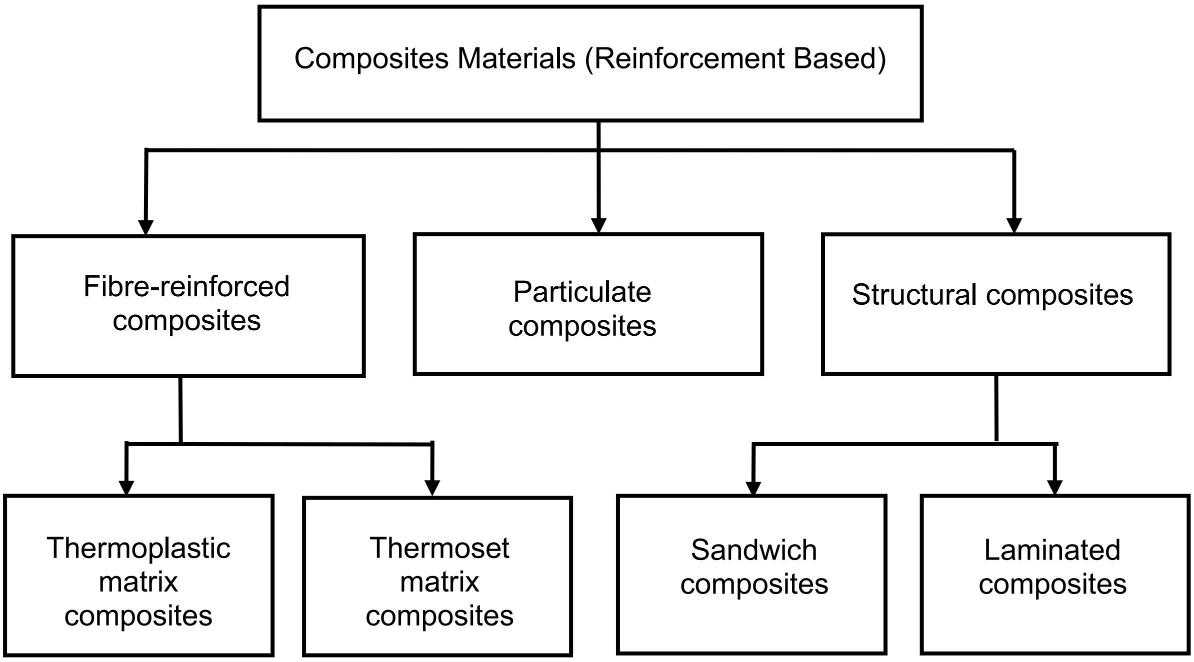

Figure 2.1: Reinforcement-based composite classification

Source: Ibrahim et al. (2015)

Sandwich structures are now manufactured and designed to offer better mechanical performance, stability, and weight savings than traditional structural configurations. Sandwich composite materials belong to the group of anisotropic materials (Krzyzak et al., 2016). In other words, the elastic properties are different in all directions at a point in the material body. As such, careful analysis is required when dealing with these materials under in-service loads.

2.2 Sandwich Structures

Sandwich composites consist of two thin face sheets or skins with high stiffness and strength and a core with low density and low stiffness (Freeman et al., 2005). (Birman & Kardomateas, 2018) define sandwich structures as "a subset of multi-layered composite structures, optimised for the anticipated lifetime loading conditions". The skins take up bending stresses and, at the same time, provide a hard-wearing surface, while the core takes up the shear stresses induced in the structure. Gryzagoridis et al. (2015) mentioned that "a sandwich structure is fundamentally designed to ensure that it possesses sufficient shear and flexural rigidity to prevent failures due to large deflections due to excessive applied loads". The increased use of sandwich structures for engineering purposes is continuing to direct research studies toward finding better solutions in dealing with the poor resistance of these structures to impact loads. The vulnerability of sandwich materials under impact loading is influenced by the properties of the face sheets, the core structure, and the integrity of the skin-core interface (Constantin et al., 2017).

The cores of sandwich structures are usually honeycomb, balsa and foam. The honeycomb sandwich structures are widely used in areas ranging from aerospace to household applications (D. H. Chen, 2011). According to Akatay et al. (2018), honeycomb sandwich structures in recent years have attracted considerable interest as advanced composite materials that satisfy the high-performance requirements of machine design. (Pathipaka et al., 2020) employed 3D printing technology to fabricate a honeycomb core structure, aiming to explore its potential applications in critical sectors such as aerospace and automotive industries. The balsa core is commonly used in the marine industry for boats' hulls and decks. The work of (Cucinotta et al., 2016) focussed on the application of sandwich composite structures with carbon fibre reinforced polymer (CFRP) face sheets and PVC foam core for racing boats subjected to repeated impacts. Foam cores are used in various applications to enhance the overall composite product. A drop weight impact test conducted by (Ude et al., 2013) on sandwich structures with natural silk/epoxy face sheets showed that foam core specimens achieved the highest energy absorption compared to those with core mat and honeycomb cores. The focus of this study will be on foam cores.

2.2.1 Characterisation of constituents of sandwich structures for this study

The overall performance of sandwich structures depends on the material properties of the constituents (facings, adhesive and core), their geometric dimensions and the type of loading (Gdoutos & Daniel, 2004). Different unique structural designs are now used for various applications.

Facings/Face sheets/skins – usually should be strong and lightweight with a high elasticity modulus. This study will use facings made from carbon fibre reinforced polymer (CFRP) and glass fibre reinforced polymer (GFRP). It has been noted from the literature that S-glass skins exhibit better impact toughness (Avilés et al., 2011). On the other hand, the S-glass face sheet has relatively low fatigue resistance and, therefore, is not recommended for use in fatigue-prone applications.

Adhesive – the urgent need for adhesives in composite structures resulted from further reducing weight imposed by mechanical fasteners. Furthermore, the fasteners create stress concentration at joint areas and initiate complex damage, weakening the composite structure (Singhal et al., 2017). Ehrhart et al. (2013) concur and mention that "a structure assembled with adhesive bonding benefits from homogenous stress distribution". Other than noting that adhesive bonding will gain more use in future because of the benefits it offers, it is not the intention of this study to look at different available adhesives currently in use for composite structures, let alone the mechanics of adhesion, which is attracting interest for further research.

Core – According to Zhou et al. (2006), "core materials substantially affect damage initiation characteristics because they have lower mechanical properties than skins due to their lower density". The core is usually lightweight and thick with a low modulus. As previously mentioned, this study will focus on the foam cores. Generally, the honeycomb core is used where impact resistance is of paramount importance. Dear et al. (2006) mention that in cases where honeycomb is used in large structures, impact damage and toughness are of primary concern. According to Yamashita and Gotoh (2005), the honeycomb structures can be used as shock absorbers in impacted objects. This is usually accomplished through stiff and strong face sheets and deformable cores. Different materials used for honeycomb cores are aluminium, thermoplastic, aramid or Nomex. In the aerospace industry, aluminium and Nomex honeycomb cores are usually used, while the core for civil engineering applications is often closed-cell or open-cell foam. As previously stated, the balsa core is normally used for ship construction. Figure 2.2 shows the nomenclature of a sandwich structure with the core which can either be foam or honeycomb.

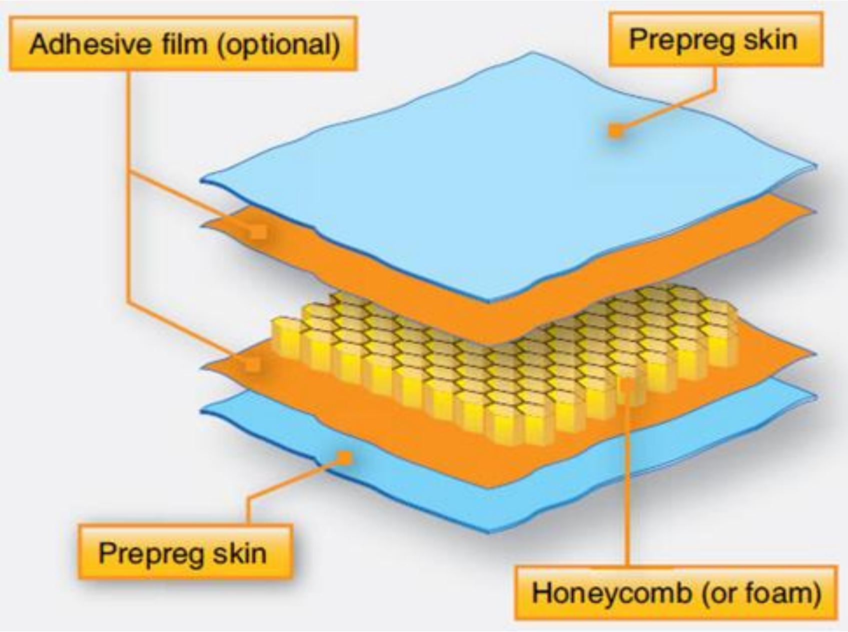

Figure 2.2: Nomenclature of Honeycomb Sandwich Structure

2.2.2 Response of Sandwich Structures to Low-Velocity Impact

Since the material constituents and geometries of the sandwich structures are different, their responses are likewise different. Factors such as panel support conditions and projectile nose shape affect the damage initiation of these structures (Foo et al., 2008).

Anderson and Madenci (2000) cited the work of Rhodes (1975) using graphite and Kevlar honeycomb sandwiches to have revealed that significant internal damage is achieved at impact levels lower than those required to create visible damage. Other researchers later confirmed this finding.

Foo et al. (2008) mentioned that core damage is characterised by a substantial change in the load-deflection curve identified as the first failure mode in low-velocity impacts of honeycomb sandwich structures with a high skin-to-core ratio.

2.2.3 Damage on Sandwich Structures

It is important to note that the damage inflicted on the structure, localised or global, will affect the structural integrity. The level of damage infliction is usually measured by two key indices, namely, damage resistance and damage tolerance. In this regard, damage resistance is a measure of the ability of a sandwich structure to resist damage when subjected to foreign body impact. In contrast, damage tolerance is a measure of the ability of a sandwich structure to perform satisfactorily with impact damage and without reparation (Chai & Zhu, 2011). The authors further acknowledge that work or research on damage evolution is still in its infancy.

Damage resistance

Damage resistance is concerned with creating damage due to a specific impact event (Tomblin et al., 1999). The authors identify variables such as the material and layup of the face sheet, the type and thickness of the core material, and the boundary conditions of the sandwich structure as key in determining the damage resistance of sandwich structures. The structures with a higher resistance to impact experience less damage, while those with less resistance suffer more damage. Li et al. (2017) mention that the stiffness, strength, and stability determine the load-carrying capacity of sandwich structures. The stability of the structure is provided by the selected design to meet a specific application, while the strength will be mechanically tested upon manufacture. Stiffness or flexural rigidity on the other end is a function of the beam's ability to resist bending and deflection when subjected to service loads.

The resistance of the beam to damage and impact is related to the bending stiffness of the sandwich beam. For example, the bending stiffness of a symmetrical cross-section of a sandwich beam is given below:

$$E_x I = E_x^c I_c + 2E_x^f I_f \qquad (2.1)$$

Where E_x is the Young's Modulus of Elasticity and I_f and I_c represent the second moment of inertia of the face sheet and core, respectively.

Tomblin et al. (1999) mention that when damage occurs in a sandwich structure, its stiffness degrades, and the load capacity decreases significantly up to the final point of failure. Therefore, this study aims to understand damage from initiation to the point when a structure can be rendered useless or can no longer undertake the loads it was designed to carry.

Damage Tolerance

Damage tolerance involves the study of the behaviour of a damaged structure, while damage tolerance evaluation seeks to understand the extent and severity of the damage fully so that remedial action can be taken. It is a fact that damage inflicted on a structure affects its performance. According to Devivier et al. (2012), damage processes affect structural performance by reducing their stiffness, and the components can lead to premature failure. Stiffness reduction of about 80% in tension and up to 60% under compression was demonstrated by Sjögren et al. (2001) on small coupons cut from impacted zones. It can be noted here that although there is a consensus that stiffness reduction occurs due to damage inflicted on the structure, the percentage reductions are inconsistent. This is attributed to many reasons, including the different constituents that make up the structure, geometry, and loading patterns. Even though this work study focuses on BVID, decisions, such as immediate or later replacement after damage, are based on a comprehensively developed damage assessment system.

Furthermore, an attempt to understand the residual load-carrying capacity of a structure after damage requires a complete damage assessment procedure. The development of a damage assessment system includes integrating parameters that affect a structure's performance due to impact. Zenkert (2009) presents a generic damage assessment procedure for naval applications as follows:

i) Estimate the strength reduction caused by the damage or defect.
ii) Determine the allowable strength reduction based on the original design assumptions and operational envelope.
iii) Make comparisons of the above. If residual strength is smaller than the allowable value, consider the possibilities of restricting the operational envelope and/or accepting a lower safety factor until repair can be effected.
iv) If the above is insufficient, perform an emergency repair or take other necessary measures.

Notably, the development of a comprehensive damage assessment system is complex due to the different material constituents and their associated response to impact loading.

2.2.4 General classification of composite failure criteria

In their review work on composite failure criteria, Wicaksono and Chai (2013) illustrated the existing contributions of many researchers by classifying composite failure criteria into two types, namely mode-independent and mode-dependent. The mode-independent failure criteria are used to predict the damage and failure of the material without directly identifying the different failure modes. On the other hand, mode-dependent failure criteria are sets of criteria used to predict the damage and failure of material corresponding to each failure mode. The mode-independent failure criterion is further divided into polynomial and parametric as illustrated in Figure 2.3.

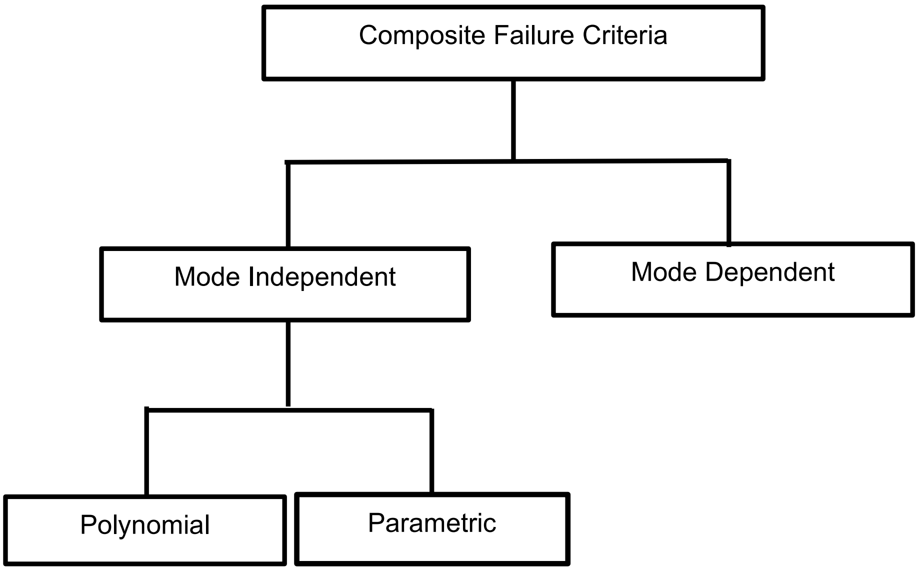

Figure 2.3: Composite failure criteria classification

Source: Wicaksono & Chai (2013)

2.2.5 Failure Modes of Sandwich Structures

Failure modes occur in sandwich structures because of bending, shear, and in-plane loading. (F. Zhu et al., 2010) report that the failure modes of sandwich structures subjected to low-velocity impact are like those of sandwich structures subjected to quasi-static indentation. Different failure modes identified by various researchers for low-velocity impact damage on sandwich panels with honeycomb cores are core buckling and debonding, core shear and cracking, delamination in the top face sheet, face sheet matrix cracking and fibre breakage in the facings. Richardson & Wisheart (1996) mentioned four modes of failure due to low-velocity impact: matrix failure (the cracking that occurs parallel to the fibres due to tension, compression, or shear), delamination (produced by inter-laminar stresses), fibre failure (in-tension fibre breakage and in-compression fibre buckling) and penetration (occurring when the penetrator completely perforates the impacted surface). The interactions of failure modes and the nonlinear and inelastic behaviour of material constituents make it difficult to analyse the stress states in these structures (Gdoutos & Daniel, 2004).

Concerning fracture mechanics, modes I, II and III are commonly used to describe the failure phenomenon. Mode I is concerned with the opening displacements of the crack faces and tensile stresses near the crack tip. Mode II describes the forward shearing of the contact faces, while Mode III shows the tearing action between two faces on one plane pulled in the opposite direction. These failure modes are illustrated in Figure 2.4.

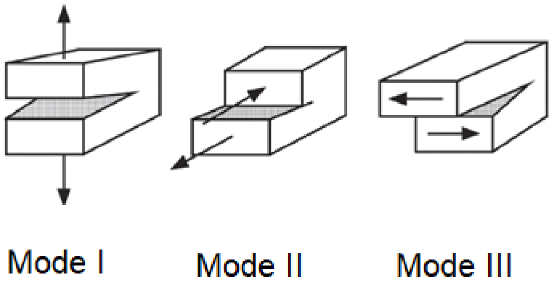

Figure 2.4: Fracture modes: Mode I – opening (in-plane separation), Mode II – sliding (in-plane shear), Mode III – tearing (out-of-plane shear).

Many researchers developed failure mode maps to provide design guidelines and ensure that optimisation is accomplished. This was done through experimental means, i.e., the three and four-point bending tests and formulations to limit associated damage modes. S. Zhu & Chai (2013) mention that failure mode maps allow for optimising energy absorption properties and load-carrying capacity with minimum weight to satisfy the quasi-static and impact loading requirement.

To this end, some researchers have adopted approaches to maximise cost and efficiency, among other parameters. Pioneer work by Ashby led to the development of Ashby charts named after him. The Ashby charts are useful to guide material selection for specific designs. The material properties used in constructing sandwich structures are important in this work. The skin thickness, t to core height, h ratio, $^{t}/_{h}$ ranges for different material combinations are useful to provide design guidelines for constructing sandwich structures. For example, some formulations to predict material efficiency regarding weight and cost are presented. Material efficiency per weight, $ME_w = \frac{E^{1/3}}{\rho}$ and material efficiency per cost, $ME_{CM} = \frac{E^{1/3}}{\rho C_w}$ (E as elastic modulus and ρ as material density). Figure 2.5 illustrates material efficiency per weight used to demonstrate the use of such charts in the choice of material properties used for the construction of sandwich structures.

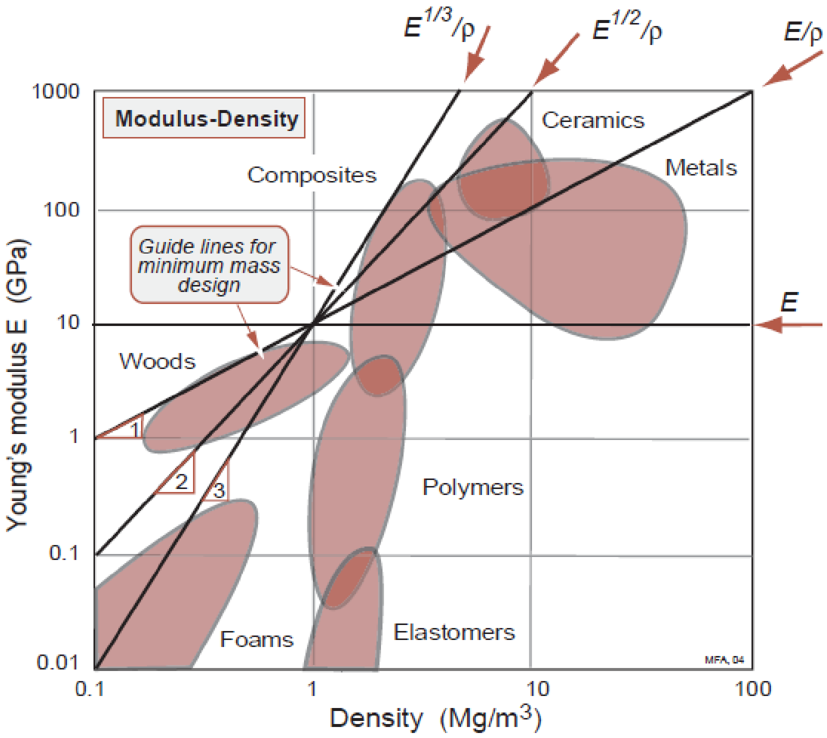

Figure 2.5: Material efficiency per weight, MEw

Source: Ashby & Ashby (2011).

2.2.6 Associated NDT techniques for assessing damage on sandwich structures

Many different NDT techniques are available, but not all can effectively characterise impact defects in sandwich structures. BVID may either propagate to a critical level and cause catastrophic failure due to repeated sinusoidal stress loading or remain latent until a structure fails. The purpose of this section is to review appropriate techniques for assessing impact damages in sandwich structures. The following techniques are reviewed for potential use in this study: Digital Shearography, Infrared Thermography, Ultrasonic C-scan, X-ray radiography, and X-ray micro-computed tomography (X-ray μ-CT).

2.2.6.1 Digital Shearography

Digital Shearography was successfully used by the author of this study to characterise defect-induced deformation anomalies on "shot peened" specimens (Chipanga, 2009). (Hung et al., 2013) define Shearography as a speckle interferometric technique providing full-field and quasi-real-time quantitative images of the surface displacements of a loaded structure. Thus, its capabilities include strain measurement, material characterisation, residual stress evaluation and vibration studies, to mention a few.

The measurement principle of the Shearography technique is that a laser light is illuminated on a surface under review, and a speckle pattern is formed that is imaged through a shearing device and stored in an image digitiser. The image of the object stored in the computer is compared with the damaged one. The comparison of the two images forms fringes that are superimposed on the image of the structure. The typical Digital Shearography setup is shown in Figure 2.6. The fringes represent lines of constant gradients or slope of out-of-plane displacements quantifiable by an expression: $\frac{\partial \delta p}{\partial x} = \frac{\lambda N}{2S}$ (Gryzagoridis et al., 2011) , where λ is the wavelength of the laser, N is the number of fringes observed, and S is the shear image imposed.

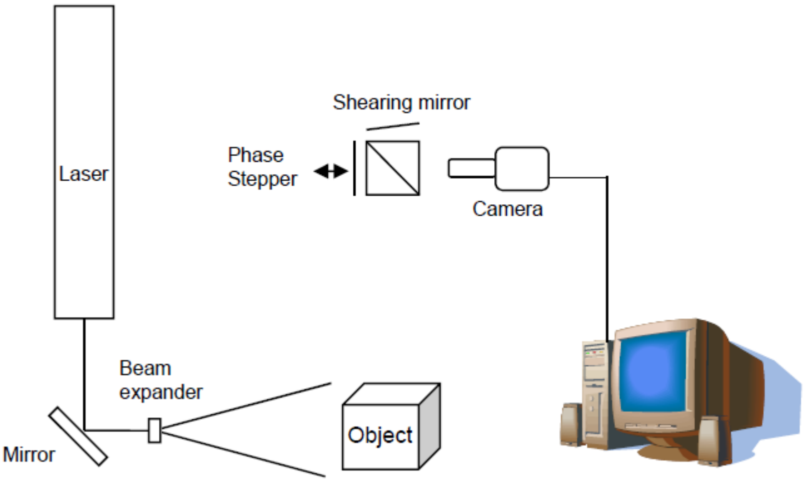

Figure 2.6: Typical laboratory Digital Shearography

Digital Shearography was proved to be capable of detecting delamination and other inhomogeneities in composite aerospace structures (Huang et al., 2007).

On the other hand, Růžek et al. (2006) used Digital Shearography to assess impact damage in sandwich panels, but it is unclear which type of cores were used in their study. The foam core influences the suitability of the damage assessment technique in describing the damage fully.

2.2.6.2 Infrared Thermography

Infrared thermography is divided into passive and active, as illustrated in Figure 2.7. Passive thermography does not use an external heat source and, therefore, relies on the differences in temperature of a part in operation and the ambient temperature of its surroundings. Thus, the possible change in ambient conditions makes this technique less accurate. The crack tips or stress concentration areas where heat accumulates and gets dissipated appear as hot spots on the thermal images. On the other hand, active thermography uses external heat sources, such as halogen lamps, lasers, flashes, infrared lights, and hot air jets, for active heat dissipation (Chrysafi et al., 2017). The infrared technique is based on the concept that all objects with a temperature above absolute zero emit infrared radiation at different wavelengths according to the black body radiation law.

It should be noted that applying an external heat source can be single or double-sided. The single-sided application is used where the other side of the part under inspection is not accessible, in which case the object will be heated, and afterwards, the scanner will be activated to record the heat distribution. In a double-sided application, the scanner and heat source are placed opposite each other, and heating and recording occur simultaneously (Dattoma et al., 2001). The advantage of double-sided application is that deeper defects can be detected.

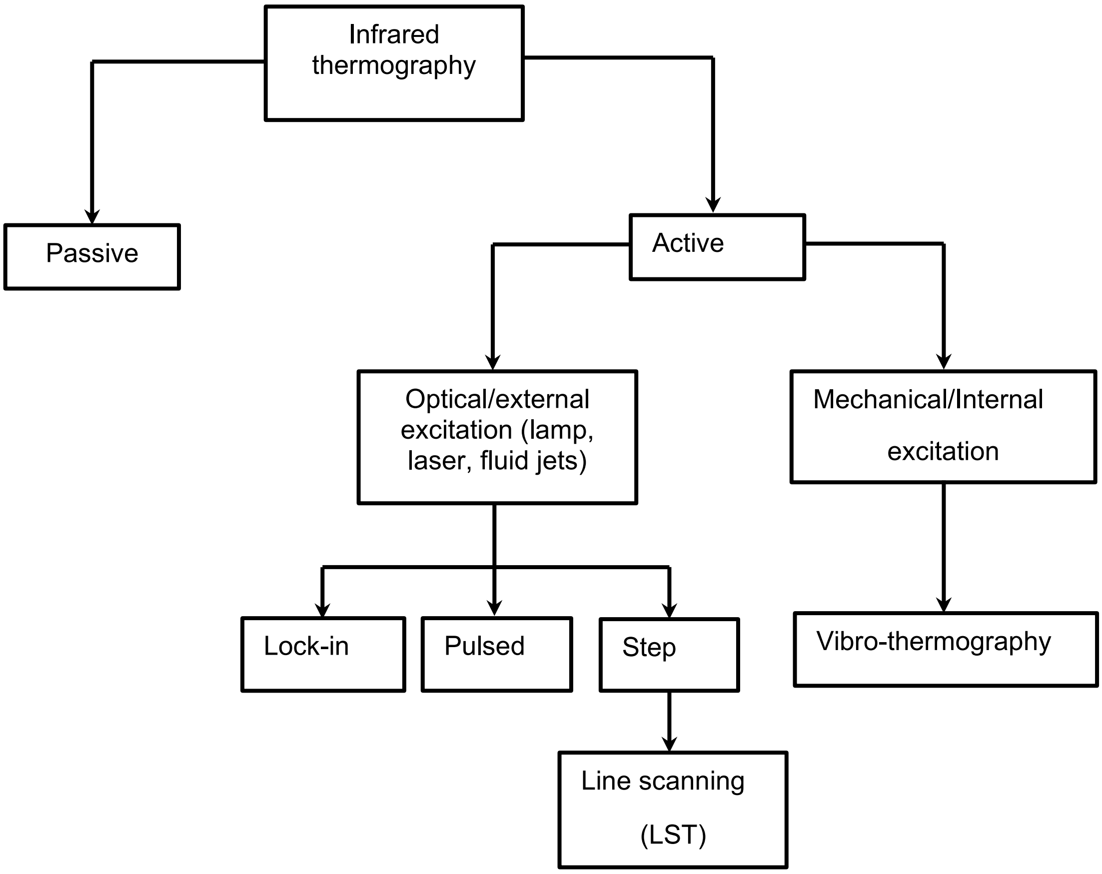

Figure 2.7: General classification of thermography techniques

Source: Ley & Godinez (2013)

Active thermography is divided into two forms of excitation: optical (external) and mechanical(internal). The common thermal stimulation techniques for optical excitation are pulsed (transient), lock-in (periodic heating) and step heating (long pulse). Although in most literature, step heating and long pulsed thermography are similar, (Almond et al., 2017) make a distinction between the two in that step heating technique data are measured during the application of the step-pulse, whereas in long pulsed technique, thermal signals are acquired during the cooling phase. Maierhofer et al. (2014) mention, among other excitation techniques, that flash lamps are used for pulse heating and halogen lamps are for periodic and step heating. A line scanning technique (LST) was developed as a dynamic thermography technique where a heat source and thermal camera move in tandem allowing the continuous scan of long surfaces without loss of resolution (Chung et al., 2011). Vibro-thermography is a "technique whereby the internal integrity and uniformity of materials and components are interrogated by observing the heat pattern produced by the dissipation which occurs when a specific vibratory excitation is applied to the test piece" (Reifsnider et al., 1980). Thus, the vibro-thermography technique monitors heat produced by damage under vibration and/or ultrasonic excitation.

It is important to note that further novel techniques with better characteristics are being developed, such as fast, accurate and reliable damage assessment in some wide range applications. This study uses active infrared thermography to detect latent subsurface defects in composite structures. Literature shows that infrared thermography was previously and successfully used for detecting flaws in composite laminates and honeycomb panels for skin-to-core debonding, face sheet delamination, honeycomb cell wall, core crushing and absence of adhesive (Ciampa et al., 2018). In the work of Xie et al. (2021), infrared thermography was used to assess damage on Paulownia wood core sandwich panels with GFRP face sheets.

2.2.6.3 Ultrasonic testing

Ultrasonic testing uses high frequency sound energy to conduct examinations and make measurements. The applications cover a wide range of tasks, including the detection of defects, material characterisation, and dimensional measurements. There are two approaches to ultrasonic testing, namely, pulse-echo and through transmission.

In the pulse-echo method, the transmitter generates an ultrasonic pulsed wave with a frequency of up to 50 MHz, reflected by an inhomogeneity, such as a defect or back wall of the test specimen or structure. The reflected wave is captured by the receiver and transformed into an electrical signal, which is then amplified and displayed on the screen. The relationship between wavelength, λ, frequency, f and velocity of sound, c is given by the expression $\lambda = c/f$. The waves generated can be longitudinal or transverse, and their sound velocities vary for different materials. The resistance of a material to the passage of sound waves (acoustic impedance) determines how much sound will be transmitted and reflected between two boundaries due to discontinuities. The acoustic impedance, Z, is the product of the density of the material, ρ and the sound velocity, c. The time of flight, t is given by double thickness, $2d$ divided by the sound velocity, c provides information to characterise the depth of the defect or flaw. In the pulse-echo arrangement, the transmitter and receiver are situated at one end for cases where the other side of the specimen is not accessible. On the other hand, through transmission ultrasonic (TTU), the transmitter and the receiver are placed on either side of the test piece that are accessible (Duchene et al., 2018).

The coupling can either be dry (thin foil of rubber) or liquid (water, oil, grease, glycerine). A good coupling liquid should have an acoustic impedance similar to the impedance to the test specimen, a high viscosity, and be non-corrosive and non-toxic. For cases of composites, water would be an appropriate medium, while the other coupling media would appeal to other materials.

The information from UT can be presented or displayed in different formats, i.e., the A-scan displays the amount of received ultrasonic energy as a function of time, the B-scan displays a profile view (cross-sectional) of the specimen, while the C-scan displays a plan view of the specimen and the discontinuities. According to Diamanti and Soutis (2010), the C-scan can produce sensitive measurements in relation to the location and size of damage inflicted on the structure.

Improvements made in the NDT space to address the shortcomings of contact transducers have given rise to laser ultrasonic techniques that use laser-generated ultrasound, which assist in producing highly sensitive measurements without using any coupling medium. The laser ultrasonic technique is a non-contact method developed to measure material thickness and detect and visualise damage in structures.

2.2.6.4 Comparisons of Digital Shearography & Active Thermography techniques

In a review of Digital Shearography and Active Thermography by (Hung et al., 2009), the authors compared the characteristics of the two techniques as presented in Table 2.1.

Table 2.1: Comparisons of Digital Shearography & Active Thermography techniques

Digital Shearography	***Active Thermography***
Full field	Full field
Non-contact inspection	Non-contact inspection
Measures mechanical deformation	Measures thermal radiation
Loading methods: Partial vacuum pressure, acoustic wave, and thermal shock excitation	Loading methods: long heating pulse, transient pulse excitation, and induction heating
Capture the speckle patterns for analysis	Capture a sequence of thermal images for analysis
Fringe pattern distribution in the stereographic image.	Anomalous "hot spots" deviated from the ideal flawless region and derivative value in thermal signal reconstruction (TSR) value
Qualitative and quantitative analysis through the density of the fringe pattern	Qualitative and quantitative analysis through temperature distribution and its transition time
Rigid-body movement influence	Material's surface thermal properties influence
Indication determined by contrast with flaw-free background	Indication detected by temperature contrast with the numerical value of derivative

Although UT cannot be easily and directly compared to Digital Shearography and active thermography, literature has shown its usefulness as an acceptable technique that can be used to characterise BVID in composite structures.

2.2.6.5 X-ray radiography

Conventional radiography uses a penetrating X-ray beam to scan the internal of the composite materials. The projection of the attenuation beam on an X-ray-sensitive film or a digital scanner forms a 2D image known as a radiograph. Radiography can detect mesoscale and macroscale damage in composite laminates, such as translaminar cracks and delamination (Rolland et al., 2017).

2.2.6.6 X-ray micro-computed tomography (X-ray µ-CT)

Compared to conventional radiography techniques, X-ray µ-CT relies on computerised reconstruction of a series of radiographs collected by rotating the sample at a controlled angular step (Duchene et al., 2018). The transformation of two-dimensional radiographic images into a cohesive three-dimensional dataset is facilitated through sophisticated algorithms. Within this dataset, each three-dimensional pixel, or 'voxel,' symbolises the X-ray absorption level at that specific point within the object, providing detailed insights into its internal structure. The schematic representation of the X-ray micro-computed tomography is shown in Figure 2.8.

Principle of Operation

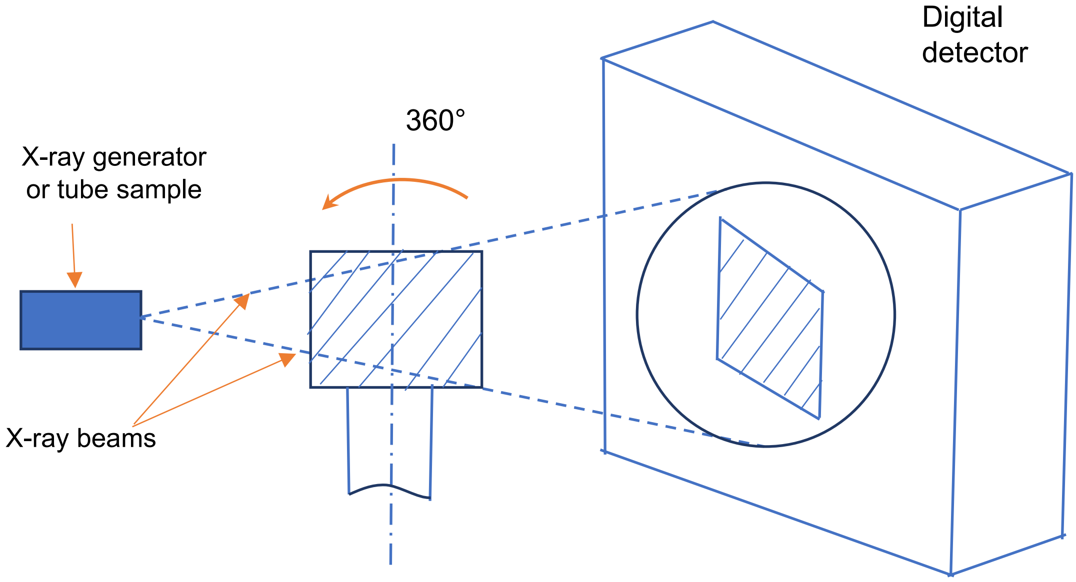

Figure 2.8: Schematic representation of the X-ray-micro computed tomography

Thus, an object to be tested is placed between the X-ray tube and X-ray detector and is usually rotated at 180° or 360° on a platform. The axis of rotation is perpendicular to the direction of the X-ray beam. The geometrically conical emitted X-ray beams from the X-ray tube to the digital X-ray detector pass through and around the tested specimen, with many 2D images captured and recorded at a high resolution. According to Du Plessis et al. (2017), the captured images are then used to mathematically generate a volumetric dataset where each dimensional pixel, aka volumetric pixel (voxel), represents the X-ray density at that location in the object. The authors further mention that before the reconstruction of 2D images, the images can be processed to assess internal manufacturing flaws, porosity and cracks through digital radiography (DR).

This technique has evolved from being laboratory to industrial-based, and as a result, it is now used for several applications such as geosciences (Cnudde & Boone, 2013), food sciences (Schoeman et al., 2016), material sciences (Salvo et al., n.d.) and biological sciences (Du Plessis et al., 2017) just to mention a few. However, despite using micro-CT in these applications, its full potential and capabilities are still being explored.

In general, the quality of images is influenced by several factors, including voltage and current used, reconstruction techniques, scan process and set-up, sample size and mounting stability, and material densities. Image contrast is due to differences in X-ray absorption and is caused by density and compositional variation in the sample (Schoeman et al., 2016).

In summary of the reviewed techniques, it is clear from the construction of the sandwich structures that some of the techniques are unable to characterise the damages fully. According to the characterisation done by Duchene et al. (2018), Shearography and Infrared Thermography cannot detect matrix cracks and fibre breakages in composite structures. Ultrasonic techniques with high-frequency probes show some promise in identifying matrix cracks, yet fibre breakages remain elusive. X-ray μ-CT is the only technique that has the potential to fully characterise the damages induced on the sandwich composite structures, although it depends on the composition of the face sheet and core materials.

2.2.7 Classical sandwich theory for homogenous and isotropic face-sheet and core: static analysis

The dimensions of the typical sandwich composite structure are shown in Figure 2.9.

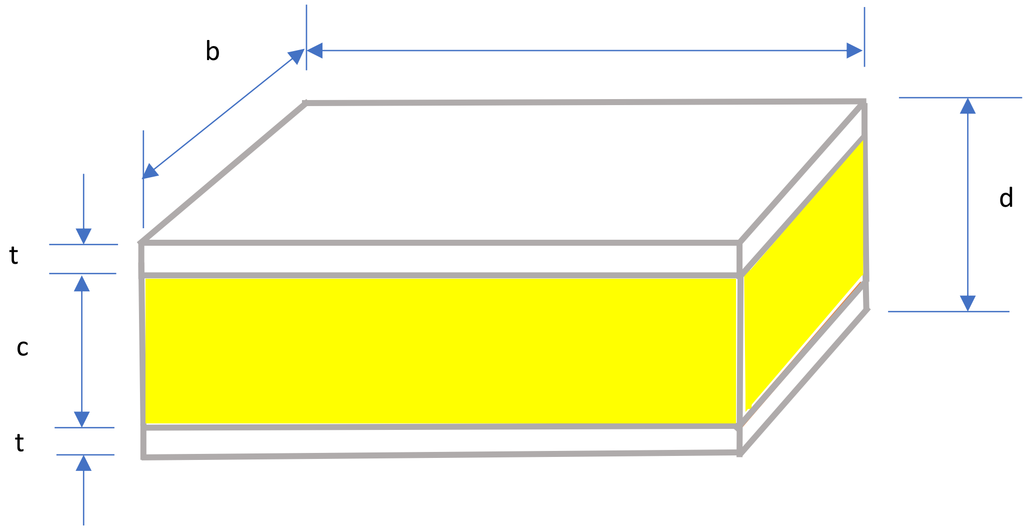

Figure 2.9: Schematic of a typical sandwich composite structure

The sandwich structure's nature requires that the beam stiffness computation include both the core and the face sheets. Thus, the equivalent stiffness, also known as flexural rigidity (the product of the material's Young's modulus and the moment of inertia, *EI*), is used in the analysis.

From the above schematic of a typical sandwich composite structure, $d = c + 2t$, where d is the total depth of the structure, t is the thickness of the face sheets. Furthermore, l and b represent the length and width of the structure, respectively.

The analysis of the deformation of the sandwich structure depends on boundary conditions. To this end, the following are the assumptions are made in the analysis:

- Both the core and face sheets are regarded as homogenous and isotropic
- The Young's modulus of the core, E_c, is much less than the Young's modulus of the face sheet,E_f.
- The core thickness, c is much greater than the thickness of the face sheet, t
- The loading of the composite structure occurs at room temperature.
- The deformation of the sandwich structure depends on the boundary conditions.

It should be noted that the deformation to be considered involves both bending and shear. Thus, the total deformation, $\delta_{\max\,(total)} = \delta_b + \delta_s$ of the composite structure where δ_b and δ_s refer to the bending and shear deformation, respectively. This will correctly predict the load-deflection behaviour of the composite structure. The types of loading induced in the composite sandwich structure is depicted in Figure 2.10.

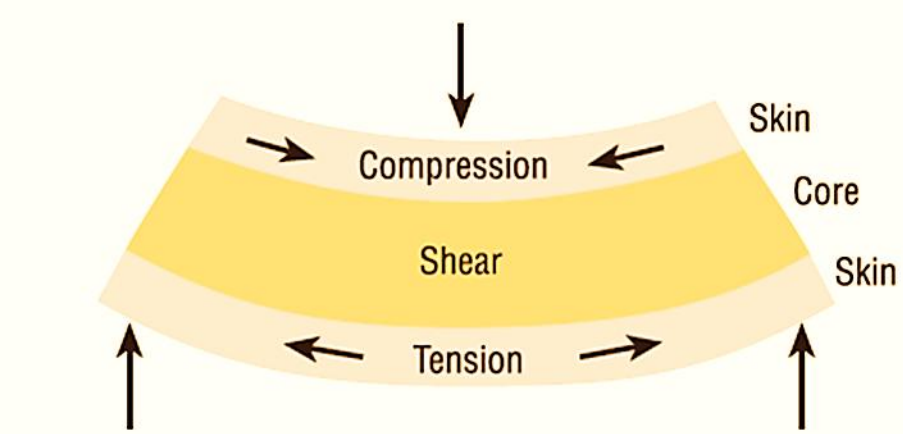

Figure 2.10: Loading scenario for sandwich panel

2.2.7.1 Description of sandwich constituents

Face sheets:

The face sheets are designed to resist global bending moments and to provide high in-plane longitudinal stiffness. This is in addition to providing impact resistance of the sandwich structure.

Core:

- Should be made up of low-density material.
- Have high stiffness in the transverse direction (perpendicular to the face sheets)
- High shear strength
- High shear modulus
- It can either have an isotropic or anisotropic behaviour.

NB. The length-to-thickness ratio should be less than 20 to account for shear deformation accurately. In this study, the length-to-thickness ratio is 16.

The beam bending stiffness, also known as flexural rigidity, EI, is the product of Young's modulus, E and the second moment of inertia, I. For the symmetrical cross-section of a sandwich beam under study, the equivalent bending stiffness that takes into account the core and face sheet materials will be considered. Thus,

$$(EI)_{eq.} = E_c I_c + 2E_f I_f \tag{2.2}$$

Where E_c and E_f are Young's Moduli of Elasticity of the core and the face sheet, respectively. On the other I_c and I_f represent the second moment of inertia of the core and the face sheet sequentially.

Since the centroids of the face sheets do not coincide with the centroidal axis of the composite structure, the parallel axis theorem is used to compute the moments of inertia of the face sheets, as illustrated below.

$$(EI)_{eq.} = \frac{E_c bc^3}{12} + \left(\frac{E_f bt^3}{12} \times 2\right) + E_f bt \left(\frac{c+t}{2}\right)^2 \times 2 \tag{2.3}$$

The above equation reduces to:

$$\left(EI\right)_{eq.} = \frac{E_c bc^3}{12} + \frac{E_f bt^3}{6} + \frac{E_f bt}{2}(c+t)^2 \tag{2.4}$$

From the above and assuming that $E_f \gg E_c$ and $c \gg t$, the equation yields:

$$\left(EI\right)_{eq.} \approx \frac{E_f btc^2}{2} \tag{2.5}$$

2.2.7.2 Incorporation of shear deformation in the analysis

Shear stress, τ induced in the core of the sandwich structure, is the product of modulus of rigidity, G and the shear strain, γ

Thus, $\tau = G\gamma$ hence $\frac{F}{A} \propto G\frac{d_s}{l}$

$d_s = \frac{FL}{k_2(AG)_{eq.}}$ Where k_2 is the coefficient of proportionality.

$$(AG)_{eq.} = \frac{b(c+t)^2}{c} G_c \tag{2.6}$$

$$(AG)_{eq.} \approx b_c G_c \tag{2.7}$$

$$\delta_{\max\,(total)} = \delta_b + \delta_s$$

The total and maximum deformation depends on the boundary conditions for the above-mentioned cases and accounts for both bending and shear stiffness as derived.

Case 1: (a)The uniformly distributed loading with a simply supported beam.

$$\delta_{\max\,(total)} = \frac{5WL^4}{384k_1(EI)_{eq.}} + \frac{WL}{k_2(AG)_{eq.}} \tag{2.8}$$

$$\delta_{\max\,(total)} = \frac{5WL^4}{192k_1E_fbtc^2} + \frac{WL}{k_2bcG_c} \tag{2.9}$$

(b) Simply supported beam with a concentrated load on the mid-span

$$\delta_{\max\,(total)} = \frac{WL^3}{48k_1(EI)_{eq.}} + \frac{WL}{k_2(AG)_{eq.}} \tag{2.10}$$

$$\delta_{\max\,(total)} = \frac{WL^3}{48k_1E_fbtc^2} + \frac{WL}{k_2bcG_c} \tag{2.11}$$

Case 2: (a) The uniformly distributed loading with built-in beam

$$\delta_{\max\,(total)} = \frac{WL^4}{384k_1(EI)_{eq.}} + \frac{WL}{k_2(AG)_{eq.}} \tag{2.12}$$

$$\delta_{\max\,(total)} = \frac{WL^4}{192k_1E_fbtc^2} + \frac{WL}{k_2bcG_c} \tag{2.13}$$

(b) Built-in beam with a concentrated load on the on the mid-span

$$\delta_{\max\,(total)} = \frac{WL^3}{192k_1(EI)_{eq.}} + \frac{WL}{k_2(AG)_{eq.}} \tag{2.14}$$

$$\delta_{\max\,(total)} = \frac{WL^3}{96k_1E_fbtc^2} + \frac{WL}{k_2bcG_c} \tag{2.15}$$

Note: k_1 and k_2 are coefficients of proportionality (correction factors) for bending and shear respectively.

Since the above derivations were based on static analysis, dynamic impact loading analysis is expected to yield larger deflections.

2.2.8 Dynamic impact response of sandwich panel due to low velocity

During impact, the sandwich panel exhibits a dynamic response characterised by local indentation at the impact site, while the entire section undergoes global deformation, as illustrated in Figure 2.11.

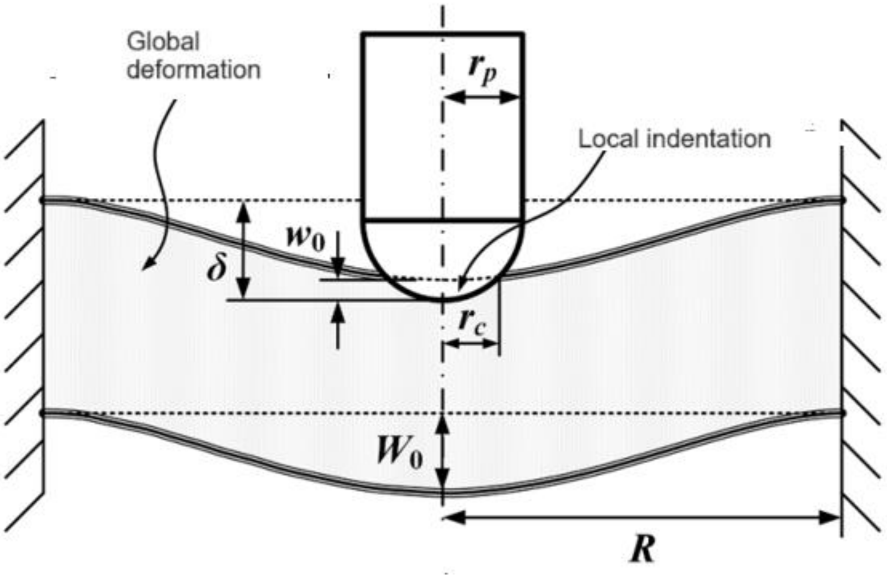

Figure 2.11: Combination of local indentation and global deformation for the foam core sandwich panel under low-velocity impact

Source: Y. Zhu & Sun (2021)

$$\delta = w_0 + W_0 \tag{2.16}$$

Where δ is the displacement of the impactor.

w_0 is the indentation depth.

W_0 is the global deformation.

Based on the above configuration, the impact process can be divided into three phases. Phase 1 involves understanding the failure of the incident (top) face sheet, phase 2 deals with the core crushing and shearing fracture, while phase 3 covers the failure of the back sheet.

According to Chai and Zhu (2011), the deformation of a sandwich panel subjected to impact load can be divided into two parts: indentation and global deflection. The authors further mention that, regarding low velocity impact, the global deflection depends on the boundary conditions and is highly dependent on the impact duration. When the impact duration is long enough, i.e., low velocity impact, the global deflection is in phase with the motion of the impactor and thus dominates the deformation. In the case of a short duration impact, i.e., high velocity impact, the deformation is dominated by indentation.

The purpose of this study is not to delve into the analytical formulations and models since these analyses are limited to the elastic region and fail to cover the full damage evolution cycle. To this end, only numerical results will be compared to the experimental results for validation.

A two-degree-of-freedom spring-mass model system was adopted to model the three phases involved in penetrating the sandwich panel. The spring mass model is based on the assumption of quasi-static that is only valid for a large mass impactor striking a lightweight panel. The law of conservation of energy is applied, which assumes that no energy is lost due to heat, sound, or localised plastic deformations. The kinetic energy of the impactor is absorbed by the elastic strain energy of the face sheets. Figure 2.12 illustrates the schematic of a two-degree-of-freedom spring-mass model system used to simulate low-velocity impact.

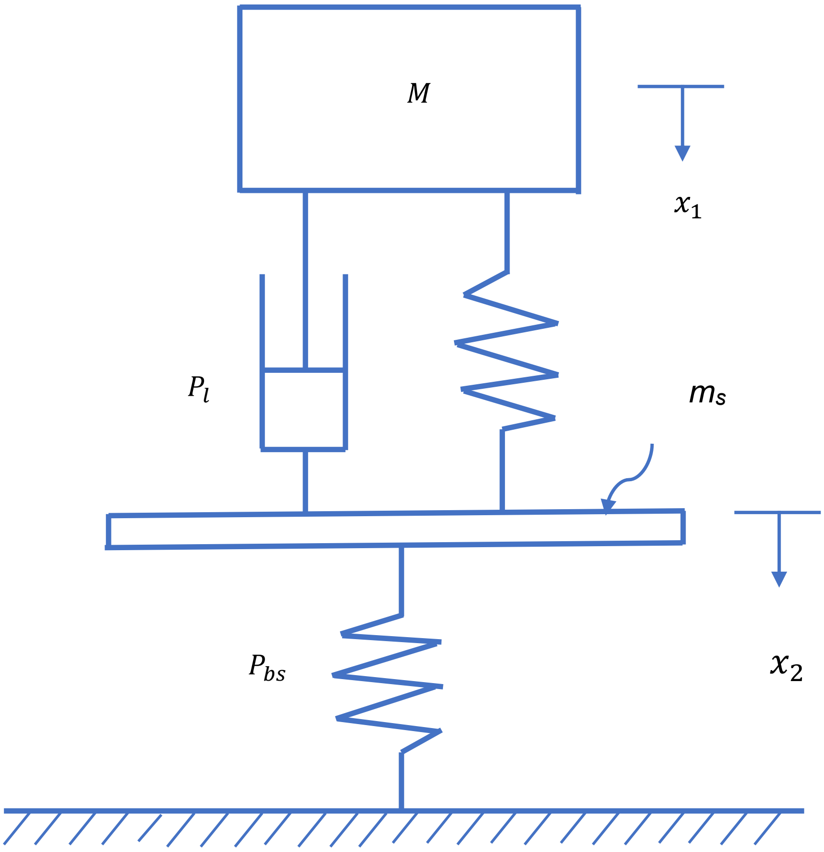

Figure 2.12: Spring mass model for low-velocity impact response of foam core sandwich panel

Where,

M - large mass impactor

m_s - effective mass of the panel

P_l - indentation force

P_{bs} - force due to bending and shear

x_1 – displacement of the large mass.

x_2 – displacement of the sandwich panel

The indentation depth and global deformation can be expressed in terms of respective displacements, i.e.:

$$w_0 = x_1 - x_2 \tag{2.17}$$

$$W_0 = x_2 \tag{2.18}$$

The equations of a two-degrees-of-freedom spring-mass model system are presented below:

$$\begin{cases} M\ddot{x}_1 + P_l = 0 \\ m_s\ddot{x}_2 - P_l + P_{bs} = 0 \end{cases} \tag{2.19}$$

with initial conditions of $x_1(0) = 0$, $\dot{x}_1(0) = V_0$, $x_2(0) = 0$ and $\dot{x}_2(0) = 0$.

The velocity decreases from a release position where the potential energy is converted into kinetic energy. The velocity decreases to zero before a rebound occurs. Some energy is transferred to the impactor, while the specimen absorbs the other during an impact event. The rebound effect can easily be identified on the force displacement curve. It is noteworthy to mention that the initial velocity is greater than the final velocity. The numerical modelling will be conducted in Chapter 5 and validated by experimental data.

The next chapter deals with the manufacturing of the sandwich panels and preparation work for testing and respective experimental procedures.

CHAPTER 3

MANUFACTURING OF SANDWICH PANELS AND EXPERIMENTAL PROCEDURES

3.1 Introduction

This chapter outlines the manufacturing process of the test specimens and the experimental techniques employed. The manufacturing process includes fabric preparation and the curing of composite panels. Following fabrication, specimens were cut to the required testing dimensions using waterjet technology. To assess structural integrity, non-destructive evaluation techniques such as Infrared Thermography and X-ray micro-computed tomography were applied for flaw detection. The experimental procedures for both flexural testing and Drop Weight Impact Testing (DWIT) are described in detail. Additionally, the resulting damage states of the tested specimens are presented. The chapter also explains the experimental protocols used for damage detection. A detailed analysis and discussion of the test results are provided in the subsequent chapter.

3.2 Manufacturing Process

In this study, the sandwich specimens were made from carbon and glass fibre face sheets pre-impregnated (prepregs) resin systems. “Prepreg” is a contracted and common term for a reinforcing fabric that has been pre-impregnated with a resin system. The sandwich core was made from a cross-linked, close-cell polyvinyl chloride (PVC) foam that resists water, gas, and oil.

Since prepregs have resin and hardener, epoxy resin is avoided from hardening by storing it in freezers. Carbon prepregs used in this work were stored at -18°C, while glass fibre prepregs were stored at room temperature. The carbon fibre prepregs were kept at ambient temperature for 24 hours before they were worked on or cut so that they could reach thermal equilibrium. The prepregs were chosen because of the advantages they offer, such as ease of use, low void content, control of laminate thickness and fibre volume fraction, high specific modulus, and strength, to mention but a few.

The prepregs were processed using the autoclave forming method. This method allows the prepregs or laid-up composite panel to be subjected to hydrostatic pressure and vacuum in an autoclave during the curing process. Temperature requirements depend on the part being cured. Temperature profiles of heating, dwell and cooling gradients usually form part of the curing cycle to initially allow the resin to reflow and eventually cure.

3.3 Materials' Specifications

The following are the specifications of the materials used:

Carbon fibre prepregs – T300/C520-14 3K 2 x 2 Twill carbon weave epoxy resin impregnated, fabric thickness of 0.25 mm, areal weight of 202.5g/m^2, resin content 41% and volatile content of 92%. K means that there are 1000 filaments; thus, 3K means that there are 3000 carbon rovings in the weave epoxy.

Glass fibre prepregs – E-Glass, ply thickness 0.25 mm and areal weight of 200 g/m^2.

Polyvinyl chloride (PVC) foam core is cross-linked and closed-cell with a thickness of 9 mm. More specifications are given in Table 3.1.

Table 3.1: PVC foam core properties

Variant	Nominal Density (kg/m^3). (1)	Density Range (kg/m^3). (1)	Compressive Strength (MPa) (2)	Compressive Modulus (MPa) (2)	Shear Strength (MPa). (3)	Shear Modulus (MPa). (3)	Tensile Strength (MPa. (4)	Tensile Modulus (MPa). (4)
M080	80	72 - 92	1.6 (1.42)	97 (76)	1.2 (1.07)	30 (26)	2.74 (2.28)	146 (94)

Note: All the values in brackets are minimum values

3.4 Preparation and Fabrication

After all the materials and tools were gathered, the prepregs were cut according to the required specifications, i.e., the required panel dimensions are 950 x 1000 mm. The stacking sequence for both panels was 0/90, +45/-45, core, -45/+45, and 90/0. This makes the sandwich structure symmetric and balanced. Both carbon and glass fibre panels were fabricated the same way. Figures 3.1 and 3.2 show the laying up of prepregs and vacuum bagging before curing, respectively.

Figure 3.1: Hand lay-up of prepregs

Figure 3.2: Vacuuming process before placing in the autoclave

3.4.1 Curing Process

The curing process was characterised mainly by three stages: ramp up, dwell and ramp down, as shown in Figure 3.3 As the vacuum bagged part shown in Figure 3.2 was placed in the autoclave, the following stages ensued:

Ramp-up stage – the temperature was increased to 120°C for 1 hour while the pressure was maintained at 1 bar. The heat introduced into the system allowed the resin to reflow, and the vacuum bagging system removed the gases produced during this reaction.

The dwell–isothermal process leads to cross-linking of components, resulting in strong and durable molecular bonds. This process took place for 1.5 hours.

Ramp down – the cooling effect was experienced as the temperature gradually decreased for half an hour. This gradual cooling allows minimum thermal residual stresses to be locked inside the composite panel and prevents microcracking.

Compared with the typical curing cycle curve for carbon/epoxy composites, the curve represented in Figure 3.3 has one dwell, and the temperature was not raised above 120°C, which is sometimes the case for the second dwell.

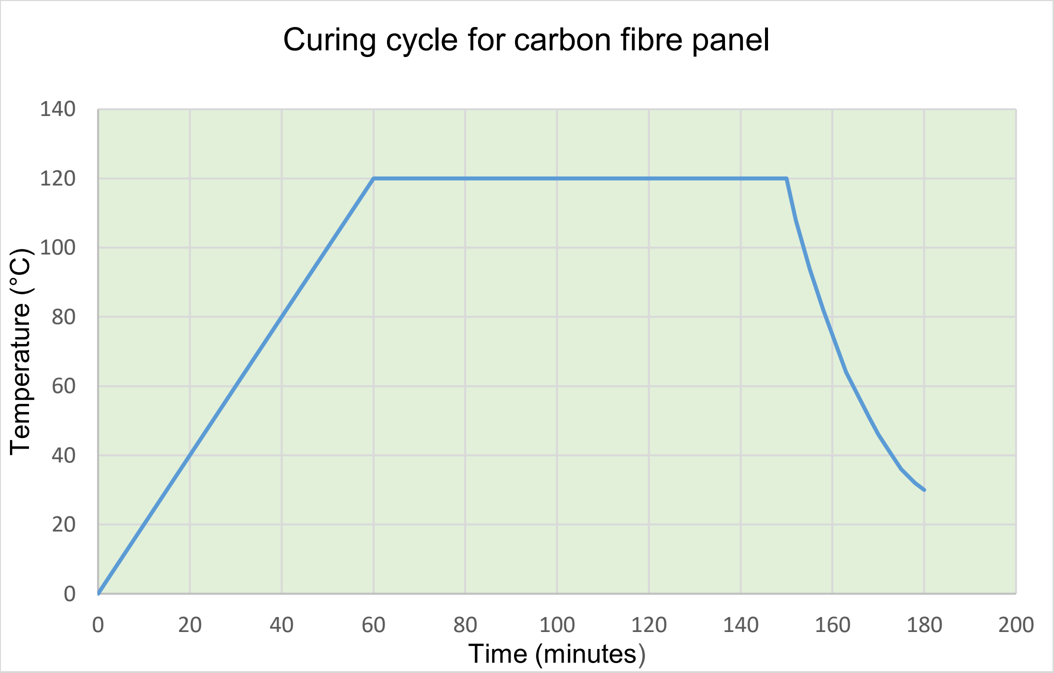

Figure 3.3: Curing cycle for carbon fibre panel

After curing, the panels were debagged, demoulded, and left for 48 hours before being worked or cut. Figures 3.4 and 3.5 show the top views or surface finishes of carbon and glass fibre, respectively.

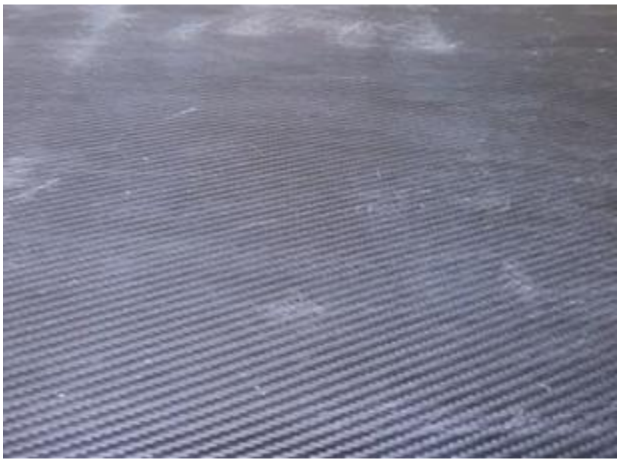

Figure 3.4: Carbon fibre panel top side

Figure 3.5: Glass fibre panel top side

3.4.2 Cutting of specimens

The specimens were cut to the required sizes as per the specific testing standards using a water jet cutting machine to avoid the chances of inducing stresses. Each was weighed to determine its mass before the specimens were inspected for defects. All the specimens recorded a mass of 32 grams for CFRP, as shown in Figure 3.6.

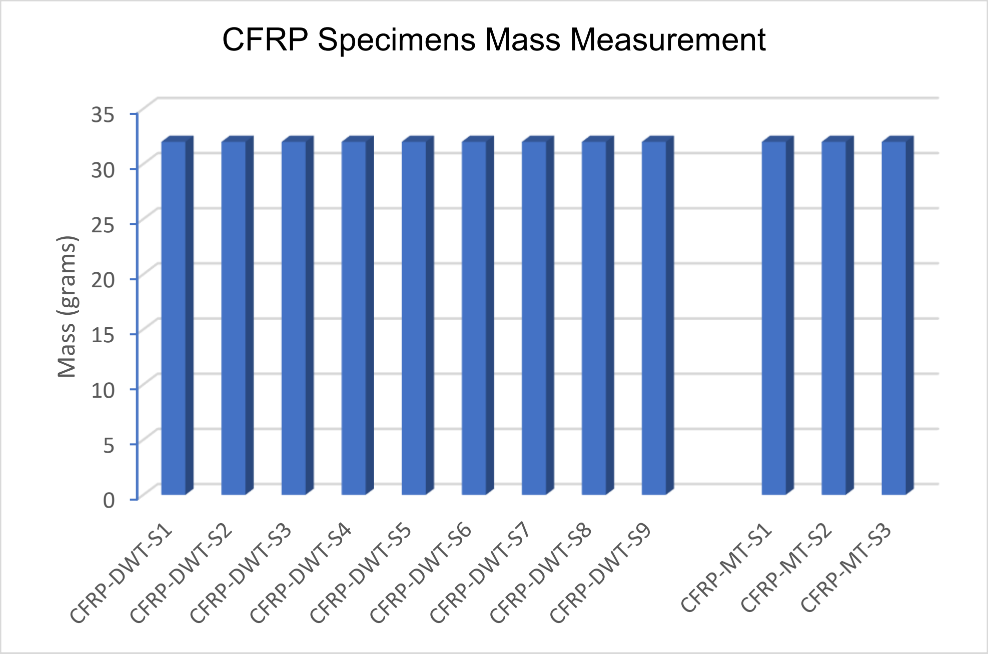

Figure 3.6: Mass Measurement of Drop Weight Testing specimens for CFRP

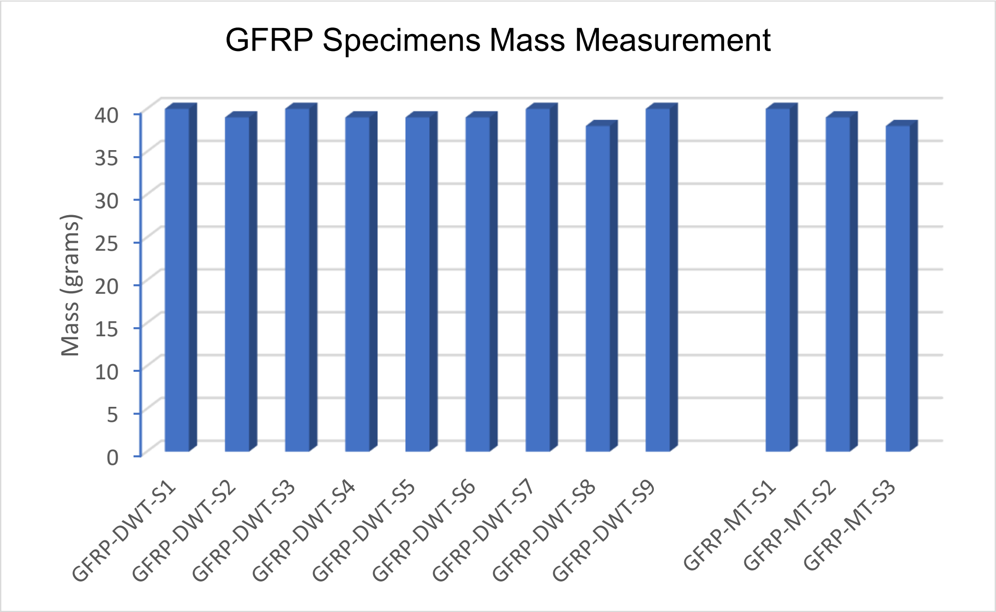

Figure 3.7: Mass Measurement of Drop Weight Testing specimens for GFRP

As observed in Figure 3.7, the masses of the specimens range from 38 grams to 40 grams. The average for the weighed specimens is 39.25 grams. This is in sharp contrast to the CFRP specimens, which recorded similar mass values. It can be predicted that the GFRP specimens will likely exhibit more defects than CFRP specimens. The defects are mainly due to the spread of epoxy during the curing process. The GFRP specimens will likely experience less damage than the CFRP type because they are less brittle.

3.5 Computation of Densities for Specimens

Based on the measured masses, the following are the computed densities:

$$For\ CFRP: \rho = \frac{m}{v} = \frac{32 \times 10^{-3}}{0.150 \times 0.100 \times 0.009} = 237.04\ kg/m^3$$

$$For\ GFRP: \rho = \frac{m}{v} = \frac{39.25 \times 10^{-3}}{0.150 \times 0.100 \times 0.009} = 290.74\ kg/m^3$$

Compared with the weighed flexure specimens, the density of CFRP remained constant, as expected. The same could not be said of GFRP as the two specimens recorded fewer values compared to drop weight impact testing weighed specimens. This dropped the average density value. However, the same average density value of 290.74 kg/ m^3 will be used for calculations.

3.6 Flexural Tests (Three-Point Bending Tests)

As part of characterising the specimens, the quasi-static three-point bending tests were conducted on a Zwick-Roell testing machine to:

(a) determine the maximum compressive strength of the specimens.
(b) determine the flexure modulii of the specimens.
(c) observe the failure modes of the specimens.
(d) provide the basis for analysis of the impact-damaged specimens.

The specimen sizes for both CFRP and GFRP specimens were cut by waterjet technology to 150 mm length, 50 mm width and thickness of 9 mm. Five specimens were chosen for each type. The specifications of the indenter were 10 mm in diameter and 60 mm long.

3.6.1 Experimental testing procedure for flexural tests

After fitting the indenter and accurately positioning the supports, each specimen was placed on supports, ensuring that an equal amount of overhang was left at both ends. Although the testing standard adopted was akin to testing steels, an equivalent standard (D7274/D7264M-15) for composites, with a span-to-thickness ratio of 13:1, was employed compared to a 16:1 acceptable ratio. The similar standard ASTM C393/C393M can be employed since it can measure core shear strength and flexural stiffness under bending loads. The other specific testing requirements, such as the radius of the indenter of 5 mm and feed rate of 1 mm/min, were maintained. The inputs for the testing wizard were a preload force of 25 N, a width of 50 mm and measured thickness for each specimen since there was a slight deviation. An option to stop the testing process could either be invoked by putting a force or deflection limit. Notably, the preload force was determined by testing the first specimen without this setting and then observed when the initial proportionality of force and defection occurred. The test was ready to commence once the force was set to zero. This testing procedure was adopted for all the tested specimens. Figure 3.8 shows the experimental setup of the three-point bending test while figures 3.9 and 3.10 illustrate the tested specimens.

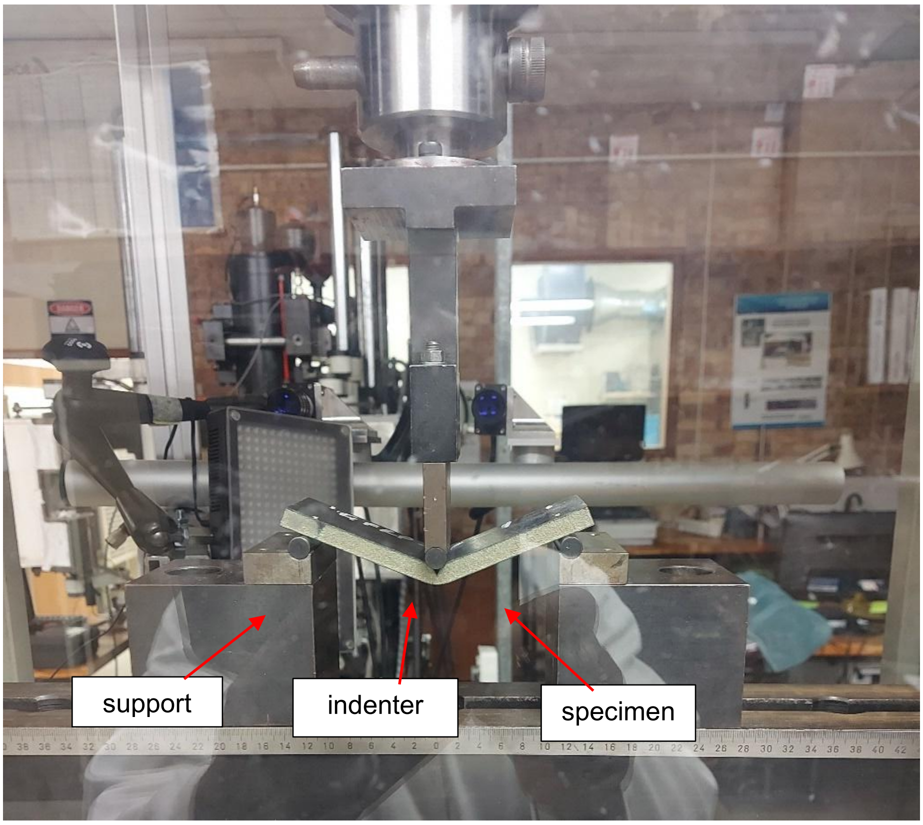

Figure 3.8: Three-point bending test experimental setup

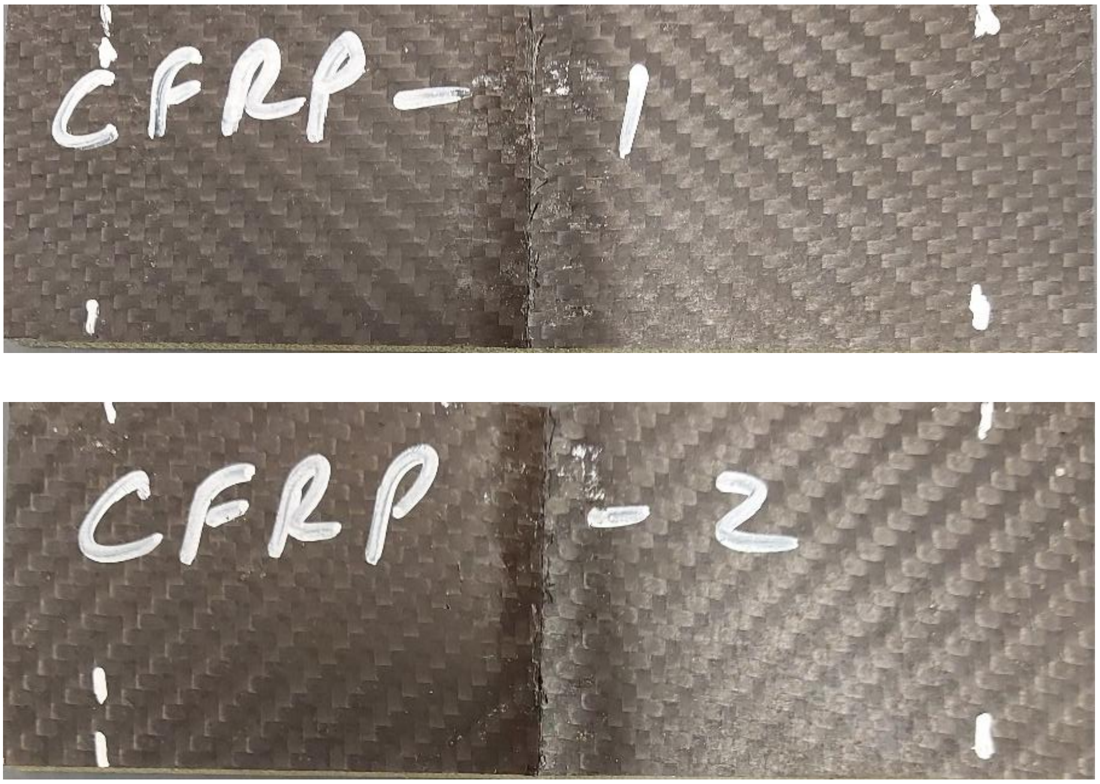

Figure 3.9: Flexure Tested CFRP Specimens

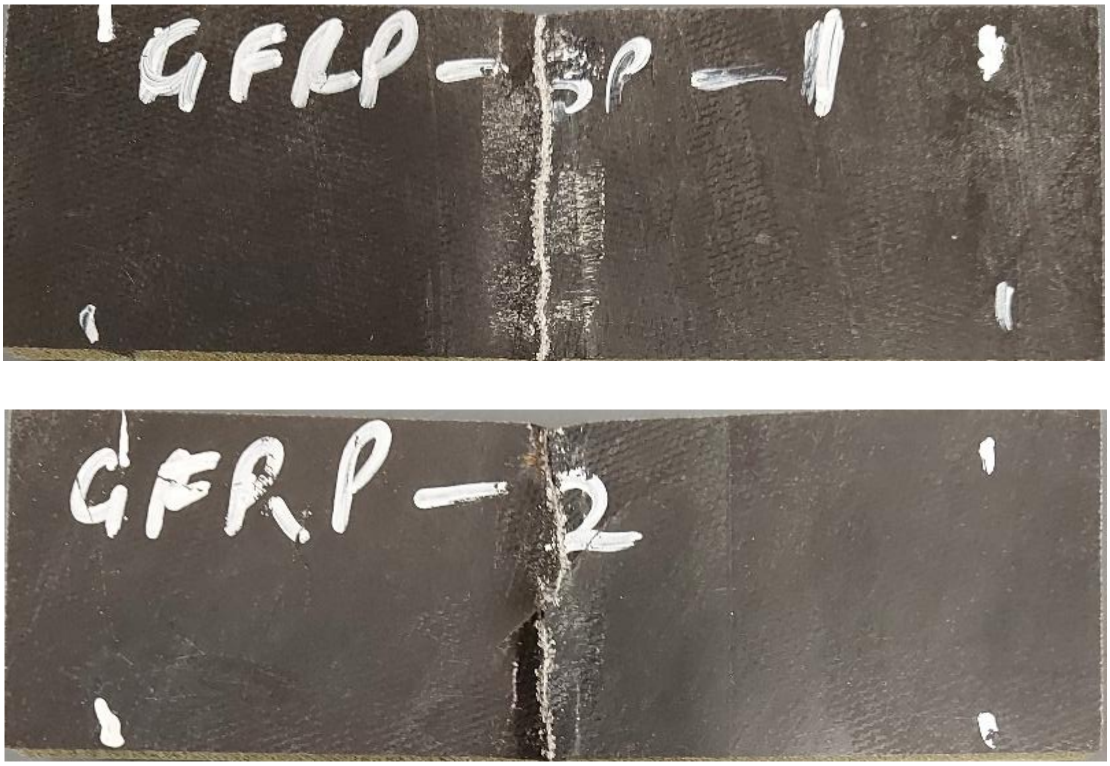

Figure 3.10: Flexure Tested GFRP Specimens

The following general comments can made about the tested specimens:

GFRP specimens appear to have been more physically damaged at the indentation zone compared to CFRP specimens. The quasi-static indentation failure can only be discussed after analysing the results. The results of this testing will be presented and analysed in the next chapter.

3.7 Drop Weight Impact Testing (DWIT)

Although the main testing focus was to induce barely visible impact damage (BVID) due to low-velocity impacts, it was also important to observe the damage mechanisms across the thickness of the specimens. A known mass was released from a predetermined height on the specimen. The instrumented tester is fitted with proximity sensors to determine the extreme positions of the top and bottom platforms. In addition, the piezoelectric accelerometer or transducer is mounted on the bottom platform on which the impactor is attached. Before the impactor is released, the height is captured by the data acquisition system, including the force and impact deflection as soon as the impactor lands on the specimen. The free fall velocity is also measured, and the total impact energy can be determined. With the help of data acquisition software, the plots for force, energy or displacement versus time can be made. The data obtained from this testing will be further processed using NDT methods.

3.7.1 Experimental set-up and procedure for DWIT

Figure 3.11 shows the clamping fixture used to secure the specimen during the impact event, in accordance with the ASTM D7136/D7136M-15 standard.

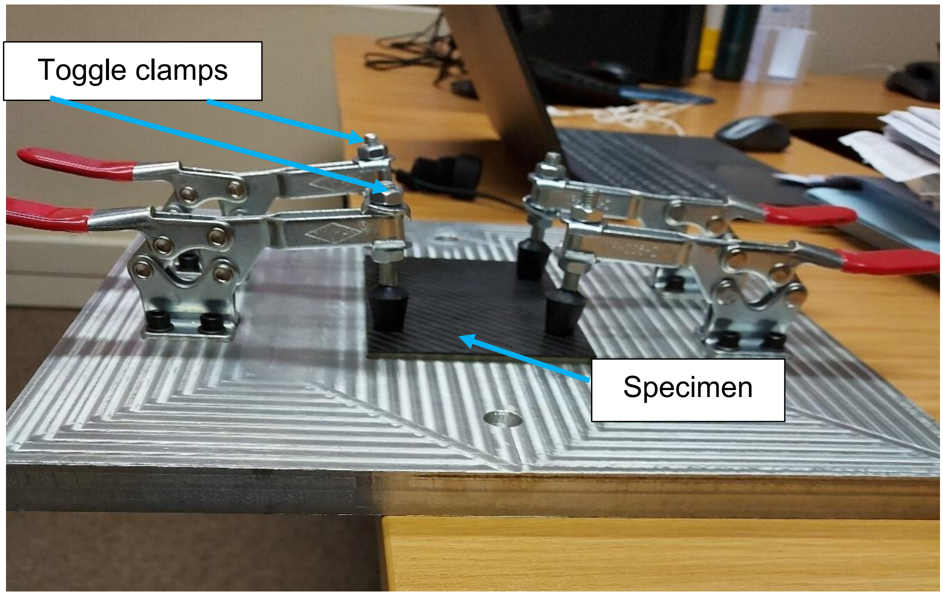

Figure 3.11: Clamping fixture with specimen in place

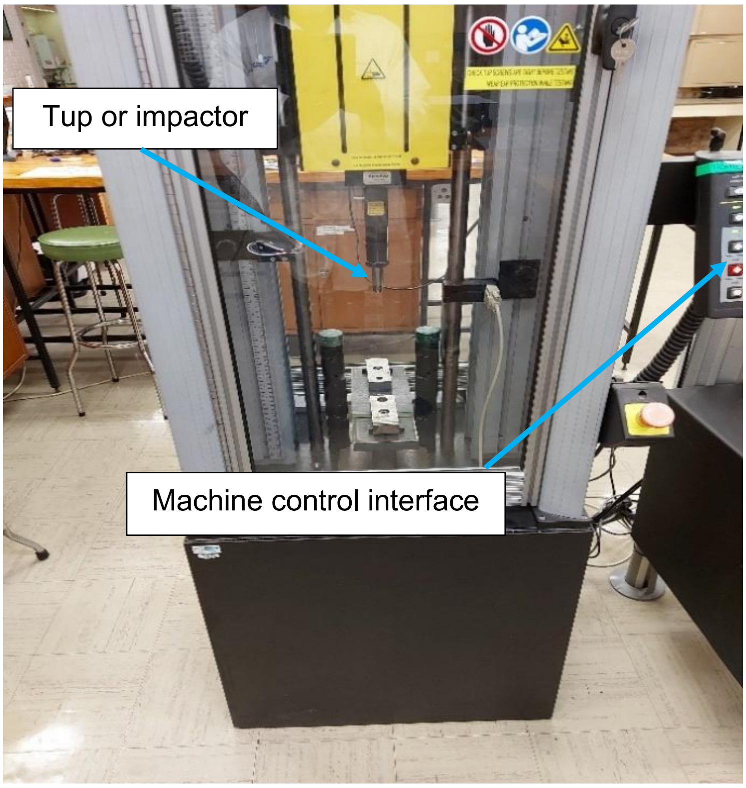

Figure 3.12: Drop Weight Impact Testing Machine Setup

The impactor of the hemispherical shape used had a mass of 125.83 g and a diameter of 12.5 mm. No weights were added. The weights considered during testing were only for the dynatup, impact holder and impactor, with a total weight 5.61 kg. To determine the suitable initial height to use, a randomly chosen height of 135 cm was set and the extent of damage exerted on the CFRP specimen was observed. It was observed that the impactor completely perforated the CFRP specimen. An initial height of 120 cm was, therefore, considered suitable. For comparison purposes, each specimen type was set at the same height. Thus, the first specimens were set at an initial height of 120 cm. The specimen heights were varied between 120 cm and 2 cm so that the full spectrum damage could be observed. At the end of each test, the final velocity was recorded. The experimental setup is shown in Figure 3.12. The respective tested specimens are shown in Figures 3.13 and 3.14.

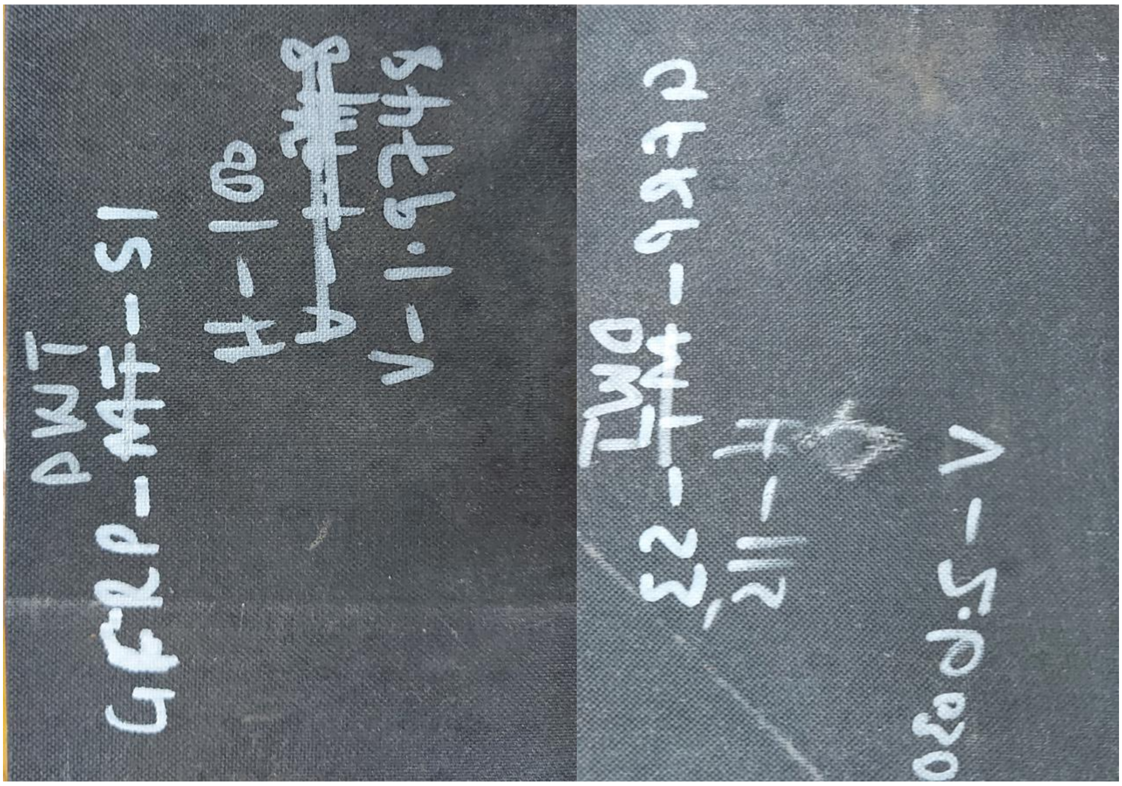

Figure 3.13: Some impacted GFRP specimens

Figure 3.14: Some impacted CFRP specimens

It was visually observed that the CFRP-type specimens were damaged more than the GFRP type for the same set drop height. The tested specimens will be analysed to determine the extent of the damage using X-ray micro-computed tomography.

3.8 Experimental Procedures for NDT Approaches in Assessing Damage.

As previously discussed, Infrared Thermography is based on the principle that subsurface anomalies in a material result in localised differences in surface temperature caused by different rates of heat transfer at the defect zone. Thus, if a defect is present in the specimen, it interrupts the flow of heat from the lamp, causing a variation in the temperature distribution at the object's surface. The technique was used mainly for the detection of manufacturing defects. Figure 3.15 shows the schematic setup.

3.8.1 Infrared thermography

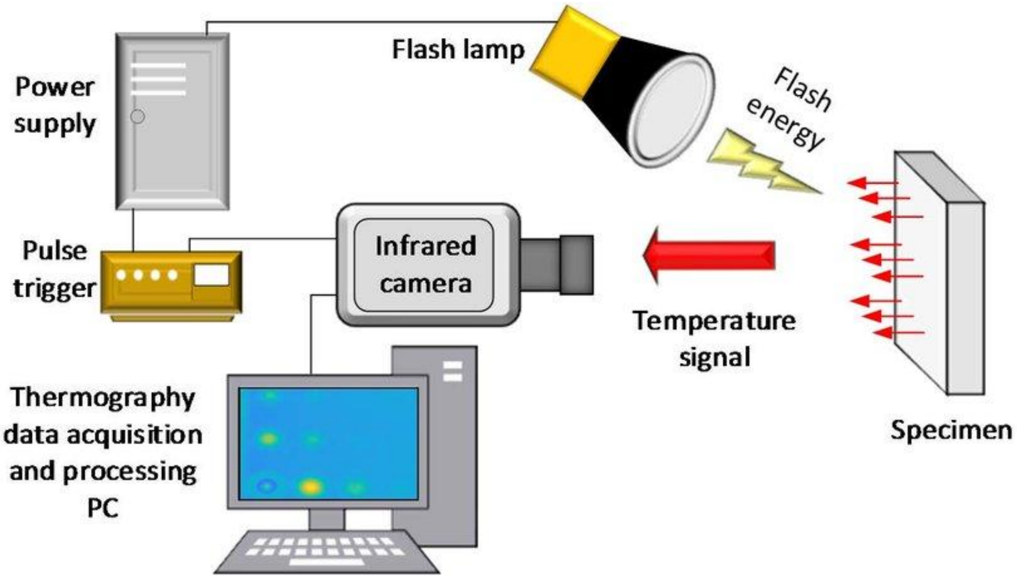

Figure 3.15: Schematic Setup for Infrared Thermography

3.8.2 X-ray micro-computed tomography (micro-CT)

It is a non-destructive imaging technology that uses X-rays to create 3D images of materials or objects under review. This study uses this technique to characterise and analyse the damage morphologies of the impacted CFRP and GFRP specimens.

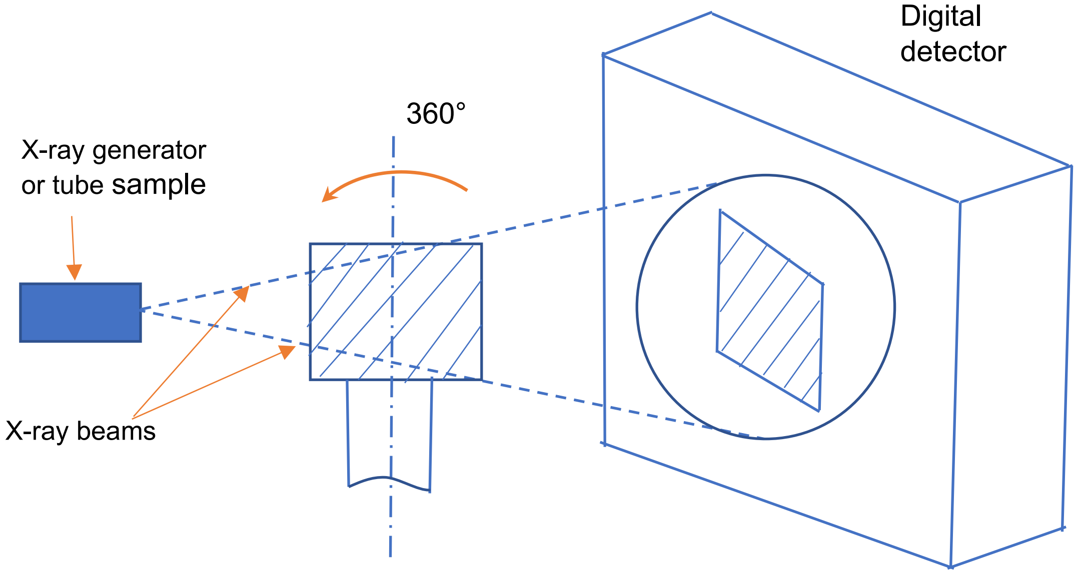

Figure 3.16: Schematic representation of the X-ray-micro computed tomography experimental setup

An object to be tested was placed between the X-ray tube and detector and rotated on a platform at 360°. The axis of rotation is perpendicular to the direction of the X-ray beam as shown in Figure 3.16. The geometrically conical emitted X-ray beams from the X-ray tube to the digital X-ray detector pass through and around the tested specimen. Many 2D images are captured and recorded at a high resolution. The captured images are then used to mathematically generate a volumetric dataset where each dimensional pixel, aka volumetric pixel (voxel), represents the X-ray density at that location in the object. The 2D images can also be processed to assess internal manufacturing flaws, porosity, and cracks through digital radiography (DR) (Du Plessis et al., 2017).

3.8.2.1 Experimental procedure for x-ray micro-computed tomography

Each specimen was put in a low-density container so that its image would not interfere with that of the tested specimen. Because the sizes of the tested specimens were too long in relation to the detection spectrum, about 75% of either side of the specimen length from the centre was covered for inspection. The scanning time lasted for about two hours. The raw data was viewed in a 3D graphic viewer called myVGL 3.5. When the scanning process was completed, the recorded raw data was ready for further processing using Volumetric Graphics VGStudio Max software. Thus, the general steps are sample preparation and mounting, scanner setup and parameter selection, scanning procedure, image reconstruction and image visualisation. The results of such analyses are discussed in Chapter 4.

This chapter has provided detailed descriptions of the manufacturing processes of the specimens, experimental procedures, and samples of the tested specimens. The detailed analyses of the tests conducted are covered in the next chapter. This next chapter also contains the results of the virgin specimens that were inspected for manufacturing defects using infrared thermography.

CHAPTER 4

EXPERIMENTAL ANALYSIS OF FLEXURAL AND IMPACT BEHAVIOUR, AND DAMAGE ASSESSMENT IN SANDWICH STRUCTURES

4.1 Introduction

As outlined in the previous chapter, this section provides a detailed analysis and discussion of the flexural and drop weight impact test results. Flexural testing enabled the determination of flexural strength and bending stiffness for each specimen type. Drop Weight Impact Testing facilitated the generation of force–time and impact energy–time plots, which were critical in identifying damage thresholds and characterising the impact response of the specimens. By correlating impact energies with the observed damage morphologies, valuable insights into the damage resistance and tolerance of the specimens were obtained.

Initial flaw detection in virgin specimens was conducted using Infrared Thermography, although its limitations in fully characterising manufacturing defects were acknowledged. In contrast, X-ray micro-computed tomography was employed for post-impact damage assessment, allowing for the identification of failure mechanisms within both the laminate skins and the foam core. These experimental findings form the basis for validating the numerical modelling results presented in the subsequent chapter.

4.2 Thermographic Inspection

Three specimens each for carbon fibre-reinforced plastic (CFRP) and glass fibre-reinforced plastic (GFRP) skins, respectively, were used. One of the specimen types was spray painted with black high-heat rust oleum capable of resisting temperatures up to 1200°C. The other specimens were not sprayed for purposes of comparison with the sprayed ones.

Each specimen was subjected to heat supplied via two 230 V lamps charged at 120 V. The surface of the specimens at room temperature of 26°C was increased to 60°C with the camera set to take pictures at 30-second intervals. The heat source was switched off upon the specimens’ surface temperature reaching 60°C, and pictures were taken during the cooling cycle until the temperatures of the surfaces reached around 30°C.

The following Figures 4.1 and 4.2 illustrate the observations made during the inspection of the specimens.

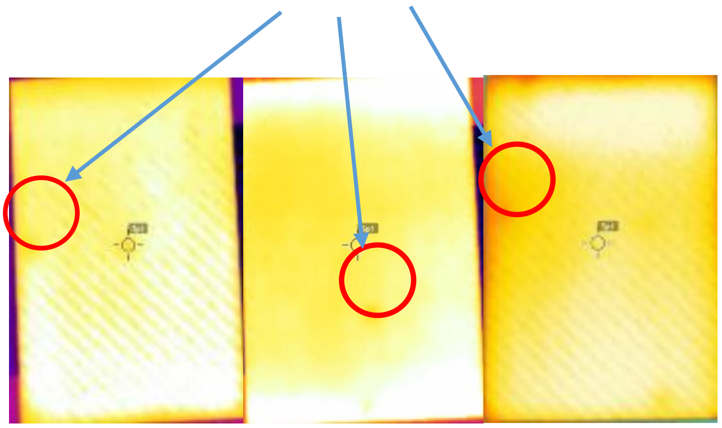

Specimen 1 Specimen 2 Specimen 3

Figure 4.1: Thermographic Images of CFRP specimens

Defects were identified during the heating cycle for all the specimens. The defects observed are some small holes drilled in the foam so that the pre-impregnated resin system could provide a firm bond with the foam during curing. The second specimen that was spray painted was more clearly visible compared to the other two. This was attributed to the quality of the surface finish provided by spray painting.

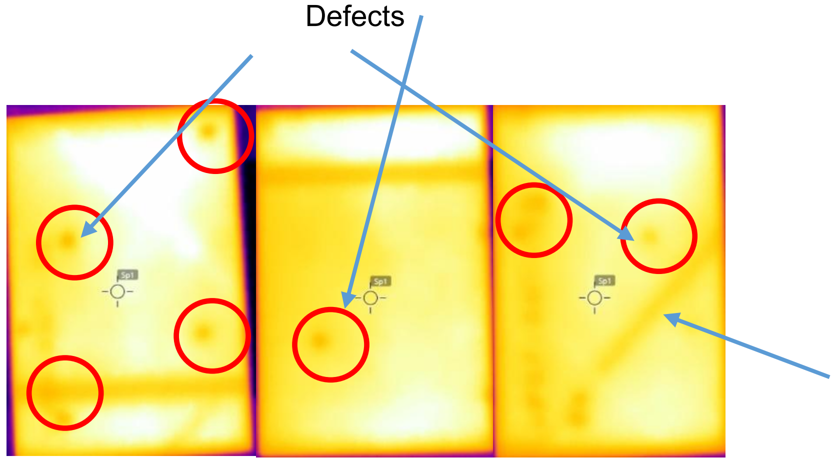

Specimen 1 Specimen 2 Specimen 3

Figure 4.2: Thermographic Images of GFRP Specimens

The defects on GFRP specimens are also clearly visible on all the specimens, as indicated in Figure 4.2, with no notable difference detected on the second spray-painted specimen because the quality of the surface finish changed slightly. The noticeable horizontal and diagonal lines are caused by the unevenly distributed resin system in the foam core. As for the CFRP specimens, visible images that could be attributed to 'defect' were observed during the heating cycle.

It was also observed that the emissivities for the specimens' surfaces for both CFRP and GFRP sandwich composites were the same at 0.95, while their respective reflection temperatures were also the same at 20°C.

Since the manufacturing process was done as a panel, the qualitative assessment of the specimens was regarded as good. The existence of man-made defects in the foam core was not expected to affect the impact tests conducted since bending deformation is handled by the skins while the foam deals with shear deformation.

The man-made manufacturing defects in the foam core were better characterised by the X-ray micro-computed tomography technique, as shown in Figure 4.3. The characterisation is enhanced because all views can be analysed simultaneously to gather critical information.

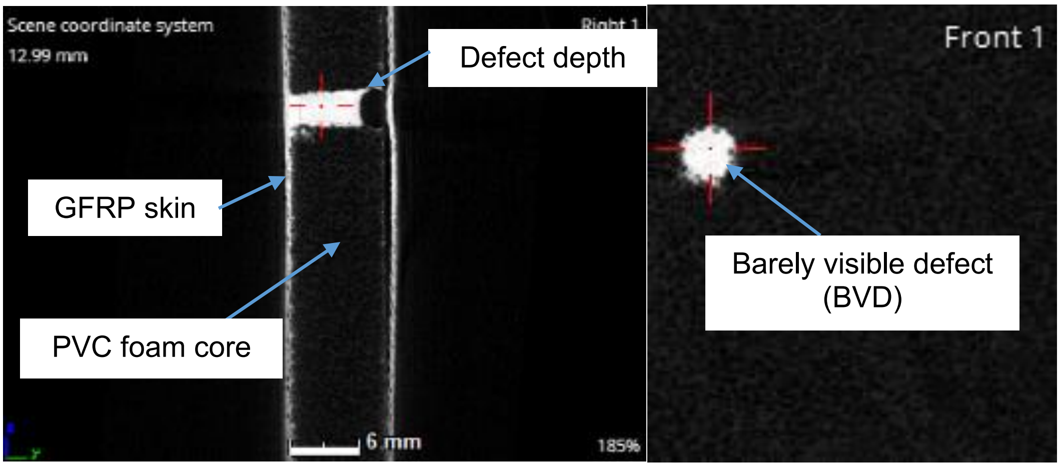

Figure 4.3: GFRP specimen with a barely visible man-made manufacturing defect

4.3 Flexural Tests

The quasi-static three-point bending tests were conducted on five specimens for each panel type.

The force-deflection curves, illustrated in Figure 4.4 for the CFRP specimens, show linear proportionality at approximately 1.5 mm. This deflection is considered as the maximum in-plane deflection. The respective force under which this maximum in-plane deflection occurs is estimated to be 400 N.

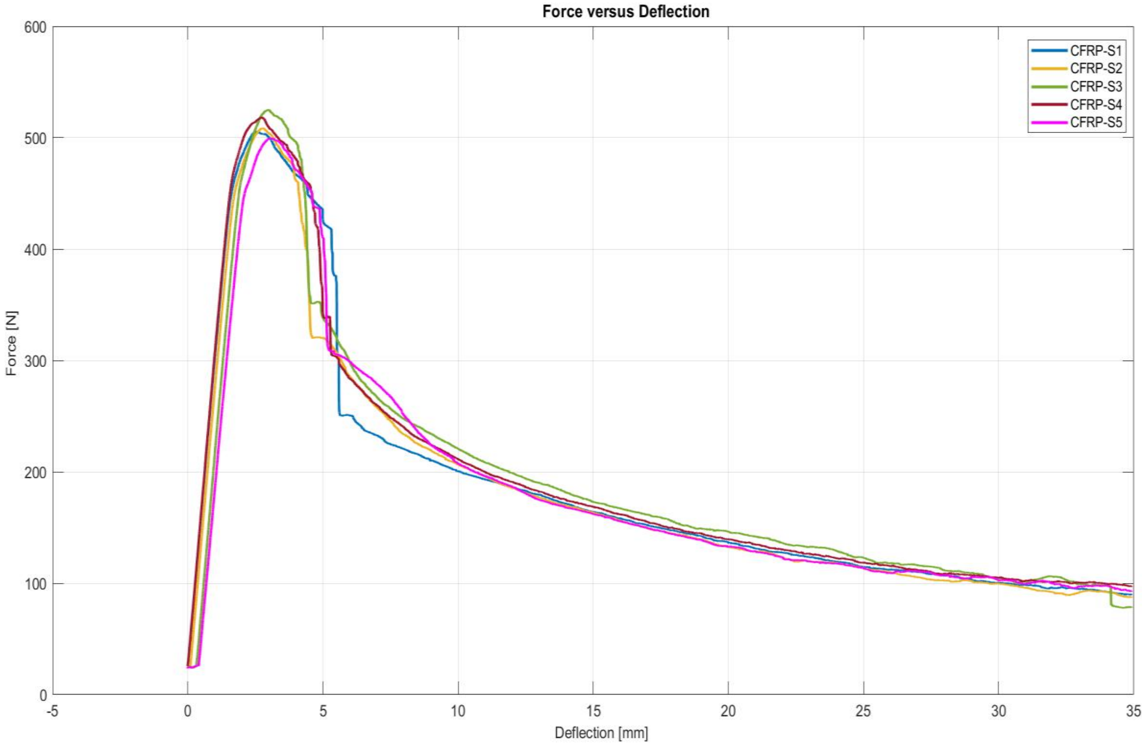

Figure 4.4: Force-deflection curves for CFRP specimens

The second stage shows the yielding process, which took place rapidly, approximately 1 mm after the linear behaviour and reached a peak load estimated at 520 N. This stage exhibits a non-linear increase of the force and deflection up to the peak loads before a slight decrease and then a sudden drop. This action can be attributed to the drop in stiffness due to debonding or delamination. The last stage was characterised by a gradual decrease in force as the deflection increased. This behaviour can be ascribed to the foam compression failure.

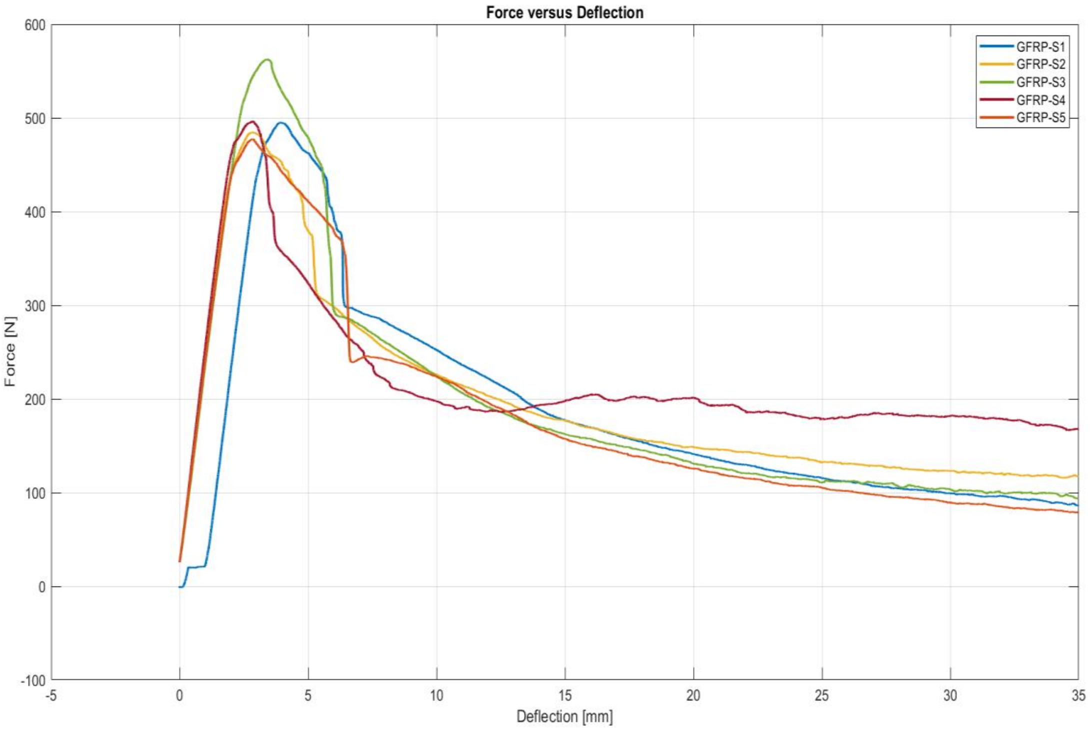

Figure 4.5: Force-deflection curves for GFRP specimens

The GFRP specimens exhibited the same trend, as shown in Figure 4.5, albeit with an outlier mainly observed in the last stage. This was potentially due to slippage during testing that resulted in unsymmetrical bending.

To better understand the correlation of data in this last stage and perhaps predict the dynamic impact response of the panels, a plot specifically for this data range was plotted for each specimen type. The CFRP and GFRP plots are shown in Figures 4.6 and 4.7, respectively.

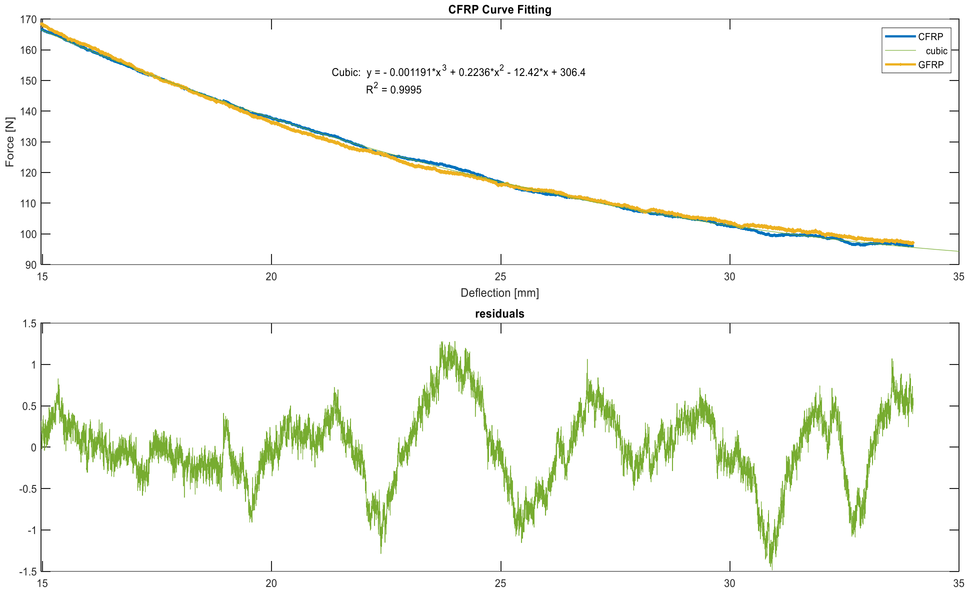

Figure 4.6: Force-deflection CFRP curve fitting

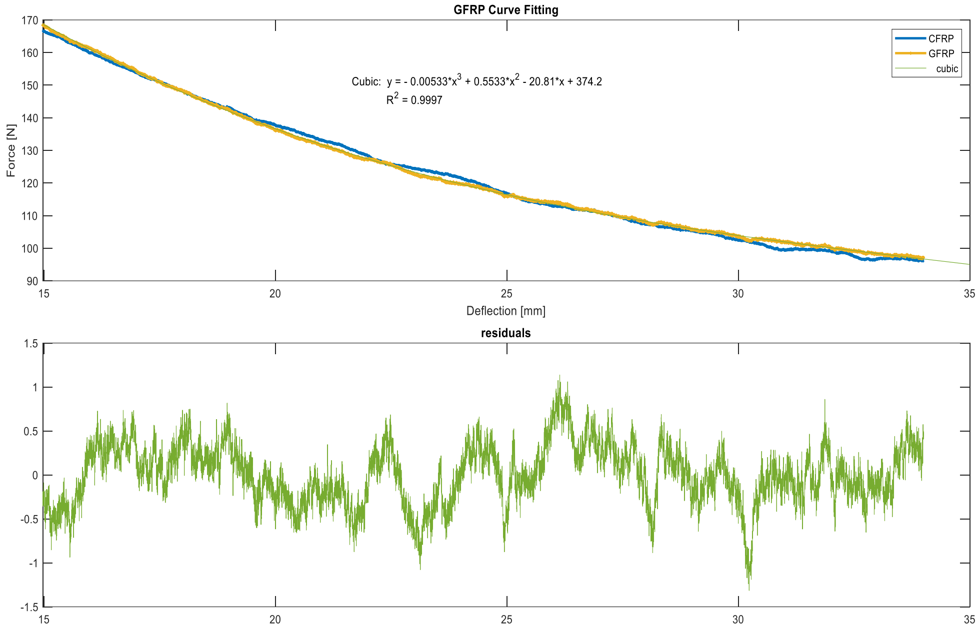

Figure 4.7: Force-deflection GFRP curve fitting

The residual plots show acceptable deviations of data points from the datum or zero line. The fluctuating patterns are magnified as the least squared (R^2) values are both around 0.9. This data can be useful in predicting and optimising the panels to carry in-service loads without experiencing complete failure.

4.3.1 Test summary results

The maximum values of flexural strength of the specimens are presented in Table 4.1.

Table 4.1: Flexural strength for tested specimens

	CFRP Max. Stress	**GFRP** Max. Stress
S1	22.47	22.01
S2	23.66	21.54
S3	23.35	26.15
S4	23.05	22.08
S5	23.23	21.22

Note: *All stress values are in MPa*

4.3.2 Computation of statistical properties of data

For CFRP Specimens

$$\bar{x} = \frac{\sum_{i=1}^{n} x_i}{n} = 23.15$$

Thus, the mean value for the stress value is 23.15 MPa

$$s = \sqrt{\frac{\sum_{i=1}^{n}(x_i - \bar{x})^2}{n-1}} = 0.44127089$$

$$Variance = s^2 = 0.1947270676$$

$$Coefficient\ of\ Variation, CV = 100 \times \frac{s}{\bar{x}} = 1.91\%$$

For GFRP Specimens

$$\bar{x} = \frac{\sum_{i=1}^{n} x_i}{n} = 22.60$$

Thus, the mean value for the stress value is 22.60 MPa

$$s = \sqrt{\frac{\sum_{i=1}^{n}(x_i - \bar{x})^2}{n-1}} = 2.0155024$$

$$Variance = s^2 = 4.06225$$

$$Coefficient\ of\ Variation, CV = 100 \times \frac{s}{\bar{x}} = 8.92\%$$

The above-calculated information is summarised in Table 4.2.

Table 4.2: Flexural stresses statistical data

	CFRP	**GFRP**
Mean value	23.15 MPa	22.60 MPa
Std deviation	0.4413	2.0155
Variance	0.1947	4.0623
Coeff. of variation	1.91%	8.92%

The standard deviation is higher for the GFRP specimens mainly because specimen 3 recorded a maximum value of 26.15 MPa from a minimum value of 22.01 MPa. This was not consistent with the other specimens.

4.3.3 Comparison of experimental and calculated values for flexural strength

The comparison is based on the mean experimental values computed at peak loads. Using the formula for calculating flexural strength,

$$\sigma_f = \frac{3FL}{2bh^2} \ldots\ldots\ldots\ldots\ldots\ldots\ldots\ldots\ldots\ldots\ldots\ldots\ldots. (4.1)$$

Where σ_f is the flexural strength (MPa), *F* is the load (N), *L* is the support span (m), *b* is the width (m), and *h* is the sample thickness in the direction of impact force (m).

In this study, the following parameters were used:

F, (peak loads – 509 N for CFRP and 491 N for GFRP)

L, (support span) – 0.120 m

b, (width) – 0.05 m

h, (thickness) – 0.009 m

The computed flexural strength values for the CFRP and GFRP specimen types are 22.62 MPa and 21.82 MPa, respectively. These values give percentage errors of 2.29% for CFRP and 3.45% for GFRP specimen types.

4.3.4 Determination of transverse or flexural moduli of elasticity

The sandwich specimens are considered as anisotropic materials. The Euler-Bernoulli beam model was applied for the loading configuration and dimensions considered. As such the presence of shear stress will be ignored for purposes of calculations.

The following equation was used to compute flexural moduli for the specimen types:

$$E_f = \frac{L^3}{4bh^3}\left(\frac{\Delta F}{\Delta s}\right) \ldots\ldots\ldots\ldots\ldots\ldots\ldots\ldots\ldots\ldots\ldots\ldots (4.2)$$

ΔF is the difference in forces in the elastic region, and *Δs* is the difference in flexural deflection evaluated at corresponding points.

The computed flexural moduli values of the CFRP and GFRP specimen types are 3.16 GPa and 2.96 GPa, respectively.

The respective maximum compressive strength for the specimens can be computed by dividing the peak load and the corresponding cross-sectional area for each averaged specimen value. The calculated values are 1.13 MPa for CFRP and 1.09 MPa for GFRP specimen types.

4.3.5 Computation of equivalent bending stiffness

Since the flexural moduli of elasticity for face sheets was determined, the equivalent flexural rigidity for each specimen type was calculated. The previously derived equation 2.5 for sandwich structure is used, and in this case, the shear effect during bending is neglected in the analysis.

$$\left(EI\right)_{eq.} \approx \frac{E_f btc^2}{2} \ldots\ldots\ldots\ldots\ldots\ldots\ldots\ldots\ldots\ldots\ldots\ldots\ldots\ldots\ldots\ldots\ldots\ldots\ldots\ldots\ldots\ldots\ldots\ldots\ldots (2.5)$$

Thus, for CFRP the $\left(EI\right)_{eq.} = \frac{3.19\times10^{9}\times0.05\times0.88\times10^{-3}\times\left(7.24\times10^{-3}\right)^{2}}{2} = 3.67587\ Nm^{2}$

and for GFRP the $\left(EI\right)_{eq.} = \frac{2.96\times10^{9}\times0.05\times0.88\times10^{-3}\times\left(7.24\times10^{-3}\right)^{2}}{2} = 3.4134\ Nm^{2}$

The significance of the bending stiffness is crucial in ensuring the structural integrity and stability of beams when subjected to external loads. The bending stiffness affects the structure's load-bearing capacity, with higher stiffness allowing the structure to support greater loads without excessive deformation. Engineers use the bending stiffness to optimise designs, ensuring that the structures can handle expected loads effectively while minimising material usage and cost.

4.4 Drop Weight Impact Testing Results

Before the actual testing, it was important to determine the drop heights that could inflict minimum damage to the specimens. Notably, the total impacting mass could not be adjusted further since it was the minimum, hence the focus on drop heights. Being aware of the challenges associated with achieving the main objectives of testing inter-alia, the limitation of 300 mm minimum drop height as per ASTM D7136/7136M-15 standard, it was important to carry out the velocity test first to deal with potentially unreliable velocity readings at minimal drop heights.

4.4.1 Velocity test

The test was accomplished by recording the velocities at different heights, which were considered as high enough to cause no velocity errors. The test was done with no specimen clamped on the fixture. Figure 4.8 shows the relationship between velocity and drop height for the test conducted.

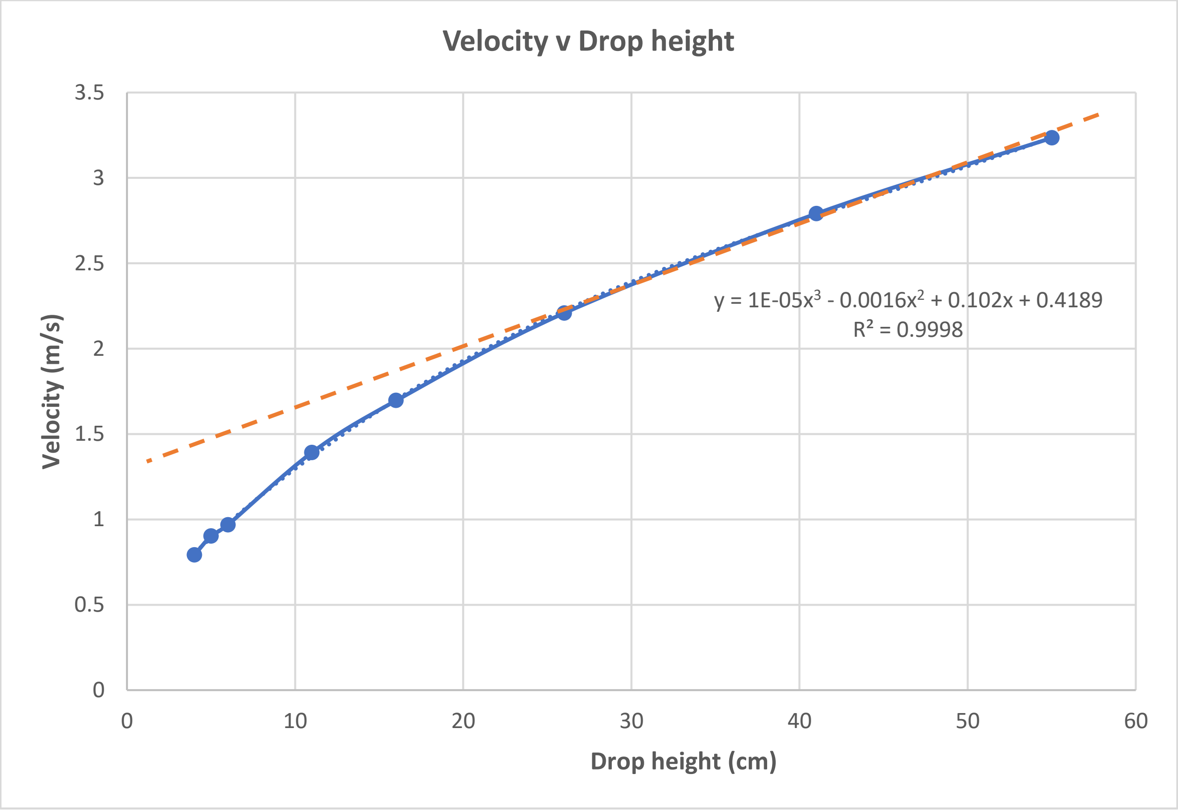

Figure 4.8: Correction of velocity readings at lower drop heights

The plot shows that: $y = 1E - 05x^3 - 0{,}0016x^2 + 0{,}102x + 0{,}4189$ with R squared equals to 0,9998. This equation was used to correct the recorded velocities at lower drop heights. The curve seems to corroborate the fact that the minimum drop height of 300 mm is required to carry out the tests as per ASTM D7136 standard since the curve becomes near linear from 300 mm upwards when velocity varies with drop height. It was necessary to carry out this correction because high values of drop heights resulted in high impact energies, thereby inflicting excessive damage to the specimens, which, in this instance, was undesirable. It is evident from the graph that errors increase with a decrease in drop height. Table 4:3 below provides the corrected velocities values for respective drop heights.

Table 4.3: Correction of velocity at predetermined drop heights

Drop Height (cm)	**Corrected Velocity (m/s)**
3.2	1.0772
3	1.0500
2.5	0.9811
2	0.9100

The next section deals with specimens that experienced low-velocity minimum damage. Some specimens experienced barely visible impact damage (BVID). The hemispherical impactor of 12.5 mm diameter and total drop weight of 5.61 kg were used to inflict damage on the specimens. The drop heights were selected to inflict minimum or barely visible impact damage on the specimens. Figures 4.12 and 4.13 depict dented and BVID-inflicted specimens. The statuses of the impacted specimens subjected to different impact energies are explained in Table 4.4.

Table 4.4: Impact energies and statuses of impacted specimens

Drop height (m)	**Impact Velocity (m/s)**	**Impact Energy (J)**	**Remark on status**
0.02	0.9	2	BVID
0.03	1	3	BVID of delamination
1	2	11	Top face sheet penetrated
1.15	2.6	19	Near full penetration
1.2	2.8	22	Full penetration

The data indicates barely visible impact damages (BVID) occur at velocities below 0.9 m/s.

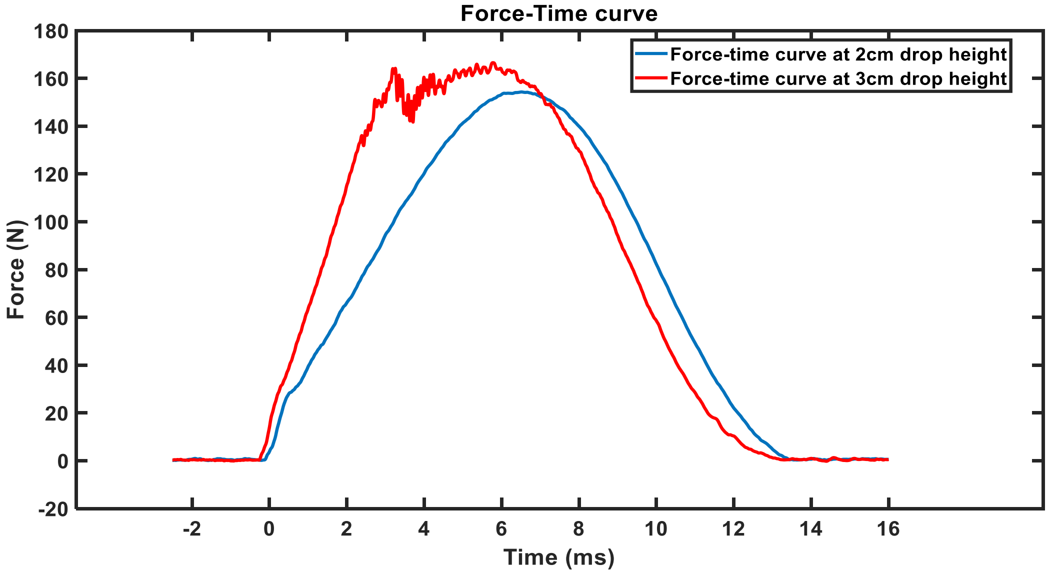

Figure 4.9: Damage initiation at lower drop height

The impact responses were observed on load-time curves. The area under each curve represents the total energy absorbed during the impact event. For all curves, the load increased linearly with the increase in time before the peak load was reached. The time to reach the peak load depended on the impact energy values. Thus, the higher the impact energy, the shorter the time to reach peak value. For barely visible impact damage, two cases exist: (1) the impact energy is completely dissipated throughout the specimen, as reflected on a load-time graph with a smooth curve. It took 6 ms to reach the peak load, (2) a sharp drop in load by 18% as a manifestation of damage initiation and a reduction of stiffness in the structure. In this case, the peak load was reached at only 3 ms. From the sharp bottom end, the load increased non-linearly to below the initial peak load. A smooth curve followed the second peak load to zero load at the end of the impact event, which lasted for 13 ms, as shown in Figure 4.9. The first notable damage mechanism to manifest was delamination (interfacial debonding or debonding of the face sheet and the foam core). However, delamination is preceded by matrix cracking caused by shear and tensile stresses during impact. Consequently, most numerical simulations were conducted on velocities within the BVID range.

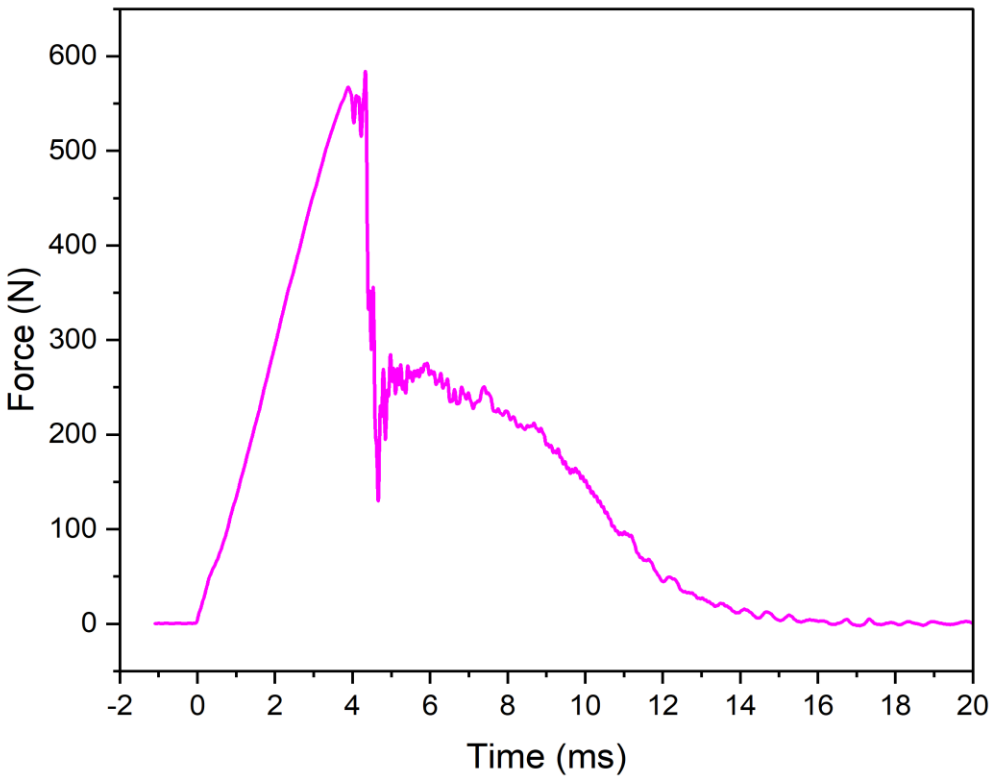

Figure 4.10: Damage evolution with top face sheet penetrated

The reduction in stiffness continued until the top face sheet was completely perforated, with a sharp drop of the load to approximately 75% of the peak load. This drop in load suggests a minimum contact force recorded at the impactor at the time of perforation. When the impactor regained full contact with the foam core, it occurred at a lower load than the peak load before another slight sharp increase. The load gradually decreased from a lower peak load to zero and remained constant, as illustrated in Figure 4.10.

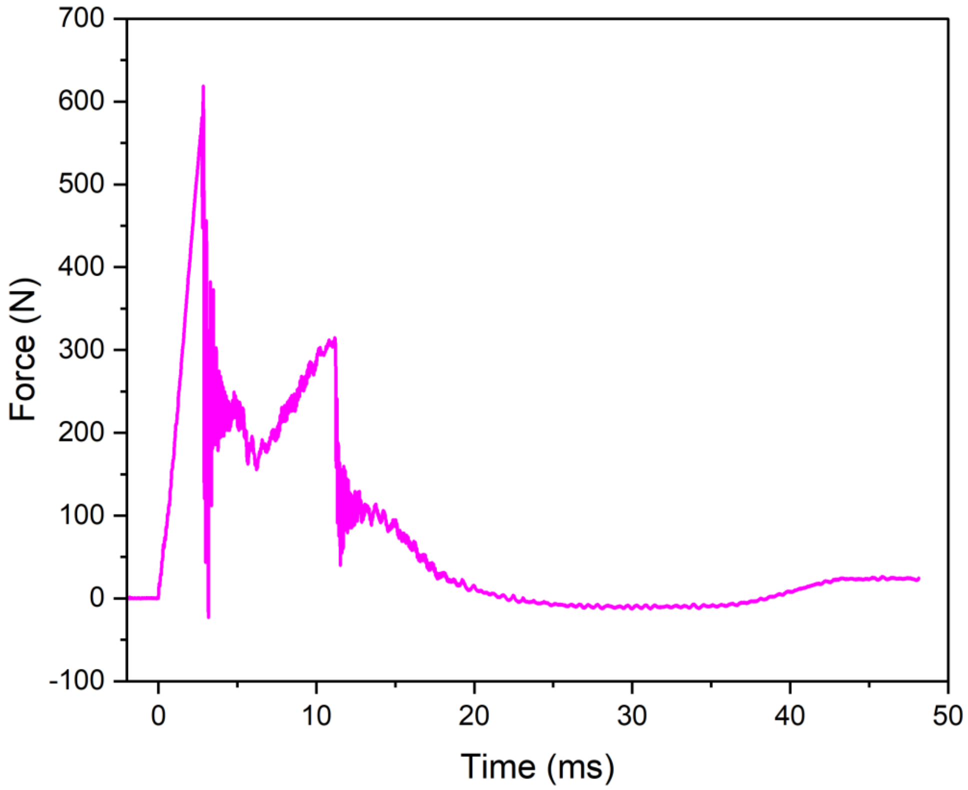

Figure 4.11: Damage evolution for a nearly perforated specimen

In the near-penetrated specimen, the foam core was crushed immediately after the top face sheet was penetrated. This resulted in a decrease in load before the densification of the foam core due to load increase, as shown in Figure 4.11. The second sharp curve shows that the back face sheet was nearly perforated because it did not reach the zero load. At this stage, the perforated foam core remained in contact with the impactor. The load started to decrease gradually from a point above the endpoint to indicate a complete perforation of the foam core. The decrease reached the zero load, remained constant for a while before a gradual increase, and then remained constant again. The gradual increase is perhaps an indication of residual energy before full penetration.

4.4.2 Results of impacted specimens

Visual inspections of the top faces of impacted specimens show the damages inflicted.

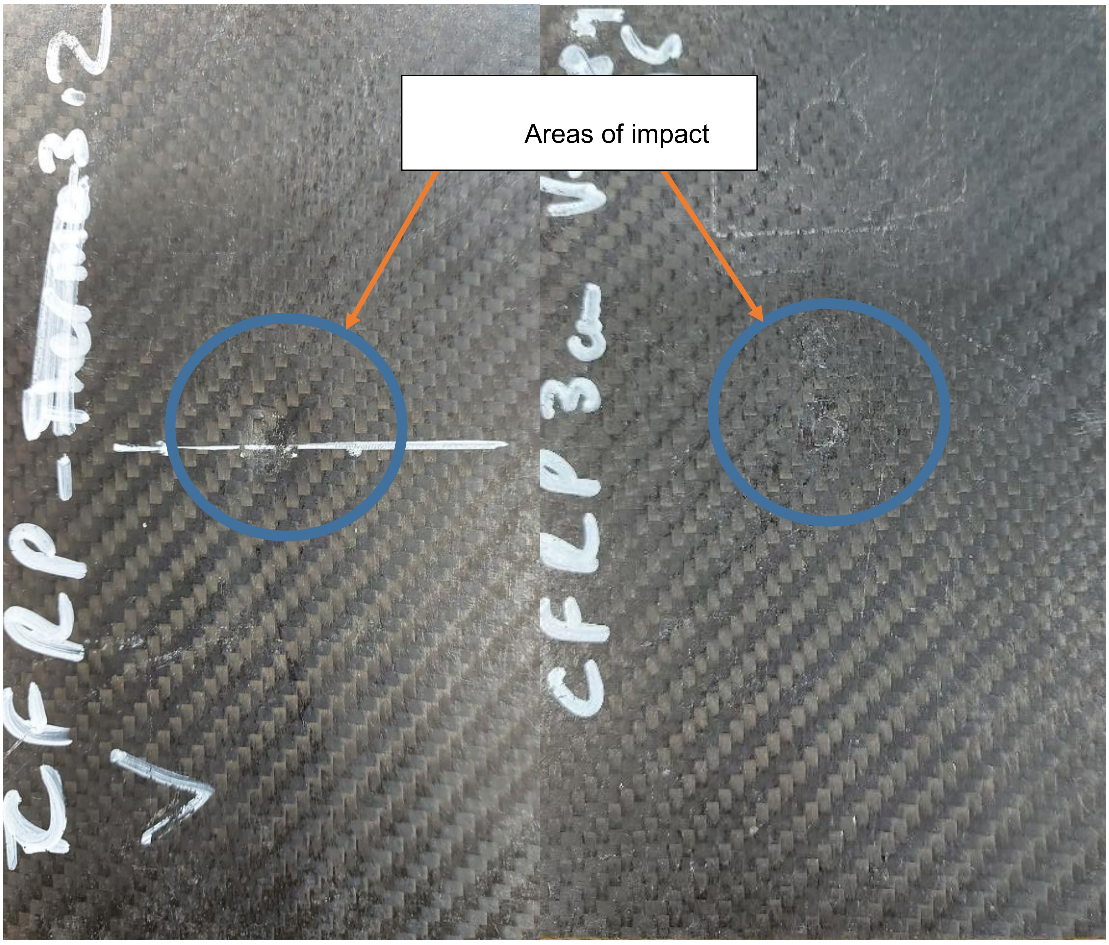

(a) Dented specimen (b) BVID specimen

Figure 4.12: CFRP damage-inflicted specimens

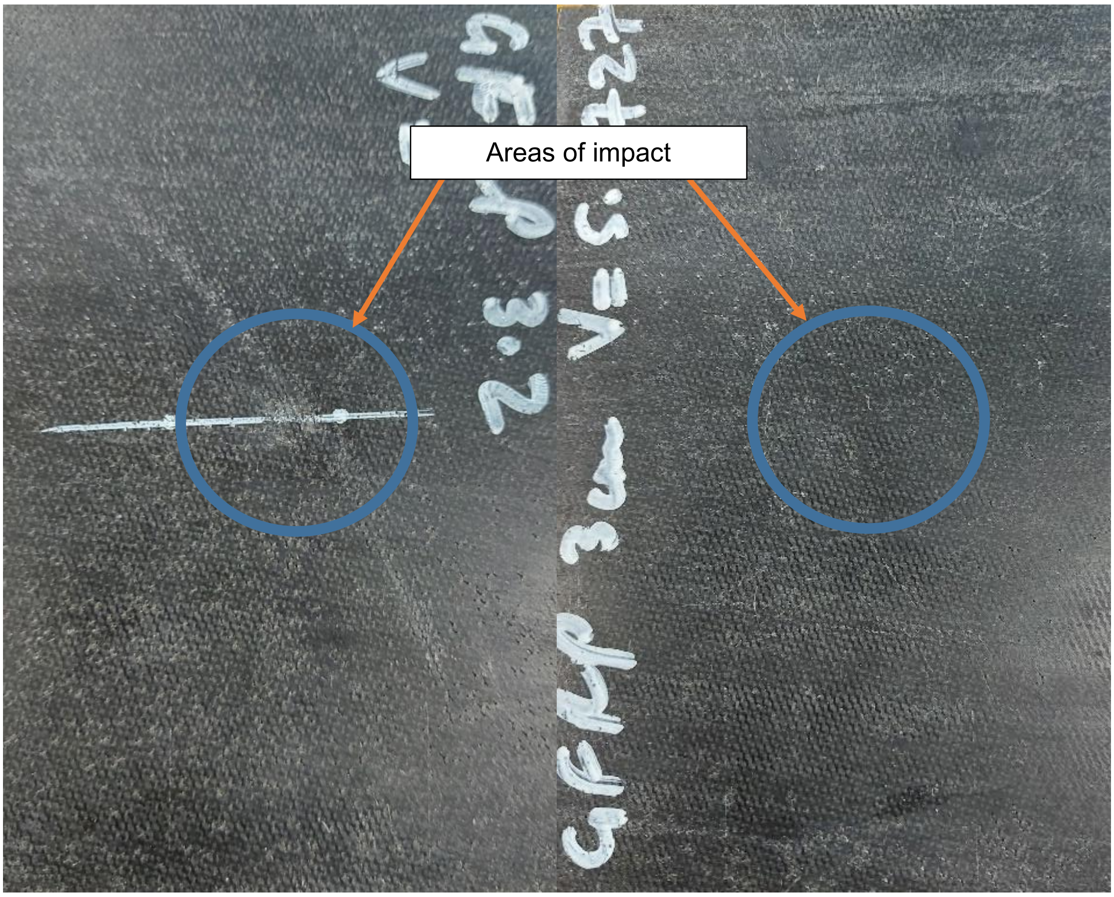

(a) Dented specimen (b) BVID specimen

Figure 4.13: GFRP damage-inflicted specimens

As shown on the specimens, visual inspection could not predict the extent of the damages on either dented specimens or specimens with barely visible impact damages. As this is the usual norm when the sandwich panels are subjected to low-velocity service impact loads, regular inspections are needed to ascertain their suitability for continued use. This study used X-ray micro-computed tomography to assess the damage inflicted on these specimens.

4.5 Identification of Damages on the Scanned Specimens with Minimal Damages

Few of the specimens were selected for inspection and assessment of damage by X-ray micro-computed tomography. The capabilities of X-ray micro-computed tomography assisted in identifying the damages that could hardly be observed by other NDT techniques, such as Thermography. This was because the specimens were made of low-density PVC foam, making it more difficult to pick up irregularities within the specimens.

4.5.1 Damage on impacted CFRP specimens

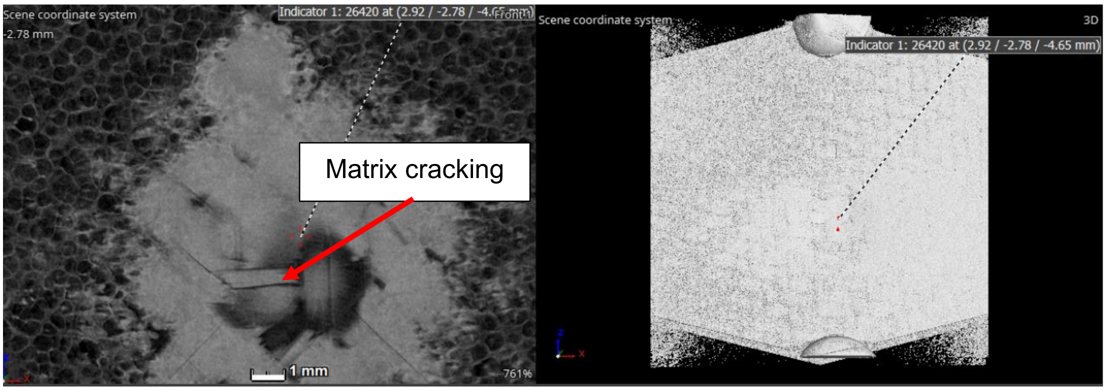

(a) Plan view (b) Isometric view

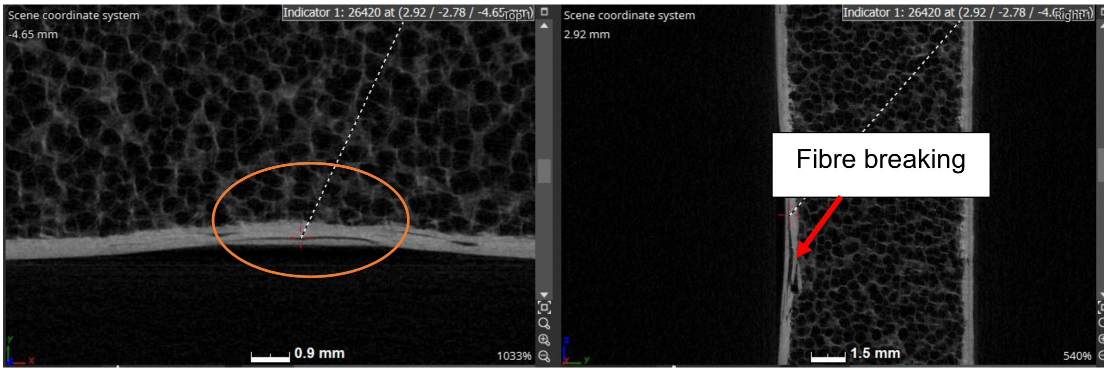

(c) Front view (d) End view

Figure 4.14: 3D views for the CFRP impacted specimens

Fibre breaking and matrix cracking were witnessed due to localised impact, while delamination weakened the entire specimen as shown in Figure 4.14. The low strain to failure of carbon fibres made it more vulnerable to fibre breakages. Due to this localised impact, deeper indentations were observed. It is evident that CFRP specimens are suspectable to impact damage. The findings of (Zhang et al., 2020) demonstrated a similar pattern of matrix cracking and fibre breakage in the CFRP skin, although their study employed a Nomex hexagonal cell honeycomb as the core material.

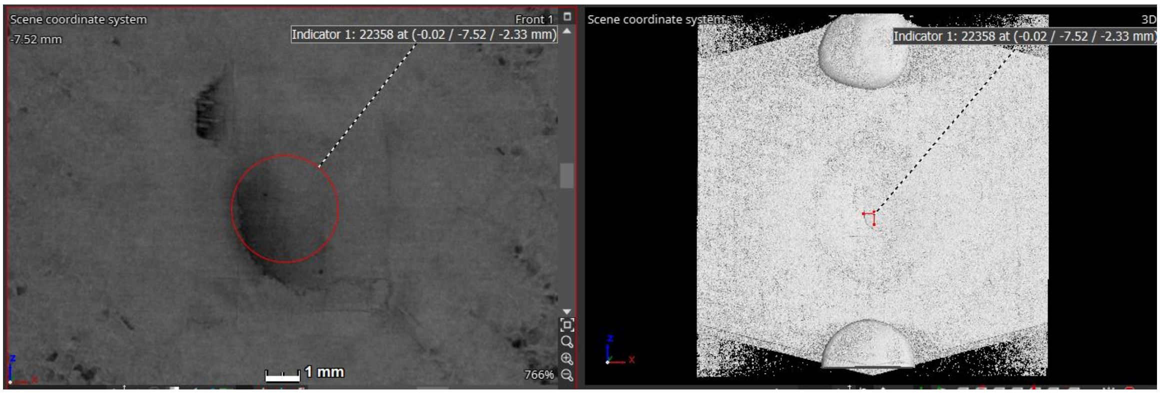

(a) Plan view (b) Isometric view

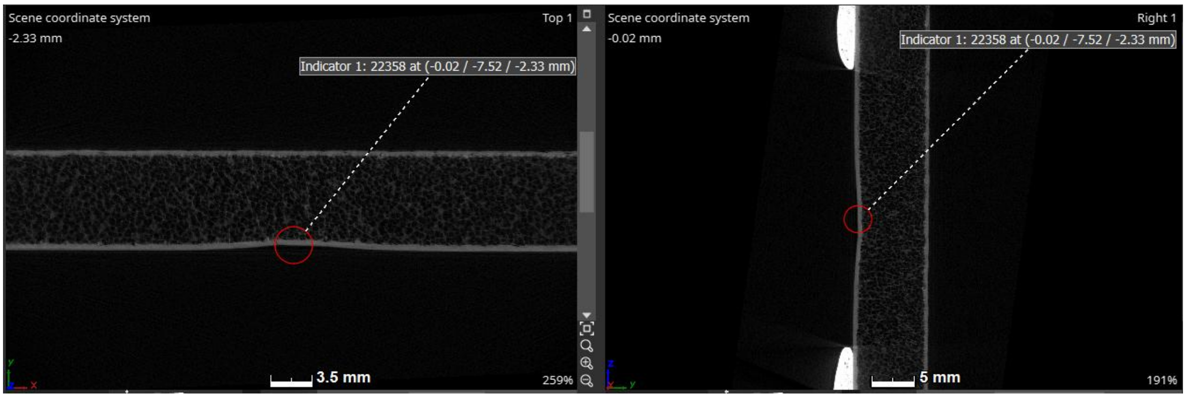

(c) Front view (d) End view

Figure 4.15: 3D views for the CFRP impacted specimens with BVID

From the inspection of the internal structure, the specimen experienced indentation with no notable damage inflicted as indicated in Figure 4.15. It is a fact, though, that damage accumulation will continue to increase over time when service loads are applied.

4.5.2 Damage on Impacted GFRP Specimens

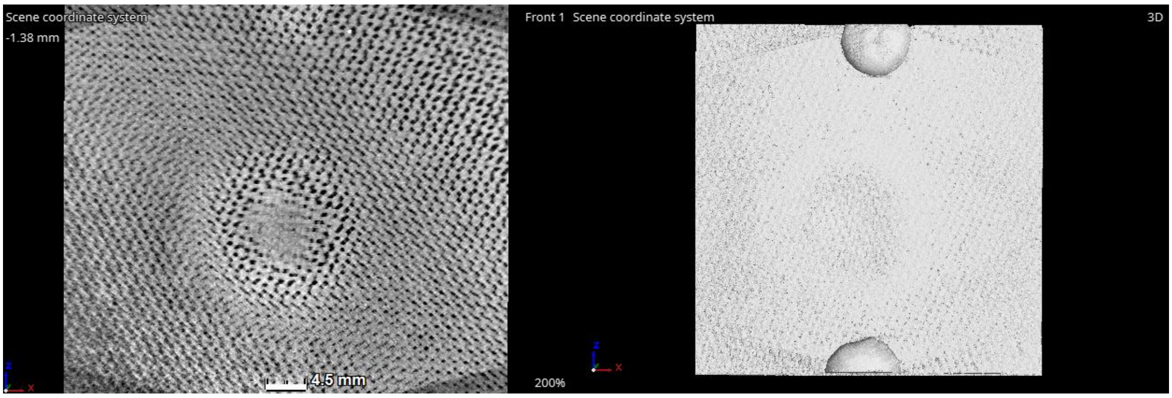

(a) Plan view (b) Isometric view

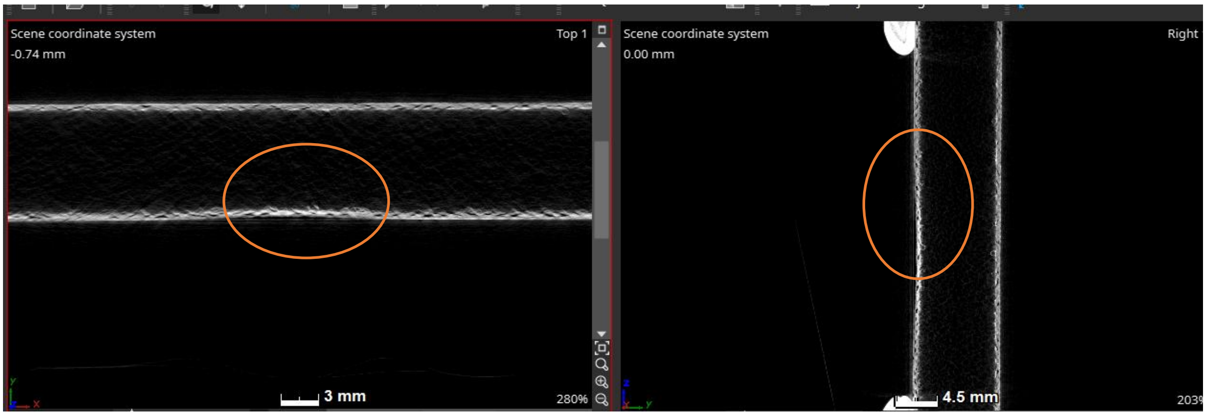

(c) Front view (d) End view

Figure 4.16: 3D views for the GFRP impacted specimens with BVID

The fibres are stretched at the impacted zone, and slight indentation is observed as shown in Figure 4.16. The same observation, though, could not be made by the naked eye, hence the BVID.

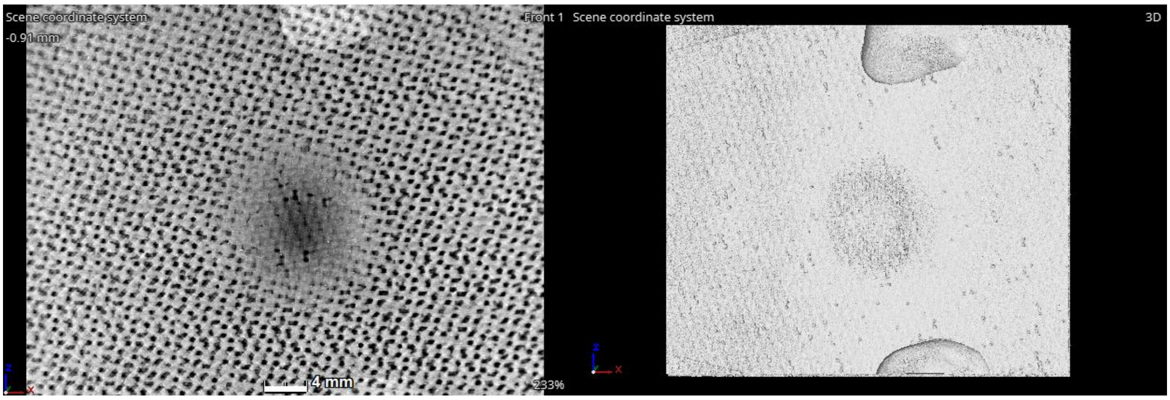

(a) Plan view

(b) Isometric view

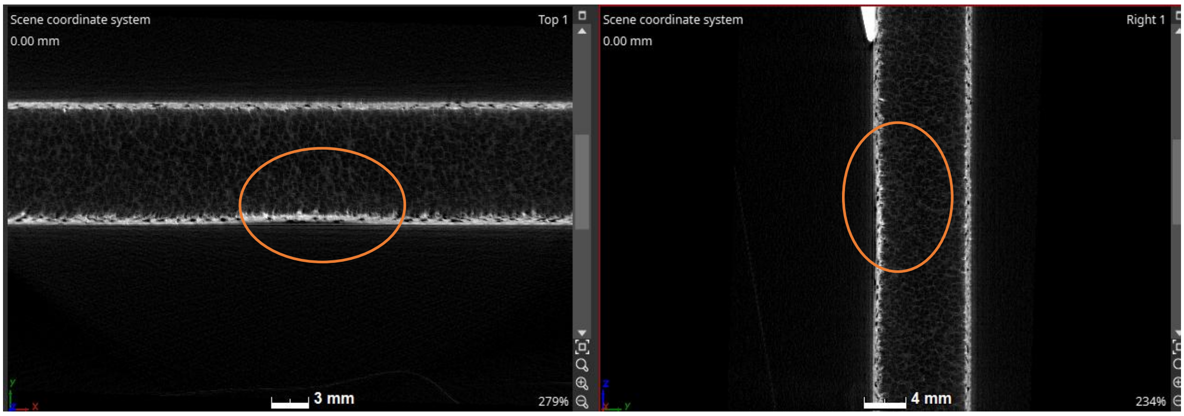

(c) Front view

(d) End view

Figure 4.17: 3D views for the GFRP impacted specimens

The damage was more pronounced but can still be classified as BVID as indicated in Figure 4.17.

4.6 Measurement of the Extent of Damage and Damage Morphologies

The extent of damage to the specimens was characterised by measuring the damaged areas and the depths of penetration. The projected damaged areas were calculated by multiplying the maximum measured lengths and widths. The projected areas were multiplied by the depth of penetration or indentation to determine the volume of the damaged areas. Further discussion on the thresholds of the BVID is covered in Chapter 5. The damage morphologies of the specimens are illustrated in Figures 4.18 and 4.19.

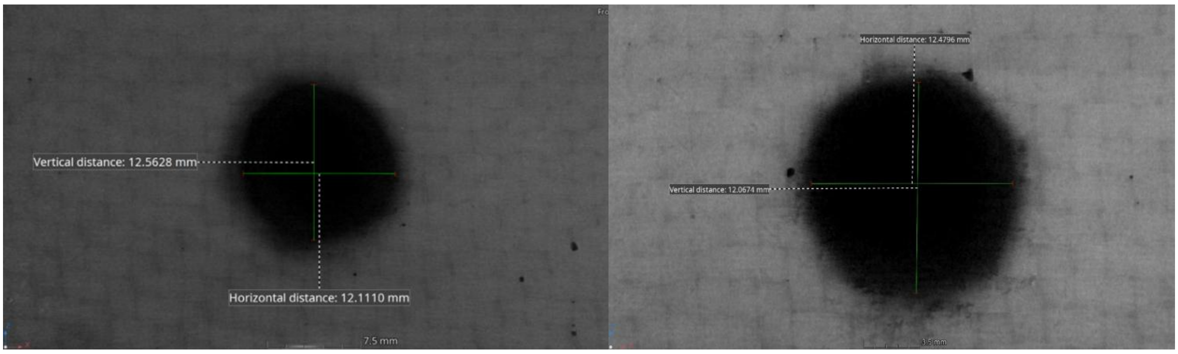

Figure 4.18: CFRP specimens progressive damaged area profiles

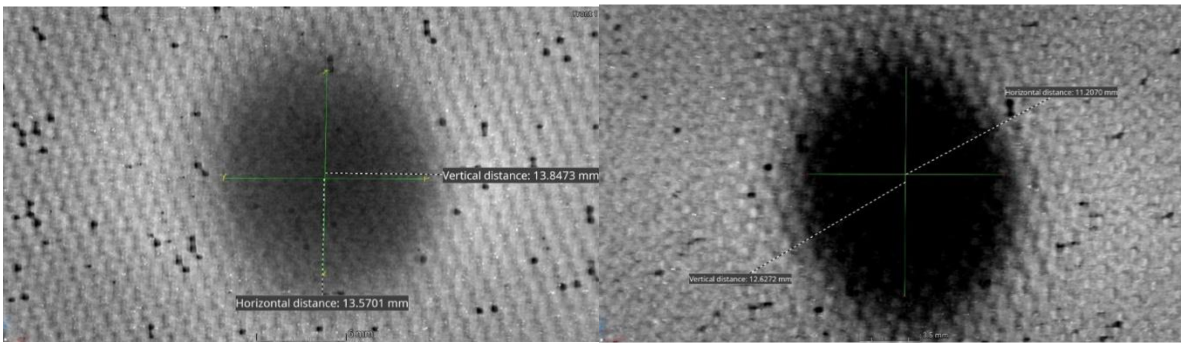

Figure 4.19: GFRP specimens progressive damaged area profiles

It was observed that the damaged areas expanded with increasing impact energies. Progressive damage was further achieved by raising the drop heights and examining the resulting damaged areas. The drop heights were increased until full perforation of the specimens was achieved, providing insights into damage accumulation. Additionally, the fully perforated specimens revealed the damage mechanisms induced on the specimens due to the impact load.

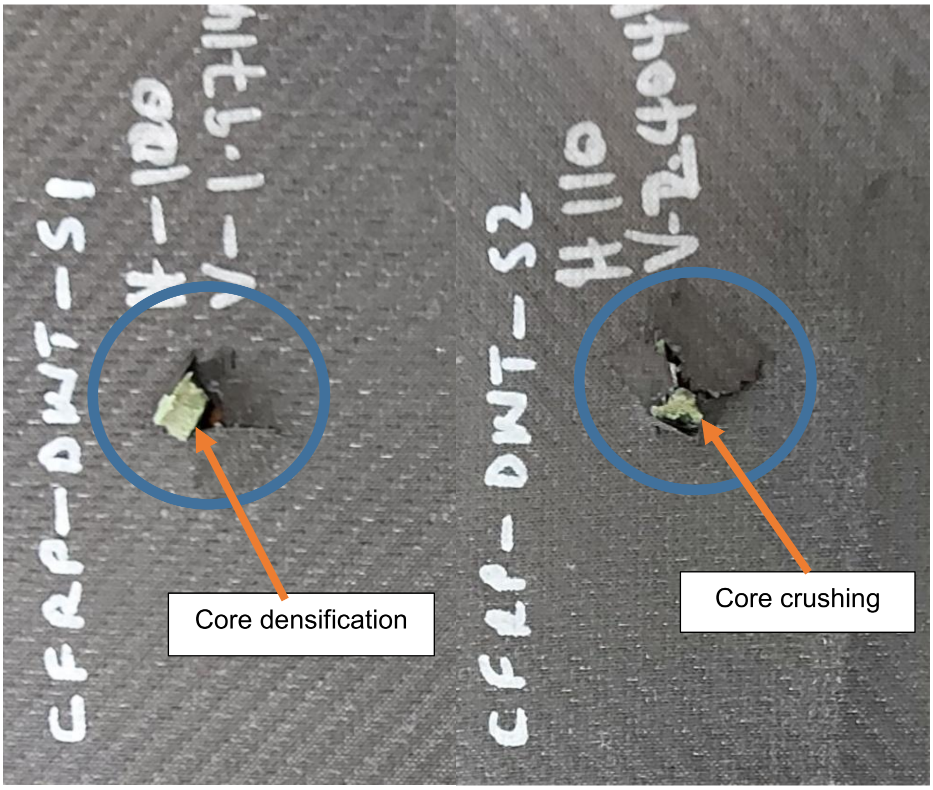

(a) (b)

Figure 4.20: Bottom side of CFRP-impacted specimens

In Figure 4.20, specimen (a) shows sheared foam and tearing or cracking action, while specimen (b) clearly shows the failure mode pattern for the specimens. It is observed that CFRP specimens exhibit a brittle nature of failure. Thus, the foam core experienced two damage mechanisms: shearing and core densification. Core densification is caused by compressive impact load exerted between the impactor and foam core. It is also evident that the higher drop height inflicts more damage to the specimens than expected. The failure pattern is a diamond shape.

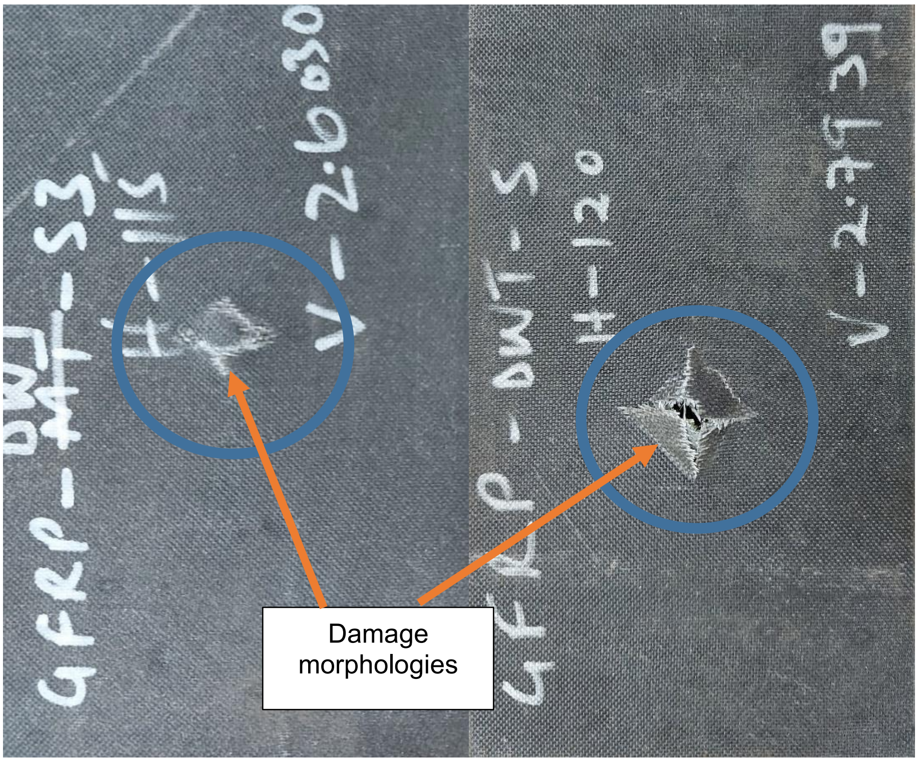

(a) (b)

Figure 4.21: Bottom side of GFRP impacted specimens

In Figure 4.21, specimen (a) shows the state of closer to full perforation, while specimen (b) illustrates full penetration of the impactor. It was anticipated that more damage would be inflicted on specimen (b) because the drop height was greater than on specimen (a). It is observed clearly at full penetration that the failure mode for these specimens forms a diamond-like shape that is more pronounced than CFRP-penetrated specimens. The failure of the fibres seems to occur at a 45° orientation. The +/-45° orientation of the stacking sequence is considered weaker than the 0° and 90° orientations. The shear action is observed at the edges. Figures 4.22 and 4.23, illustrates the progressive damage morphologies of the GFRP specimen.

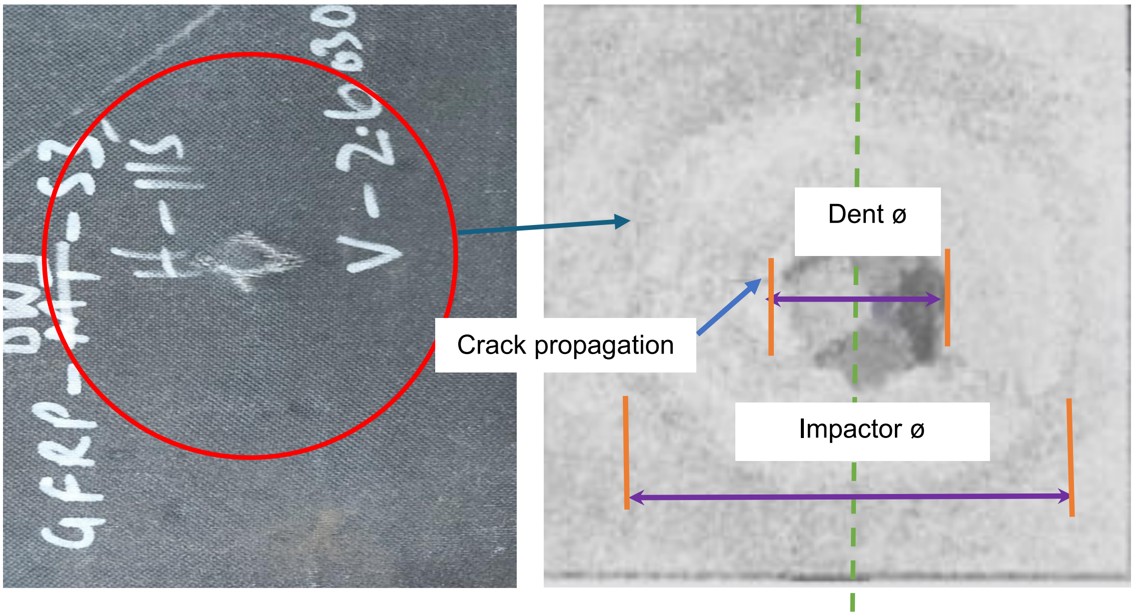

(a) (b)

Figure 4.22: (a) Near penetrated GFRP specimen (b) Relative damage morphology

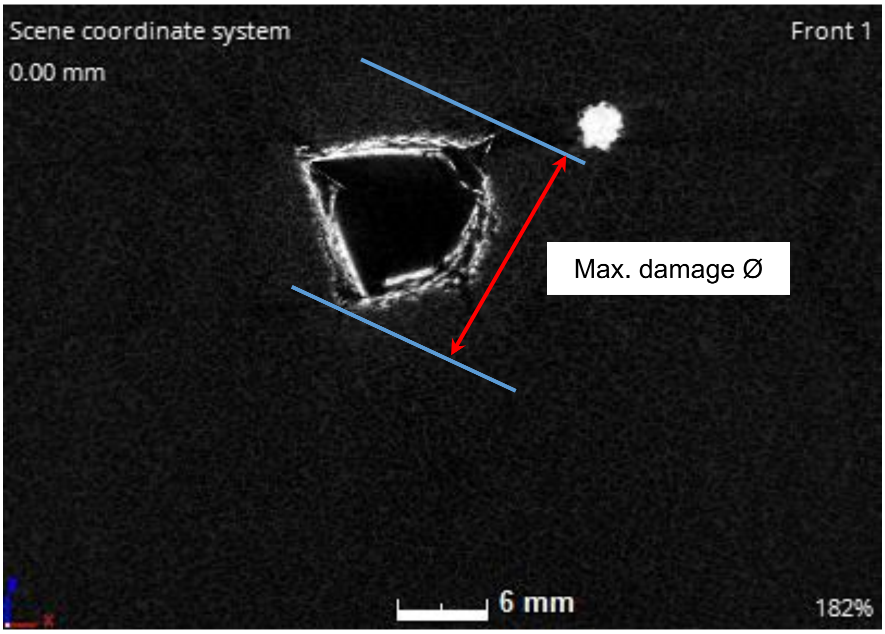

Figure 4.23: Damage morphology for the fully penetrated GFRP specimen

4.7 Failure Mode Analysis of Impacted Specimens

For both specimen types, the top face sheets did experience minimal delamination compared to the bottom face sheets. Due to the impact event, the fibres broke while the core sheared. The failure modes for both specimen types are illustrated in Figures 4.24 and 4.25.

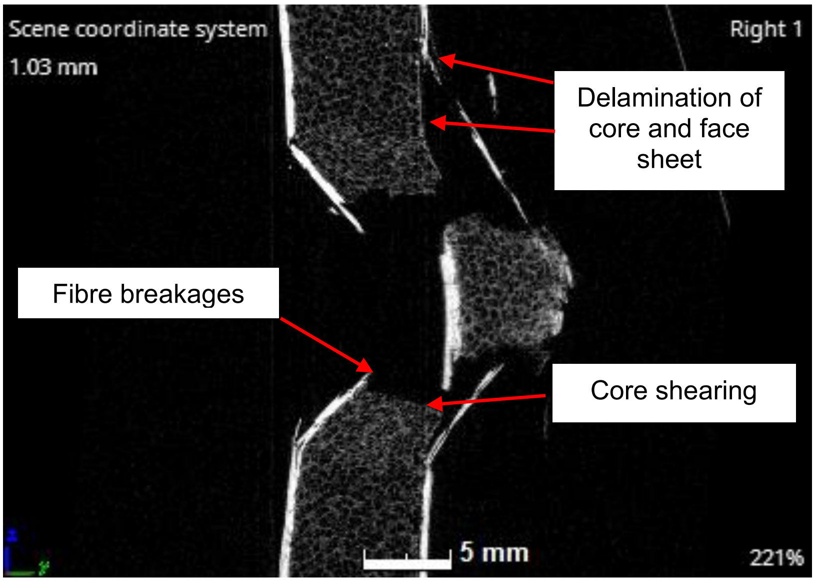

Figure 4.24: Failure modes for the CFRP specimen

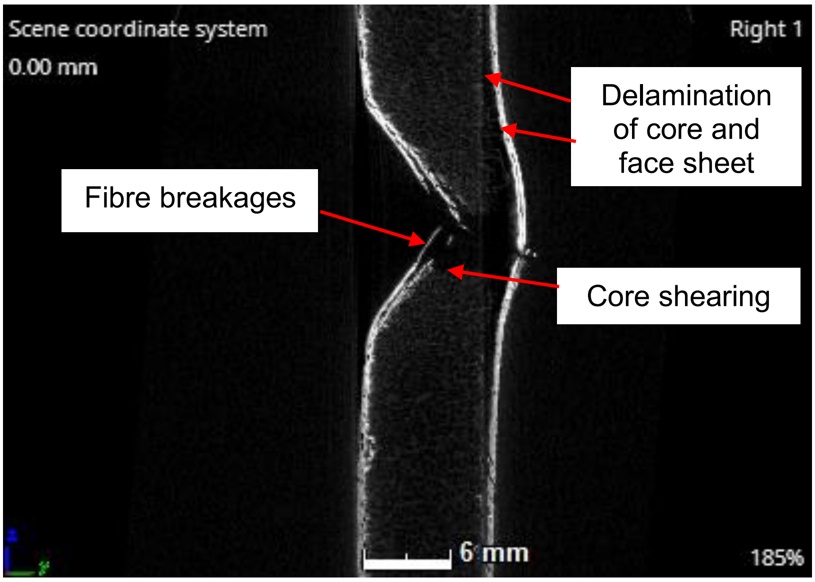

Figure 4.25: Failure modes for the GFRP specimen

The fibre breakages on the impacted specimens were localised. The identified failure modes for the impacted specimens appear similar except for the different damage morphologies. The CFRP specimen experienced minimal damage compared to the CFRP specimen. Thus, it was clear that the GFRP specimen exhibited higher damage resistance than the CFRP specimen. It can, therefore, be concluded that the dent depths are lower for GFRP-impacted specimens than for CFRP specimens at similar drop heights.

The interlaminar delamination was clearly observed using Volume Graphics VGStudio Max software, as shown in Figure 4.26. Due to the impact inflicted on the specimen, the observed interlaminar delamination is still characterised as BVID.

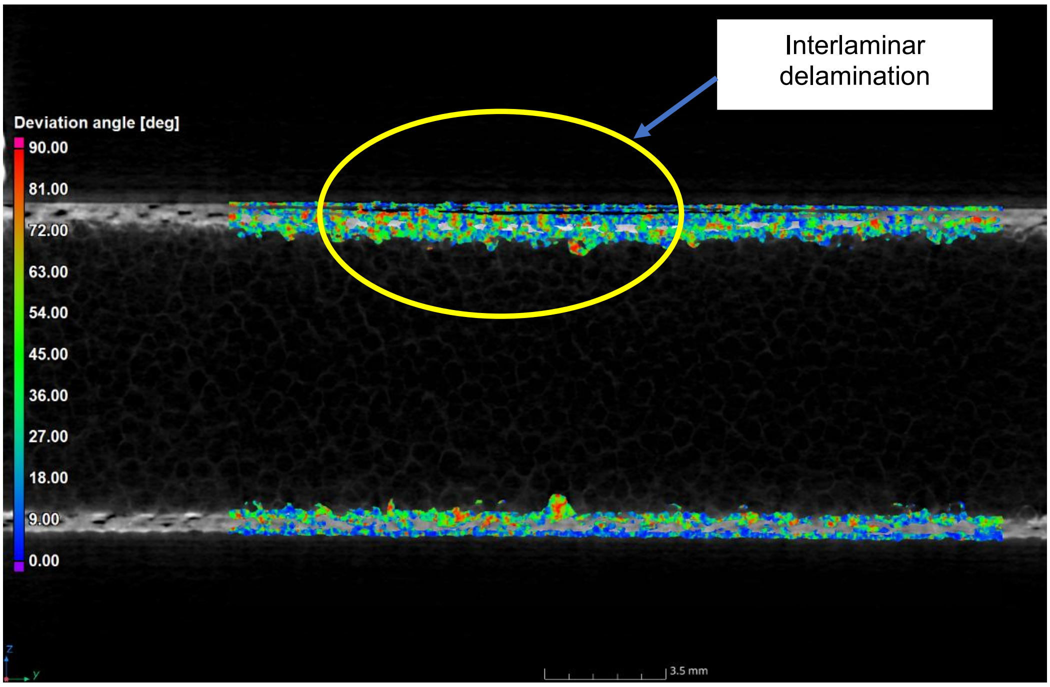

Figure 4.26: Interlaminar delamination on the GFRP specimen

4.8 Concluding Remarks

This chapter has detailed the processes undertaken, from the inspections of pristine specimens to the tests done on CFRP and GFRP specimens to characterise damage inflicted. For the tested CFRP specimens, fibre breaking and matrix cracking were witnessed due to localised impact, while delamination resulted in the weakening of the entire specimen. The low strain to failure of carbon fibres made it more vulnerable to fibre breakages. Due to this localised impact, deeper indentations were observed. On the other hand, GFRP specimens have a much higher strain of failure compared to CFRP specimens. For this reason, the impact energy can easily be dissipated to surrounding areas, causing minimal local damage. Several damage modes were identified for both specimen types in the face sheets and foam core.

In the upcoming chapter, we delve into the modelling of low velocity drop weight impact testing on the specimens. By comparing the generated numerical data with the experimental results, we aim to assess the accuracy and reliability of the numerical models in predicting damage. This validation is essential for establishing a robust correlation between experimental and numerical data, ultimately enhancing our understanding of the impact behaviour of the specimens and improving predictive capabilities for similar scenarios.

CHAPTER 5

MODELLING OF DAMAGE IN SANDWICH PANELS USING THE 3D HASHIN CRITERIA

5.1 Introduction

This chapter presents a comprehensive damage modelling approach for sandwich structures, aimed at elucidating the evolution of failure mechanisms under impact loading. The 3D Hashin failure criteria were employed to predict damage initiation and progression within the composite laminates. These criteria were integrated into a progressive damage model via a VUMAT subroutine in Abaqus Explicit, enabling detailed finite element simulations. The PVC foam core was modelled using a crushable plasticity framework that incorporates both ductile and shear damage responses during impact events. This integrated modelling strategy revealed distinct and interacting failure modes in both the laminate skins and the foam core.

Modelling of damage in sandwich composite structures is a complex yet critical aspect of materials engineering. It involves using computational tools to predict how damage initiates, evolves, and affects the overall structural integrity of composite materials. This predictive capability is vital for designing safer and more reliable structures across various industries. The modelling of sandwich composite structures presents significant challenges that include:

Material Complexity: The heterogeneous nature of sandwich composites, which combine stiff face sheets with a lightweight core, introduces complexities in accurately predicting their behaviour. Each component may have vastly different mechanical properties, and their interactions can lead to non-linear and anisotropic behaviour, which is difficult to simulate. This complexity is compounded by various failure mechanisms, such as face sheet cracking, core crushing, and face/core debonding, which can simultaneously affect the structure in different ways.

Computational Demand: Capturing all the intricacies of damage in sandwich composites requires detailed models that can account for the various potential failure modes and material behaviours at different scales. This level of detail can lead to enormous computational models with many degrees of freedom, necessitating significant computational resources and time. As a result, the computational cost can become a limiting factor, especially when attempting to model large or complex structures.

Validation Challenges: Experimental validation of the models is crucial to ensure their accuracy and reliability. However, due to the complexity of damage mechanisms in sandwich composites, gathering comprehensive experimental data is difficult. Damage can begin at a microscopic level and may not be detectable until it has progressed to a macroscopic scale. Additionally, replicating the exact conditions and failure modes in a laboratory setting is challenging. The discrepancies between model predictions and experimental observations must be reconciled to refine the models and improve their predictive capabilities. Figure 5.1 shows the proposed conceptual modelling framework.

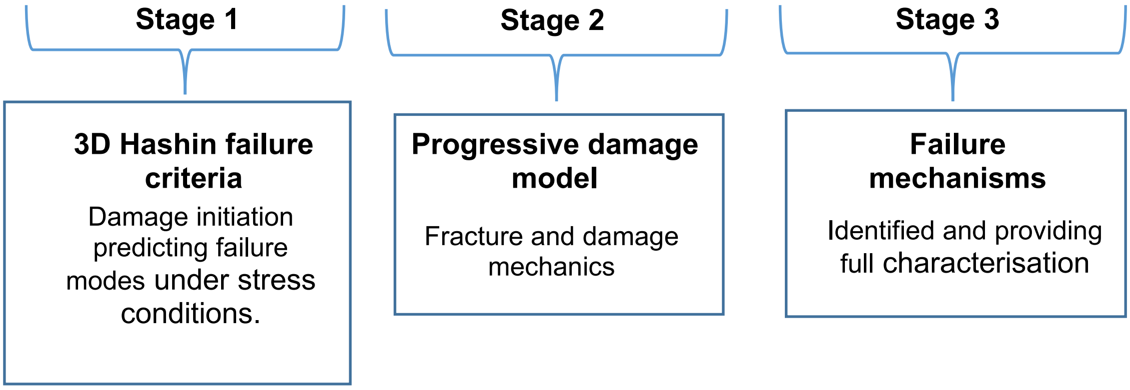

Figure 5.1: Proposed conceptual framework for damage modelling

The rationale for using the 3D Hashin VUMAT Subroutine as opposed to Abaqus Hashin Damage are:

i) The 3D Hashin Failure criterion is not supported in the Abaqus explicit solver for solid elements, hence the development of the Abaqus subroutine.
ii) It provides more accurate predictions of failure in composites by capturing all stress states, including inelastic and out-of-plane deformation.

5.2 Damage Initiation and Propagation

The Hashin Failure Criteria, introduced by Zvi Hashin in the 1980s, is a set of criteria used to predict the failure of fibre-reinforced composite materials. The simplified explanation of the Hashin Failure Criteria for both 2D (planar) and 3D (volumetric) aspects of composite materials is covered as follows:

1. ***2D Hashin Failure Criteria***: In two dimensions, the Hashin criteria distinguish four types of failure modes: fibre tension, fibre compression, matrix tension, and matrix compression (Hashin, 1980).For each mode, a different failure criterion is specified. The criteria are inequality conditions derived from the material's stress tensor components. These conditions must be checked for all four failure modes, and the material is considered to fail when the first criterion is met.
2. ***3D Hashin Failure Criteria****:* The Hashin criteria become more complex in three dimensions because they must account for out-of-plane and shear stresses in three dimensions. The extension to three dimensions still distinguishes the same four failure modes but now involves a more complex set of inequality conditions based on the 3D stress tensor. As with the 2D case, the material is assumed to fail when the first criterion is met.

Hashin’s criteria differentiate between failure modes in fibre and matrix materials, as described below.

a. *Fibre Tension (along fibre direction)*: Failure is predicted when the longitudinal tensile stress exceeds the tensile strength of the fibre.
b. *Fibre Compression (along fibre direction)*: Predicts failure when the compressive stress in the fibre direction exceeds the fibre’s compressive strength.
c. *Matrix Tension (perpendicular to fibre direction)*: Occurs when the transverse tensile stress exceeds the tensile strength of the matrix.
d. *Matrix Compression (perpendicular to fibre direction)*: Predicts failure under transverse compressive stress, which could lead to buckling or kinking of the fibres.
e. *Shear*: Addresses the shear stress state in the material and predicts failure when the shear stress exceeds the shear strength of the matrix or the fibre-matrix interface.

Hashin's criteria are based on the assumption that different failure modes are independent and can be evaluated separately. The presentation for the formulations is described below:

Hashin 2D failure

Fibre failure under tension, ($\sigma_{11} > 0$):

$$\left(\frac{\sigma_{11}}{X_t}\right)^2 + \alpha\left(\frac{\tau_{12}}{S_l}\right)^2 = 1 \qquad (5.1)$$

Fibre failure under compression, ($\sigma_{11} < 0$):

$$\left(\frac{\sigma_{11}}{X_c}\right)^2 = 1 \qquad (5.2)$$

Matrix failure under tension, ($\sigma_{22} > 0$):

$$\left(\frac{\sigma_{22}}{Y_t}\right)^2 + \left(\frac{\tau_{12}}{S_l}\right)^2 = 1 \qquad (5.3)$$

Matrix failure under compression, ($\sigma_{22} < 0$):

$$\left(\frac{\sigma_{22}}{2Y_t}\right)^2 + \left[\left(\frac{Y_c}{2S_t}\right)^2 - 1\right]\left(\frac{\sigma_{22}}{Y_t}\right)^2 + \left(\frac{\tau_{12}}{S_l}\right)^2 = 1 \qquad (5.4)$$

Hashin 3D failure

The three-dimensional state of stress adopted in this study describes and captures all possible failure mechanisms in all directions. Figure 5.2 shows the state of stress for the three-dimensional configuration.

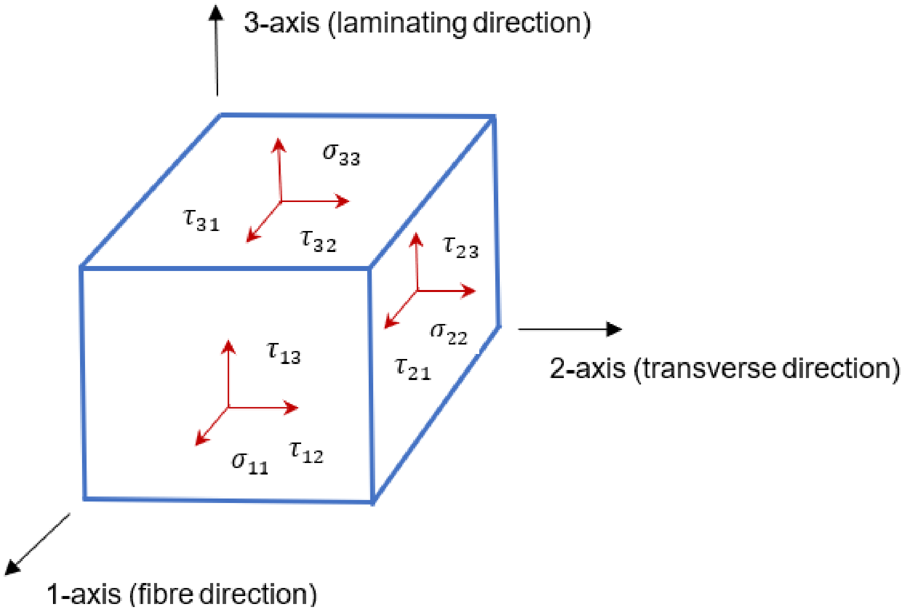

Figure 5.2: 3D state of stresses

Fibre failure under tension, $(\sigma_{11} \geq 0)$:

$$\left(\frac{\sigma_{11}}{X_t}\right)^2 + \left(\frac{\tau_{12}}{S_{12}}\right)^2 + \left(\frac{\tau_{13}}{S_{13}}\right)^2 = 1 \qquad (5.5)$$

Fibre failure under compression, $(\sigma_{11} < 0)$:

$$-\sigma_{11} = X_c \qquad (5.6)$$

Matrix failure under tension, $(\sigma_{22} + \sigma_{33} \geq 0)$:

$$\left(\frac{\sigma_{22} + \sigma_{33}}{Y_t}\right)^2 + \frac{{\tau_{23}}^2 - \sigma_{23}\sigma_{33}}{{S_{23}}^2} + \left(\frac{\tau_{12}}{S_{12}}\right)^2 + \left(\frac{\tau_{13}}{S_{13}}\right)^2 = 1 \quad (5.7)$$

Matrix failure under compression, $(\sigma_{22} + \sigma_{33} < 0)$:

$$\left[\left(\frac{Y_c}{2S_{23}}\right)^2 - 1\right]\frac{\sigma_{22} + \sigma_{33}}{Y_c} + \left(\frac{\sigma_{22} + \sigma_{33}}{2S_{23}}\right)^2 + \frac{{\tau_{23}}^2 - \sigma_{23}\sigma_{33}}{{S_{23}}^2} + \left(\frac{\tau_{12}}{S_{12}}\right)^2 + \left(\frac{\tau_{13}}{S_{13}}\right)^2 = 1 (5.8)$$

Where:

X_t is the longitudinal tensile strength.

X_c is the longitudinal compressive strength.

Y_t is the transverse tensile strength.

Y_c is transverse compressive strength.

S_{12} and S_{13} are the longitudinal shear strengths.

S_{23} and S_{21} are the transverse shear strengths.

Progressive Damage Modelling (PDM)

Progressive damage models integrate the constitutive laws with damage evolution equations that predict the growth of damage under cyclic or dynamic loading. Damage or internal state variables are often introduced to quantify the extent of damage in the material and how it evolves with continued loading. These damage variables modify the constitutive laws to degrade the material properties as damage progresses, reflecting the reduced stiffness and strength of the material.

5.3 Constitutive Laws

Material constitutive laws are foundational in the progressive damage modelling of sandwich composite structures. These laws describe how materials respond to different stress states and are essential for predicting the behaviour of materials under various loads and conditions. In the context of sandwich composites, which consist of different materials with potentially complex interactions, the constitutive laws need to capture the behaviour of each component (face sheets and core) and their interactions.

Face Sheets Constitutive Laws

The face sheets are typically made of fibre-reinforced polymers, and the constitutive laws must capture the anisotropic behaviour of these materials. The laws must be able to capture both in-plane strength and out-of-plane stresses under multiaxial states. In this study, the face sheets are modelled as orthotropic materials that consider anisotropy in the three mutually perpendicular axes.

Core Material Constitutive Laws

Constitutive laws for the core are typically designed to handle large deformations, often focusing on shear behaviour, as the core is primarily responsible for absorbing shear stresses between the face sheets. Compressive failure models are also crucial, as the core can be prone to local buckling or crushing under compressive loads. Foam materials are the focus of this research, and their properties and performance under varying impact loading need precise modelling.

Interface Constitutive Laws

Interface Elements with Damage Mechanics: Damage mechanics was incorporated into interface elements to describe the degradation of properties at the interface due to loading. This approach allows for the progressive failure of the interfaces at the laminate (intralaminar failure) and laminate-core (interlaminar failure) levels. The constitutive formulation laws used in this study are provided in Appendix B.

5.4 Linking Fortran Compiler to Abaqus

In the context of this work, the progressive damage model that incorporates the combined 3D Hashin criteria was implemented through a subroutine in Finite Element Analysis (FEA) Abaqus Explicit. This damage progression framework is distinguished by its ability to offer a comprehensive approach to understanding material degradation of both the fibre and matrix. A user-defined subroutine enabled the simulation and analysis of material behaviour under impact loading conditions.

Running simulations with a VUMAT subroutine was facilitated by linking a Fortran Compiler to Abaqus. The process of linking was achieved by downloading Microsoft Visual Studio 2022 version that has a special component of “Desktop Development with C++” and Intel oneAPI HPC Toolkit (Base kit + HPC kit). For customised installations, the Base kit must have Intel oneAPI Threading Building Blocks and Intel oneAPI DPC ++/C++ Compiler, while the HPC kit must have Intel oneAPI DPC ++/ C++ Compiler and Intel C++ Compiler Classic and Intel Fortran Compiler (Beta) and Intel Fortran Compiler Classic. The Abaqus 2023 version was installed with CAA API component, and verification of its existence in the software is done by running the software manager. On checking the verification of the installations to run the simulations, the following outcome was observed, as provided in Table 5.1.

Table 5.1: Final System Configuration

OS Version	Windows 10 Enterprise (Build 19041)
C++ Compiler	Microsoft Visual C++ 14.38.33134.0
Linker Version	Microsoft (R) Incremental Linker Version 14.38.33134.0
Fortran Compiler	Intel Fortran Compiler 2021.11
MPI	MS-MPI 10.1.12498.18

5.5 Modelling Procedure

The VUMAT Abaqus code used for conducting the simulations is provided in Appendix C.

At the beginning of the analysis, the materials under consideration are assumed to be purely elastic.

The number of state variables and controlling element deletions are 17 and 5, respectively. The user-defined material properties for GFRP and CFRP are detailed in Table 5.2. However, GFRP material properties were used to validate the models.

A distinction was made between failure and no failure by assigning the values 1 and 0, respectively, for the four possible fibre and matrix failure modes during the impact event. The damage variables for both fibre and matrix are introduced in the damage matrix to capture the mechanical behaviour changes by degrading the compliance and stiffness matrices. The formulation of these matrices is provided in Appendix B.

The implementation of the code was accomplished through the VUMAT in Abaqus Explicit. The adopted process of implementing the VUMAT is illustrated in Figure 5.3.

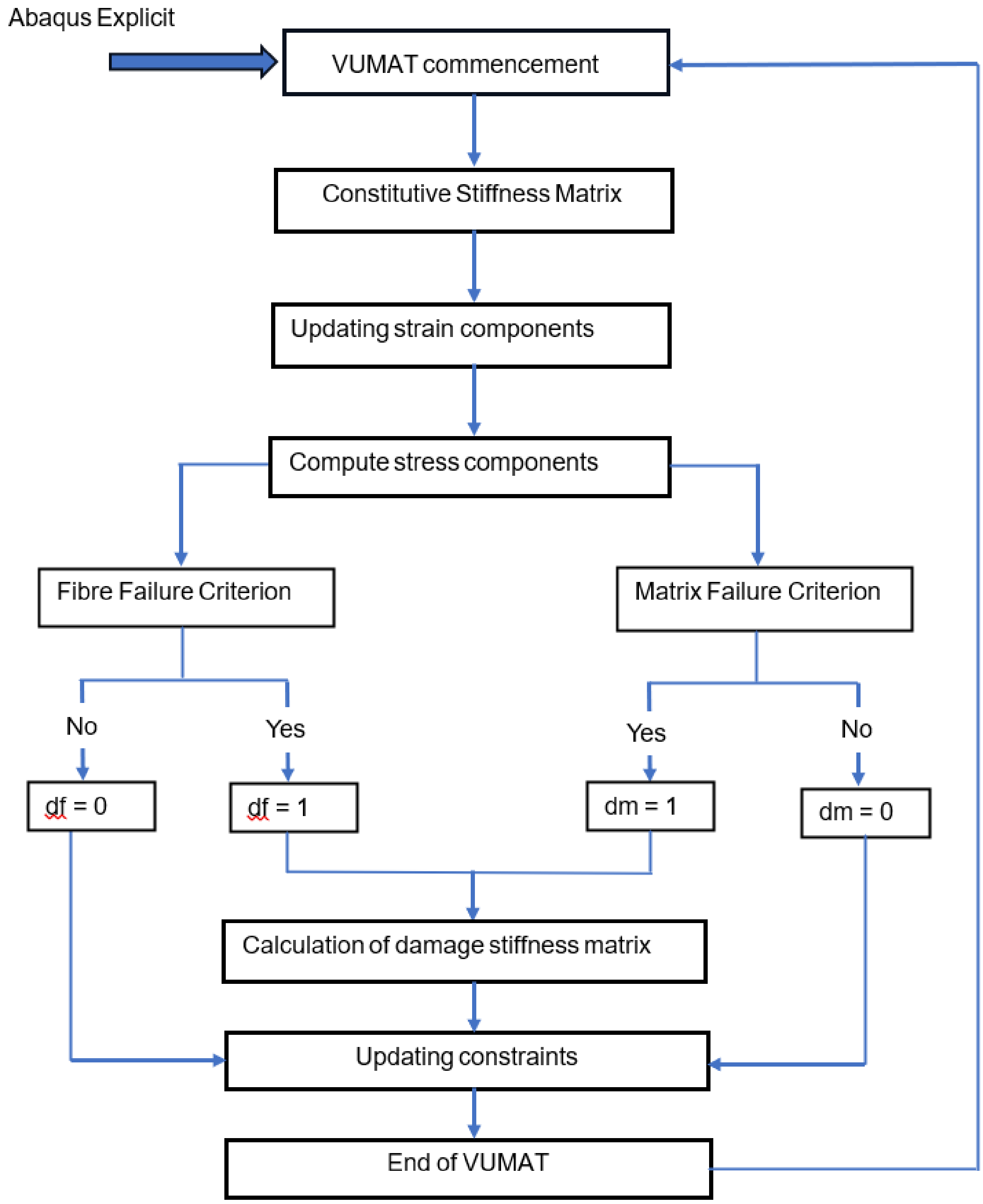

Figure 5.3: Implementation of damage model with VUMAT in Abaqus

In this section, the drop weight impact simulations are conducted for purposes of comparing with the experimental results. The comparisons are focussed on understanding the responses to low velocity impact, damage morphologies and the associated damage mechanisms created during the impact event. Thus, the mode dependent approach was adopted in this study to unmask the complexities associated with failure of both the matrix and fibre during impact.

The simulations adhered to the ASTM D7136/7136M-15 standard that is provided for carrying out drop weight impact tests on fibre reinforced composites. The dimensions of the specimens are 150 mm x 100 mm as per this standard. Due to symmetry and the fact that the specimen was impacted at the centre, only a quarter of the specimen was modelled. This condensed model as depicted in Figure 5.4, with dimensions of 62.5 mm x 37.5 mm, efficiently captured the behaviour of the panel during the impact event. In addition to providing an equally reliable analysis, this reduced model yielded the added benefit of diminished computational expenses, thus optimising the simulation process.

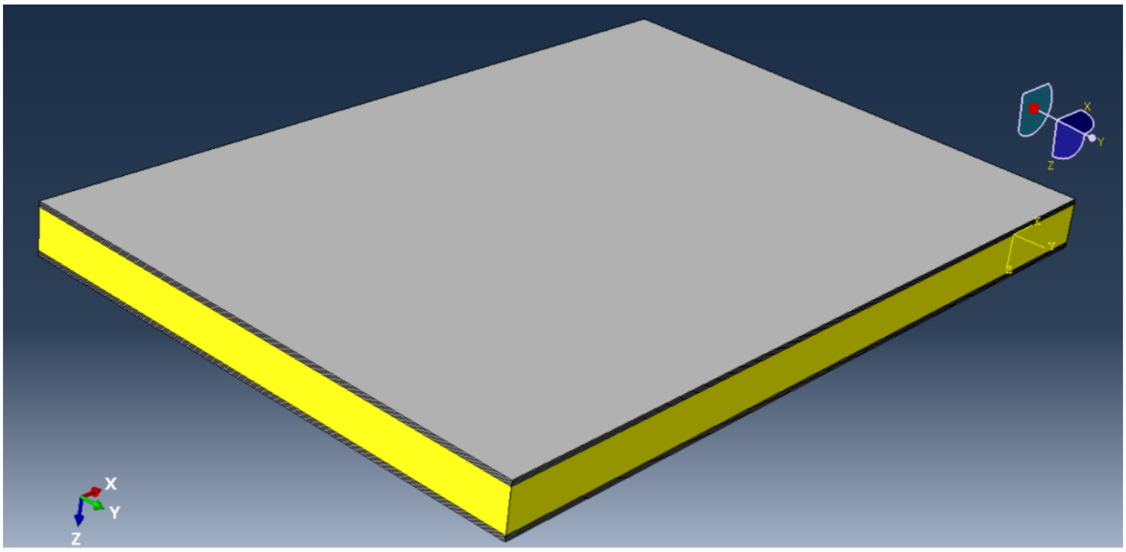

Figure 5.4: ABAQUS Sandwich Panel Model

Impactor

A hemispherical discreet rigid body impactor of diameter 12.5 mm and a quarter mass of 1.4025 kg was used for the simulations to exhibit non-deformable behaviour. The mass was inputted as a special inertia at the reference point through the centre of gravity. The material constituents of the sandwich panel are discussed below.

Face sheet types: Carbon fibre reinforced plastic (CFRP) and Glass fibre reinforced plastic (GFRP)

The stacking sequence for both: [(0/90), (+45/-45)/ 9 mm PVC foam core/ (-45/+45), (90/0)]. This stacking sequence can be shortened to $[0/90/+45/-45]_s$. The ply thickness was 0.25 mm.

The specifications/properties for face sheets and foam core are provided in Tables 5.2 and 5.3, respectively.

Table 5.2: Properties of (UD) GFRP and CFRP

Lamina Constants			**Constitutive Damage Model Parameters of Lamina**			
	GFRP	**CFRP**			**GFRP**	**CFRP**
E_{11}, GPa	36.9	105.5	Long. tens strength, MPa	X_T	820	1340
E_{22}, GPa	10	7.2	Long. compres strength, MPa	X_C	500	1192
E_{33}, GPa	10	7.2	Transverse tens strength, MPa	Y_T	80.6	19.6
G_{12}, GPa	3.3	3.4	Transv compre strength, MPa	Y_C	322	92.3
G_{13}, GPa	3.3	3.4	Long. shear strength, MPa	S_L	54.5	51
G_{23}, GPa	3.6	2.52	Trans. shear strength, MPa	S_T	161.2	23
v_{12}	0.32	0.34	Long. tens fract. energy, N/mm	G_{XT}	32	48.4
v_{13}	0.32	0.34	Long. comp fract. energy, N/mm	G_{XC}	20	60.3
v_{23}	0.44	0.378	Trans tens fract. energy, N/mm	G_{YT}	4.5	4.5
			Trans comp fract. energy, N/mm	G_{YC}	4.5	8.5

Source: Koloor et al. (2020)

Foam core type: *PVC (Polyvinyl Chloride)*

A cross-linked, closed-cell PVC foam of 9 mm thickness was used to construct the sandwich composite structure. The specifications of this foam core, as per the data sheet, are given in Table 5.3 below.

Table 5.3: Properties of PVC foam core as per data sheet

Variant	**Nominal Density** (1)	**Density Range** (1)	**Compr Strength** (2)	**Compr Mod** (2)	**Shear Strength** (3)	**Shear Mod** (3)	**Tens Strength** (4)	**Tens Mod** (4)
M080	80	72 - 92	1.6 (1.42)	97 (76)	1.2 (1.07)	30 (26)	2.74 (2.28)	146 (94)

Note: ***(1)*** *Density is in kg/m^3* ***(2)*** *Stresses in MPa* ***(3)*** *All values in brackets are minimum values.*

The inputted foam properties are presented in Table 5.4.

Table 5.4: Summarised Foam Properties

E1 (MPa)	E2 (MPa)	E3 (MPa)	N12	N13	N23	G12 (MPa)	G13 (MPa)	G23 (MPa)
146	97	97	0.38	0.38	0.42	30	30	16.8

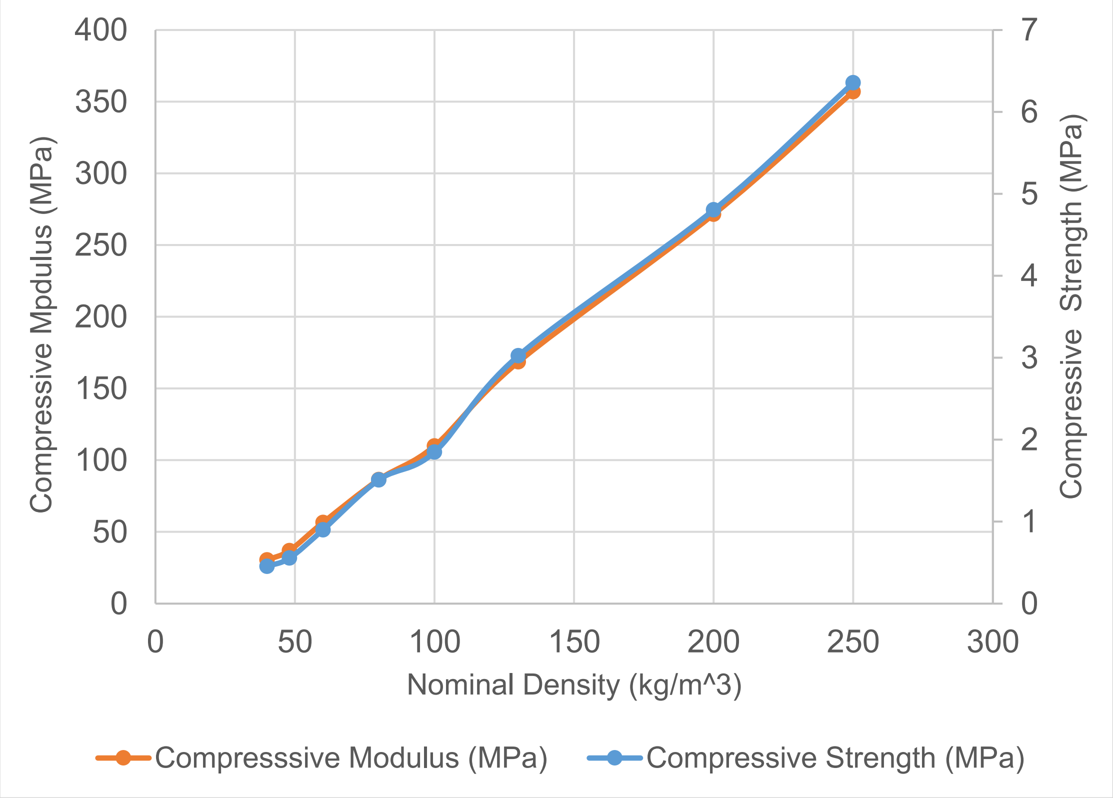

Figure 5.5: Influence of Nominal Density on Compressive Modulus and Compressive Strength

According to the density range provided in the data sheet, the compressive modulus shows a more significant increase compared to the compressive strength, as depicted in Figure 5.5. Below a nominal density of 130 kg/m³, the compressive strength and modulus increase non-uniformly. However, above this density, the increase becomes approximately linear. At a nominal density of 80 kg/m³, which is the density of the foam used in this study, the trends for both compressive modulus and strength coincide. This indicates that the same degradation pattern is followed during the impact event.

The typical compressive stress-strain curve for the foam is characterised by three stages, namely:

a. The linear elastic in which small strains below 5% allow elastic deformation due to cell wall bending.
b. Plastic plateau where deformation occurs at almost constant stress caused by elastic buckling of cell edges or walls, thereby significantly reducing the volume of the foam.
c. Densification that occurs where the cell walls crush together, causing an exponential increase in compressive stress and constant volume.

Since the fracture toughness for the M80 series was not known, it was compared to the H80 series, which had a known fracture toughness value. Saeid and Donaldson, (2016) provided data for a closer foam type (H series) of the same density that is comparable to the foam type (M series) used in this investigation. The nominal properties for the M80 series were averaged values. The purpose of the comparison was to determine the possible influence of the properties on the fracture toughness and estimate the fracture toughness of Mycell M080. The fracture toughness for the Divinycell H80 series was found to be $1.86 \pm 39\, J/m^2$ in the first mode (Viana & Carlson, 2002).Noury et al. (1998) investigated the mixed-mode fracture in rigid cellular PVC foam and obtained a ratio of fracture toughness between Mode II and Mode I in the range of 0.4 to 0.65, depending on density. Thus, the Mode II fracture toughness can be estimated. The data pertaining to the Mode III fracture toughness is still scarce in the literature. In the absence of such data, it is probably accepted to assume that fracture toughness of mode III and mode I vary in the same range as mode II and mode I, as described above, albeit linearly. The relationship between fracture toughness in Mode I, Modes II and III can vary depending on factors such as the foam's density, the size and distribution of its cells, and the direction of the applied stress relative to the foam's structure (Funari et al., 2021).

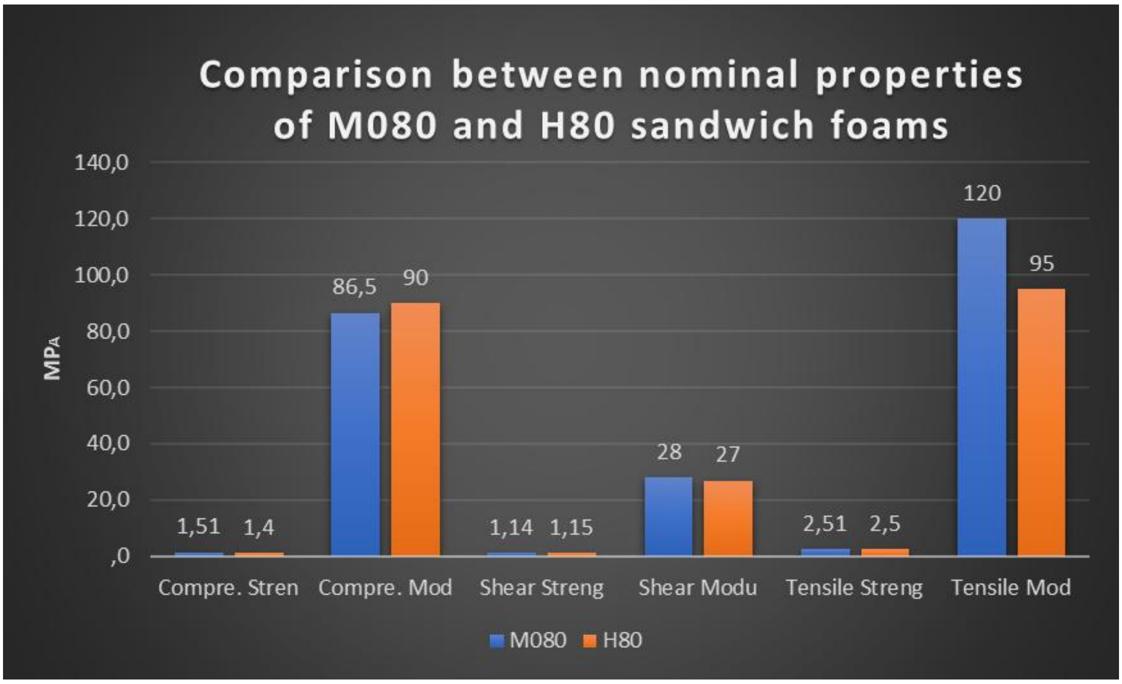

Figure 5.6: Comparison between normal properties of M080 and H80 sandwich foams

The major noted difference between the foams is the tensile modulus, with a 20,83% difference, while the other properties have less than 8% difference. It can, therefore, be assumed that the fracture toughness is the same. Furthermore, for this comparison, as shown in Figure 5.6, the M series exhibits a higher strain rate than the H series. However, further studies must be conducted to reach a generalised conclusion for different densities.

Generally, the Griffith criterion can be used to determine the fracture toughness of the composite structure. The delamination was predicted using the cohesive zone model (CZM), which accounts for the initiation and evolution of delamination. Damage initiation was governed by the quadratic failure criteria, while damage propagation was controlled by the Benzeggah-Kenane (BK) criterion incorporated in Abaqus. A B-K value of 1.45 was used in this study. A stress-based quadratic traction-separation law for delamination initiation is: $\left(\frac{t_n}{N}\right)^2 + \left(\frac{t_s}{S}\right)^2 + \left(\frac{t_t}{T}\right)^2 \geq 1$ (5.5)

Where t_n, t_s and t_t are the interface stresses in the normal and two shear directions, respectively, and N, S and T the corresponding interface strength.

Delamination propagation under the mixed-mode loading was modelled by the following interactive criterion: $\left(\frac{G_I}{G_{IC}}\right) + \left(\frac{G_{II}}{G_{IIC}}\right) + \left(\frac{G_{III}}{G_{IIIC}}\right) \geq 1$ (5.6)

Where G_I, G_{II} and G_{III}a are the strain energy release rates under mode I, II and III respectively, G_{IC}, G_{IIC} and $G_{IIIC}$the critical strain energy release rates.

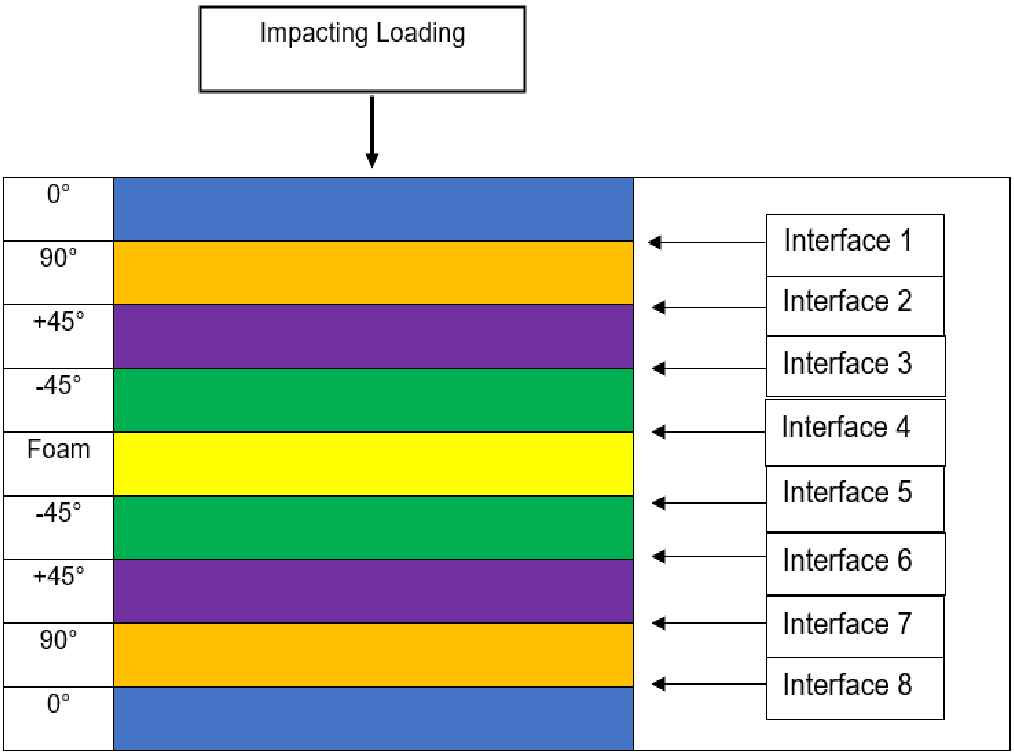

Figure 5.7: Schematic of model stacking sequence and interfaces

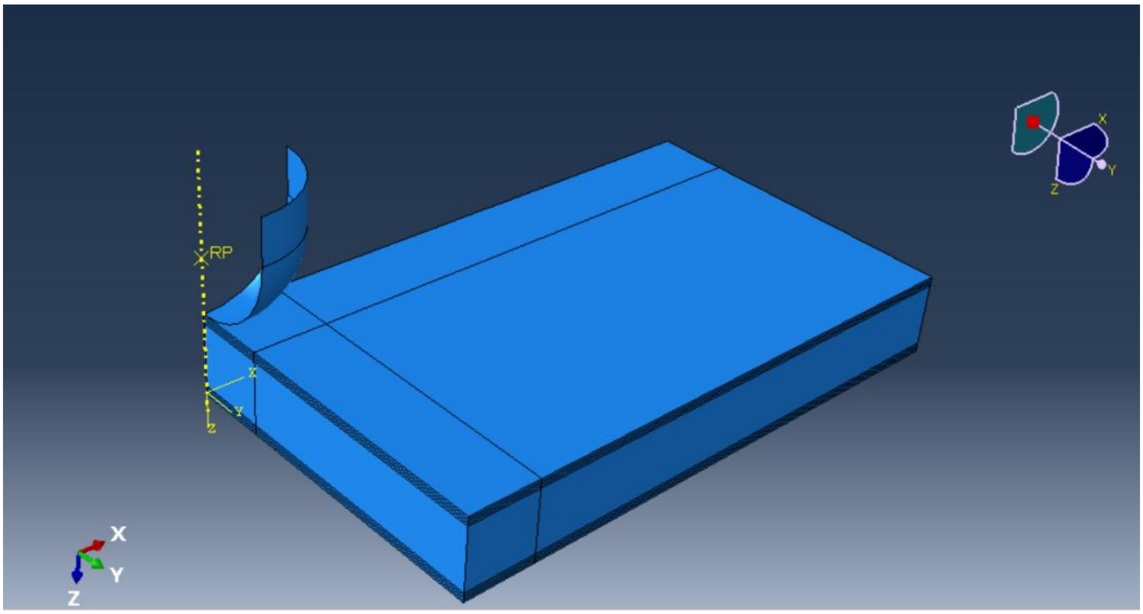

Figure 5.8: Final Assembly Abaqus model set-up before impact

Figures 5.7 and 5.8 show the interfaces and model set-up respectively prior to impact.

In this study, a PVC foam with a density of 80 kg/m^3 was modelled using the Crushable Foam Plasticity Model in ABAQUS/Explicit, employing the C3D8R element, which is an eight-node linear brick element with reduced integration. The crushable foam plasticity model allows for the foam to deform in compression due to cell wall buckling during the impact. The phenomenological constitutive volumetric hardening model was adopted that acknowledges that the cell buckling is not instantaneously recoverable and, therefore, can be idealised as plastic during the impact event. By referencing Yao et al. (2022), a compressive yield stress ratio of roughly 1.5 was adopted. Concurrently, a hydrostatic yield stress ratio (often referred to as "k_t") of 0.2 was utilised following the findings of Carranza et al. (2019) and Deshpande and Fleck (2001). Thus, the respective values of 1.5 for the compressive yield stress ratio and 0.2 for the hydrostatic yield stress ratio were used in this work. The compressive yield stress for the foam used was 1.31 MPa, adopted from the work of Xiao et al. (2024).This study considered both ductile and shear damage of the PVC foam during the impact event, which, to the author's best knowledge, was not covered in many studies.

Surface Interactions

Table 5.5: Contact Property Assignments

First Surface or Material	Second Surface or Material	Property Assigned
Impactor-Surface	comp-0-1. Top Surface	General Contact
comp-0-1. Bottom Surface	comp-90-1. Top Surface	General Contact
comp-90-1. Bottom Surface	comp-plus 45-1. Top Surface	General Contact
comp-plus 45-1. Bottom Surface	comp-minus 45-1. Top Surface	General Contact
comp-minus 45-1. Bottom Surface	Foam-1. Top Surface	General Contact
Foam-1. Bottom Surface	comp-minus 45-2. Top Surface	General Contact
comp-minus 45-2. Bottom Surface	comp-plus 45-2. Top Surface	General Contact
comp-plus 45-2. Bottom Surface	comp-90-2. Top Surface	General Contact
comp-90-2. Bottom Surface	comp-0-2. Top Surface	General Contact

The full representation of interactions included the impactor interaction with each ply and foam during the impact event as provided in Table 5.5. The tangential behaviour with a “penalty” option between the impactor and top surface was implemented with a coefficient of friction of 0.3, while the normal behaviour between the same was implemented with a “hard” contact option. Thus, a general contact algorithm was applied to calculate the common interactions in Abaqus/Explicit. The prediction of delamination between the laminates and between the skins and core occurrence was simulated using cohesive contact

Boundary Conditions

The impactor was allowed to move or translate in only one direction (z-direction) during impact with a predetermined lowest velocity of 0.1 m/s. Since modelling is limited to a quarter model, the x and y symmetries are allowed, while the edges on which the specimen rests on the slotted portion of the actual holding clamp are modelled as pinned edges to allow for movements in other directions.

Meshing

The impactor was modelled using R3D4 element type while both the laminates and the foam were modelled using C3D8R element type. Table 5.6 provides details of each element type for the respective materials.

Table 5.6: Summary of materials and respective element types

Material	**Element Type**
Impactor	R3D4: A 4-node 3-D bilinear rigid quadrilateral
Composite laminate	C3D8R: An 8-node linear brick, reduced integration, hourglass control.
Foam	C3D8R: An 8-node linear brick with reduced integration

The element removal was activated to ensure that the damaged elements were removed from the analysis. This occurs when the damage variables for failure modes at all the material points reach 1. The removed elements offer no resistance to deformation, although they remain visible on the model. These removed elements can be suppressed from the model display. Figure 5.9 shows the meshed assembly model.

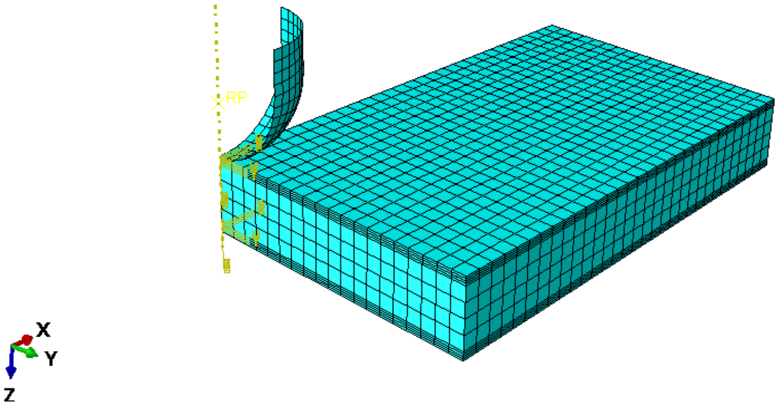

Figure 5.9: Meshed Assembly model

5.6 Results and Discussion

Models serve as simplified representations of reality and are based on specific assumptions. Consequently, validating these models using experimental data whenever feasible is essential. This highlights the importance of both modelling and experimentation in comprehending and forecasting system behaviour.

Damage initiation and propagation numerical models in this study were validated by micro-computed X-ray tomography. The impact response simulations were validated by drop weight experimental data by comparing inter-alia the force-time and energy-time curves.

Since the modelling was based on a quarter model, the kinetic energy values from the simulations were multiplied by four for comparison with the experimental values. For ease of analysis, references were typically made to the quarter model, except in instances where mentioning and referencing the full model was necessary.

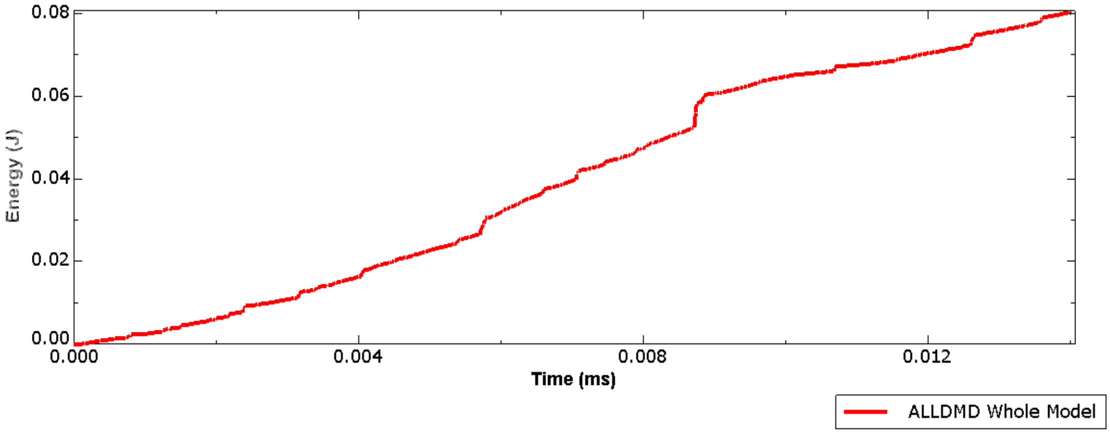

Figure 5.10: Damage dissipation energy profile for a velocity of 1 m/s

The significance of the damage dissipation energy profile provides insights into the initiation and progression of damage. The graph shows a more-less linear increase of dissipated energy for the first second before a non-linear increase for the duration of the impact event as shown in Figure 5.10. The non-uniformity of the curve may have been necessitated by the different sequence layups and introduction of various damage levels.

5.7 Validation and Analysis

This section deals with checking and proving the effectiveness of the selected models to predict the damage initiation and propagation. As previously described, the 3D Hashin failure criteria capture the states of the damage induced on the model as the impactor penetrates through the specimen. The damage induced can be described as intralaminar (across the laminates) and interlaminar (between laminates and the foam core). The interlaminar damage was modelled using the cohesive model to simulate delamination, which in the study was one of the dominant mechanisms in the failure of composites. The damage initiation was controlled by the quadratic nominal stress criterion. The onset of delamination can be identified whenever the quadratic function achieved unity (=1). The delamination initiation is illustrated in Figure 5.11 below. This delamination is considered as BVID and is located mainly around the impactor.

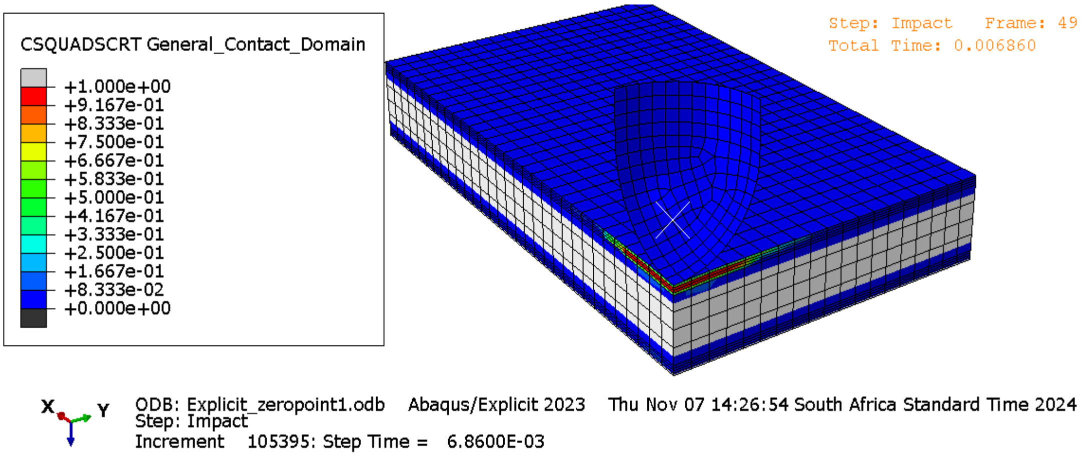

Figure 5.11: Delamination initiation at laminate interfaces

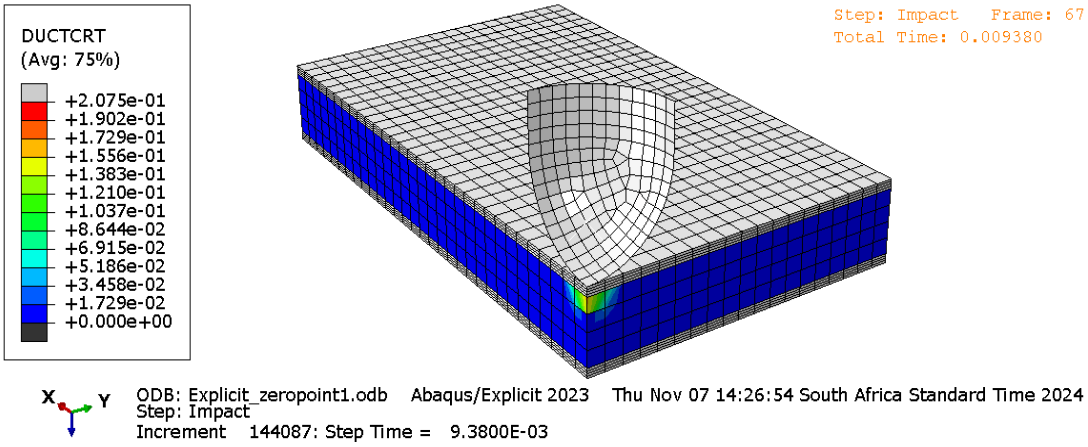

Figure 5.12: Foam core ductile damage during initial impact

As illustrated in Figures 5.12 and 5.13, the initial ductile and shear damage were localised around the impactor as predicted.

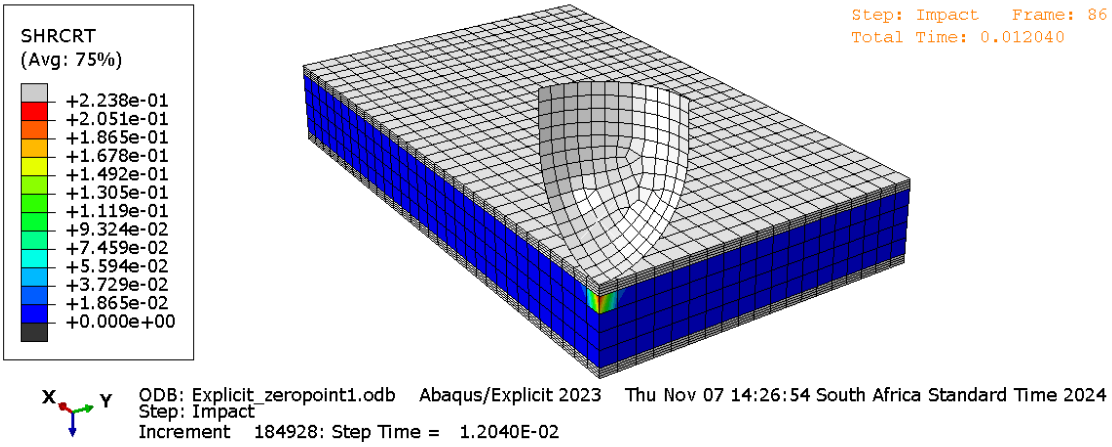

Figure 5.13: Foam core shear damage during initial impact

Notably, at this initial impact velocity, the SDV1, SDV2, SDV3 and SDV4 images show no damage inflicted on the fibre and matrix either in tension or compression. The respective images are provided in Appendix D. Figure 5.14 shows the implemented elements deletion during progressive damage.

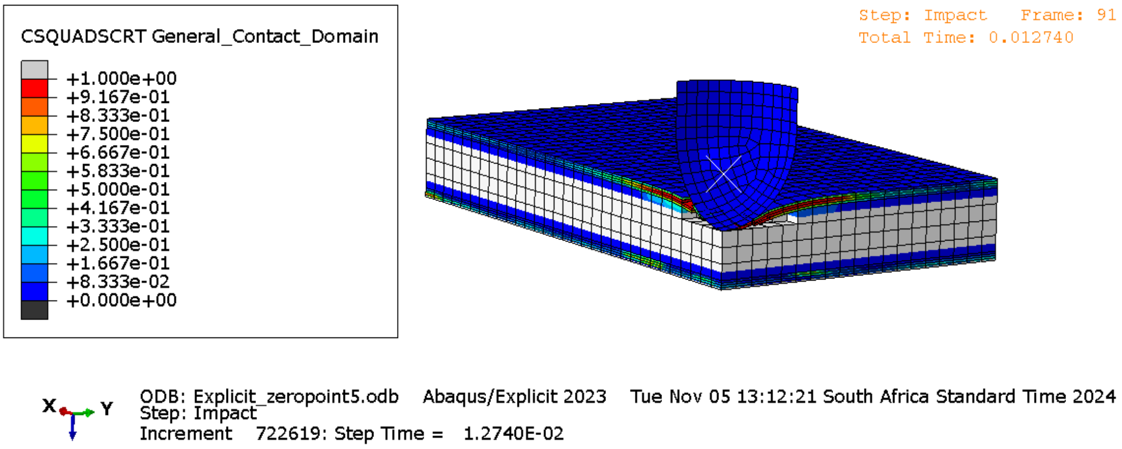

Figure 5.14: Progressive damage with implemented element deletion

In Figure 5.15, a stronger correlation between experimental and numerical data was observed at lower impact energy levels.

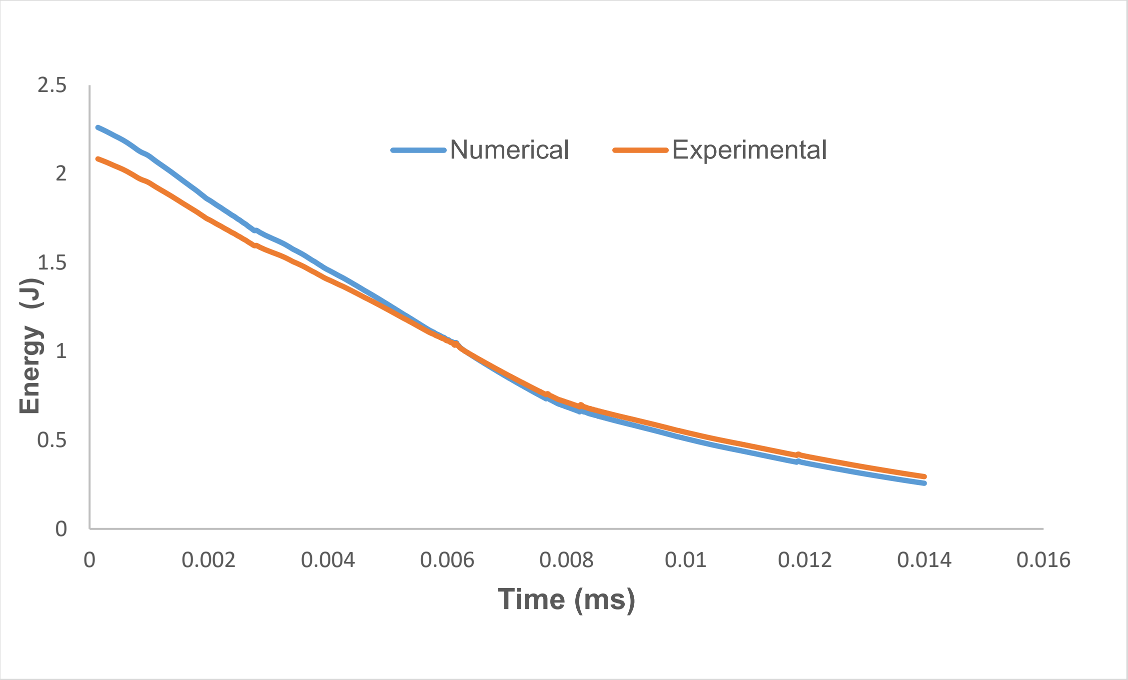

Figure 5.15: Comparison of experimental and numerical data for energy output

It was observed that lower velocities yielded more accurate validation results compared to higher velocities. Additionally, higher velocities lead to increased computational time and cost. In this study, the force-time curves were plotted for various velocities, as shown in Figures 5.16 and 5.17. The trends observed in the curves are consistent with those reported by (Deng et al., 2023), although their analysis focussed on a sandwich composite structure comprising CFRP skins and a Nomex aramid honeycomb core. Furthermore, at lower velocities where barely visible impact damages (BVID) are induced, the failure patterns exhibit three stages, namely: (a) linear proportionality of force and deflection, (b) non-uniform increase of force and deflection up to the peak and then a sudden drop in force, and (c) compression failure of the foam through densification.

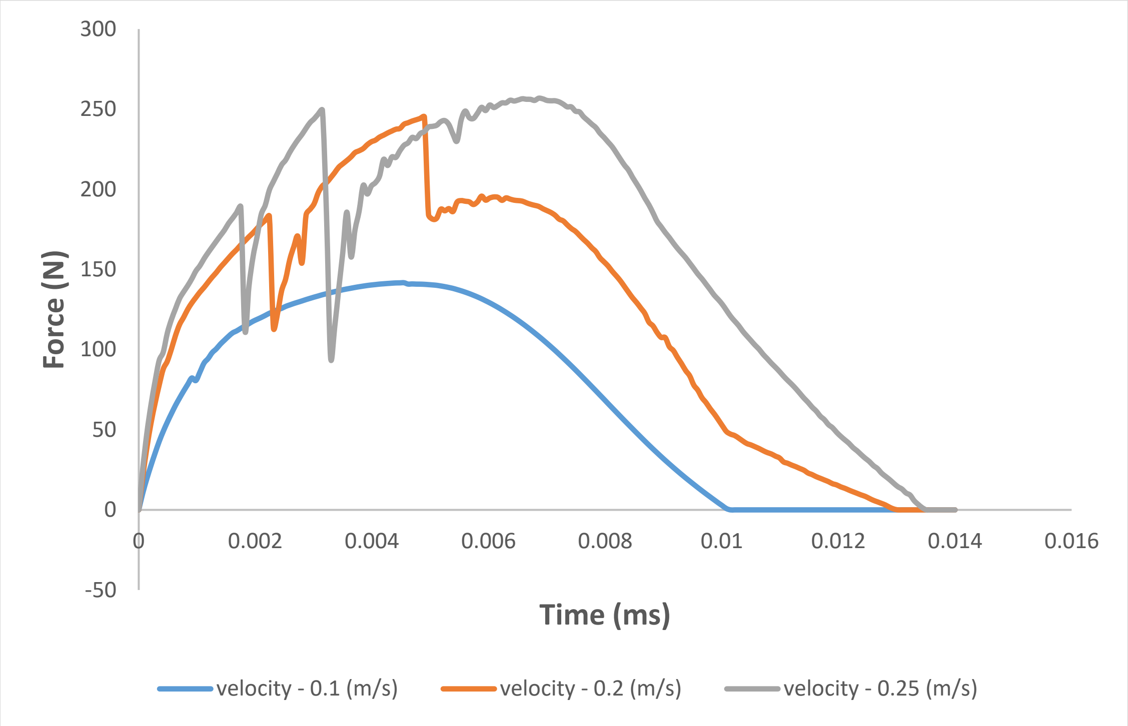

Figure 5.16: Force-time curves for different velocities

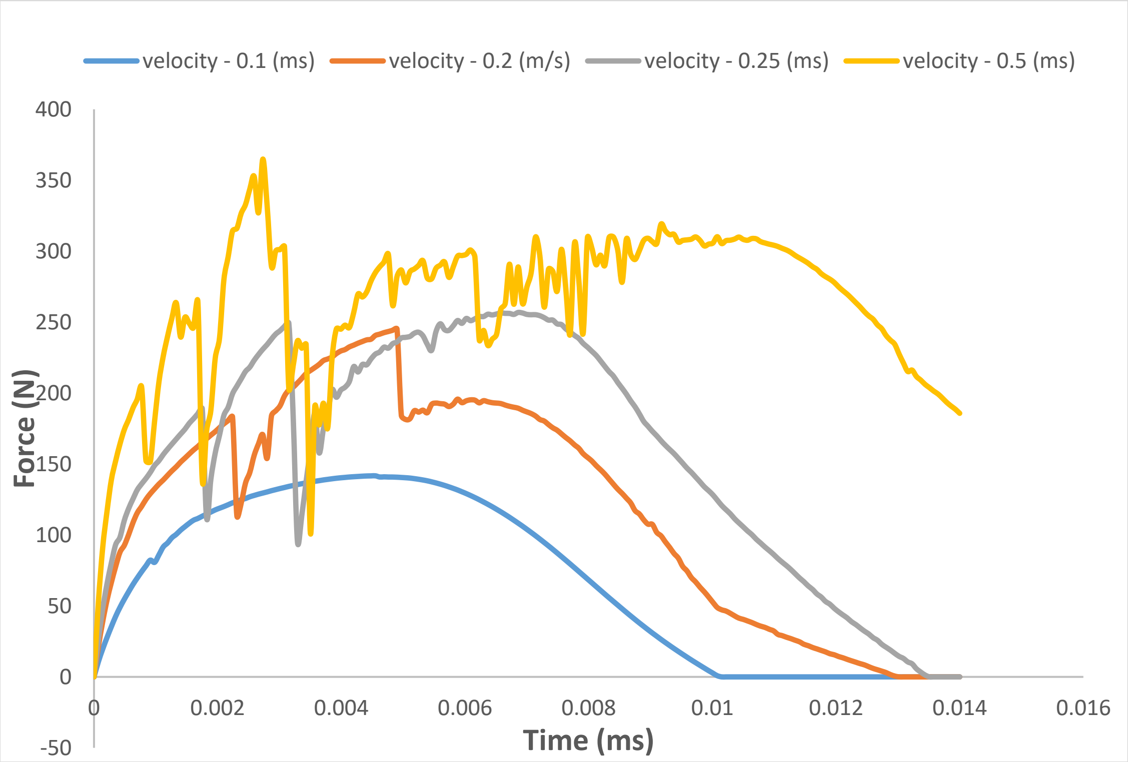

Figure 5.17: Force-time curves for different velocities

The impact response follows the same trend as the velocity is increased. The trend, however, gets distorted as the impactor nears full penetration of the specimen.

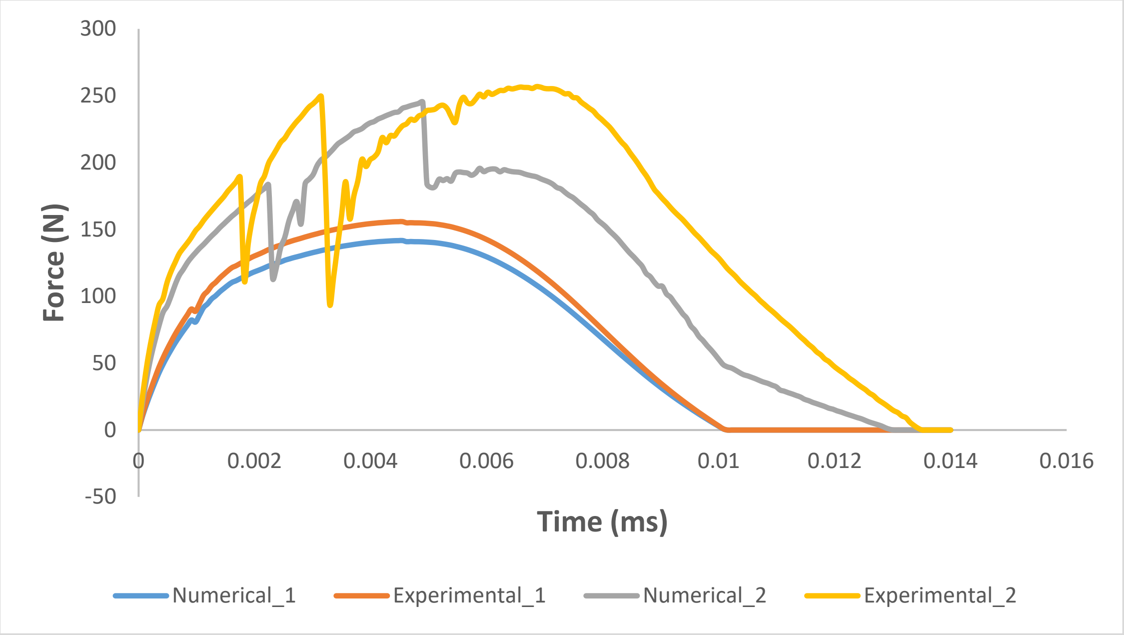

Figure 5.18: Comparison of numerical and experimental force-time curves for different velocities

The experimental data indicate larger forces compared to the numerical data as shown in Figure 5.18. Despite this, there is good agreement between the numerical and experimental data for the selected impact events. This similarity in tendencies suggests that the damage models effectively predict damage initiation and propagation.

A visual comparison between the simulation and experiment, as illustrated in Figures 19 and 20, revealed similarities in the identified damage mechanisms. Delamination was the initial damage mechanism, starting at the impacted zone and spreading along the specimen's length and width. Fibre breakages predominantly occurred in the impacted zone as the impactor penetrated the face sheets. The foam core exhibited characteristics of shearing and core densification.

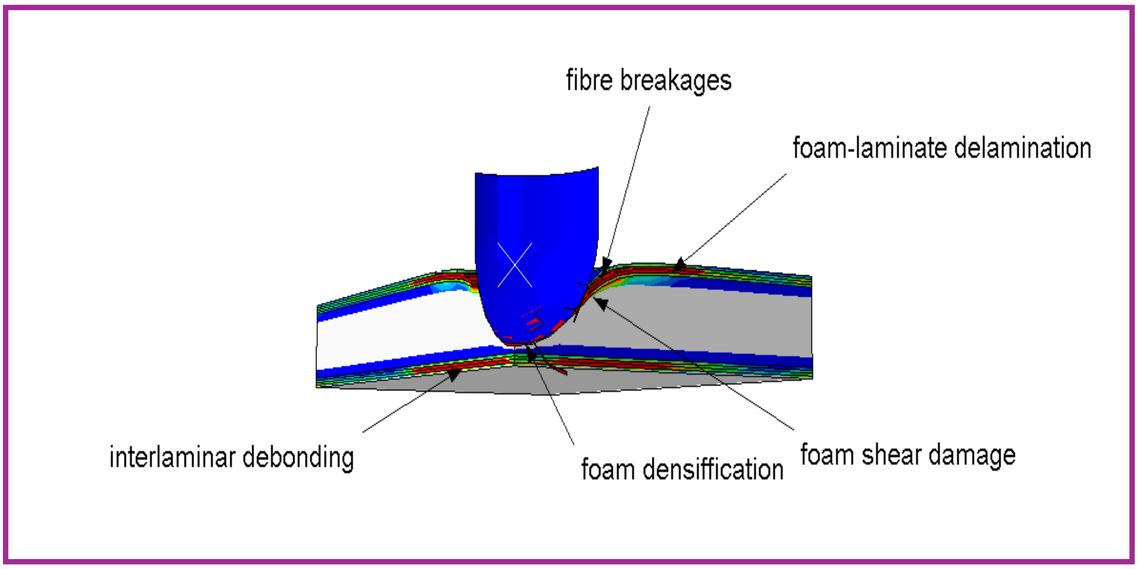

Figure 5.19: Damage Mechanisms - Simulation

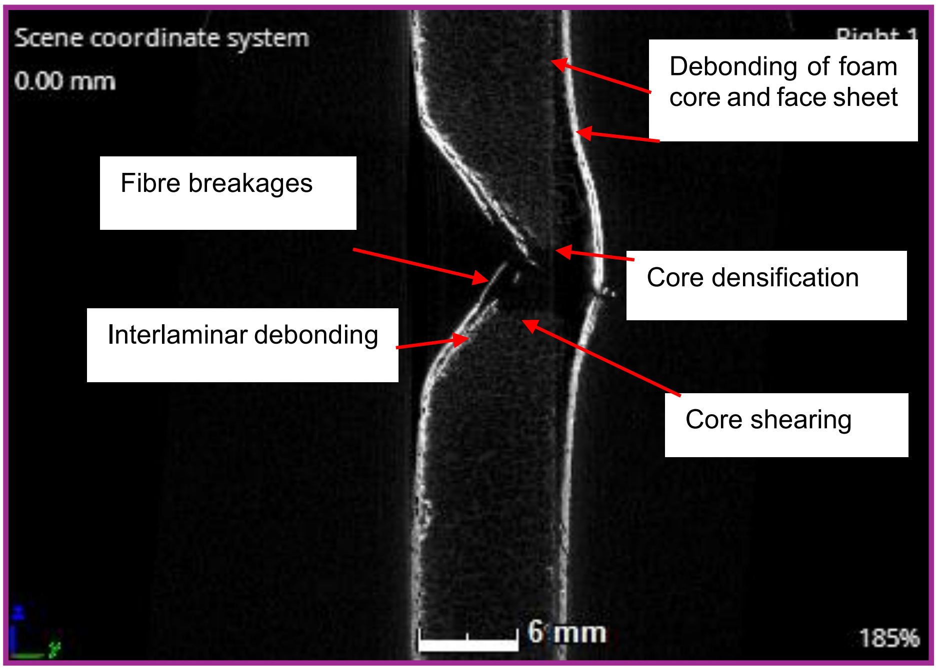

Figure 5.20: Damage Mechanisms - Experimental

For purposes of quantifying damage, the projected damage areas and depths of penetration were measured for the lowest impact velocities. This was done to determine the thresholds for BVIDs as specified in aerospace guidelines.

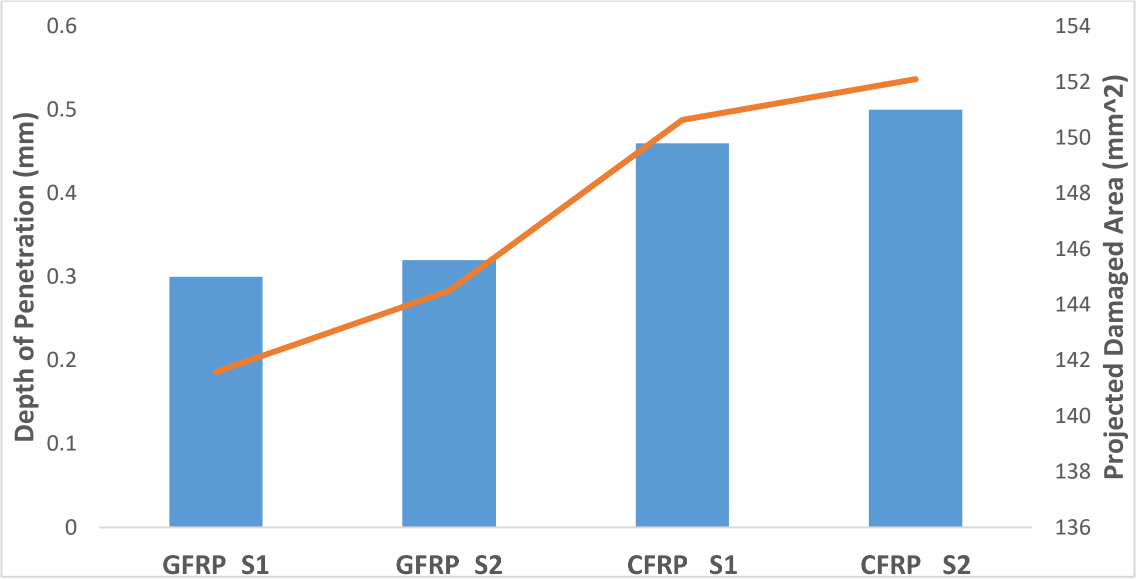

Figure 5.21: Comparison of specimen type versus Depth of Penetration and Projected Damaged Area for the same impact load

Figure 5.21 demonstrates that CFRP specimens are more susceptible to impact damage than GFRP specimens when subjected to the same load, impactor type, and stacking sequence. This observation was confirmed by the visually assessed levels of damage in the respective specimens. The comparison followed the standardised Barely Visible Impact Damage (BVID) threshold within 1 mm, as specified in aerospace standards (Easa, 2022). The corresponding impact energies are 2 J and 3 J for specimens 1 and 2, respectively. The volume of damage increases with depth of indentation, as illustrated in Figure 5.22.

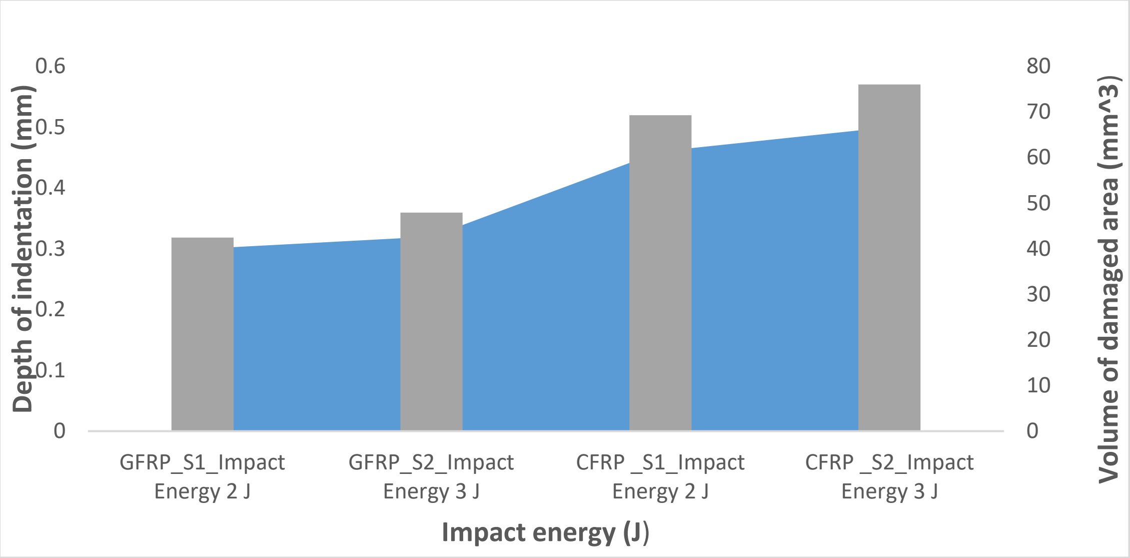

Figure 5.22: Correlation between depth of indentation and volume of damaged area for GFRP and CFRP panels

5.7.1 Validation of CT Images

Micro-Computed Tomography (Micro-CT) measurements have inherent uncertainties; thus, the reconstructed images require validation. Before capturing images with the CT system, a calibration process and imaging experimental set-ups were conducted. Emphasis was placed on correctly positioning the specimen and optimising its distance from the X-ray source and the detector. Determining the system's resolution was crucial, with the detector resolution ranging from 75-200 µm and a focal spot size of 7 µm being employed. It was established that the system's resolution is more significantly influenced by the detector resolution than by the focal spot size or any other parameter. Figure 5.23 shows the system resolution versus geometrical magnification.

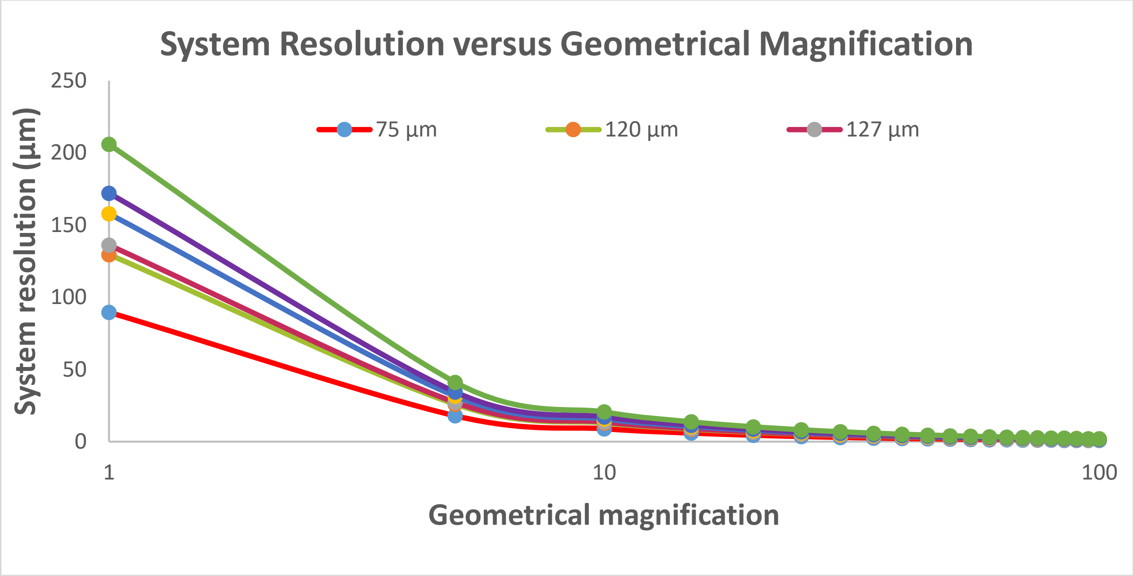

Figure 5.23: System resolution versus Geometrical magnification for spot size of 7 µm

This work determined the micro-CT resolution system and estimated it to be between 11-26 µm for a spot size of 7 µm and geometrical magnification of 8.

5.7.1.1 Use of ImageJ Software for validating the quality of reconstructed images

ImageJ 2.9.0/1.54h software was used to validate the quality of the reconstructed images. The use of ImageJ to validate the quality of reconstructed CT images is crucial. While many studies have traditionally accepted CT images at face value, evidence suggests that uncertainty errors can occur in CT measurements if proper precautions are not implemented beforehand. ImageJ helps address these uncertainties by allowing for a detailed analysis and validation of the images, ensuring their accuracy and reliability. The software offers a range of filters and processing options to enhance image quality, reduce noise, and improve contrast, which aids in the clearer visualisation of features within the CT images. This allows for comparison of multiple images or datasets to assess consistency and accuracy. An iterative process was employed, removing outliers and applying various filters to find the ones that offered the best improvements.

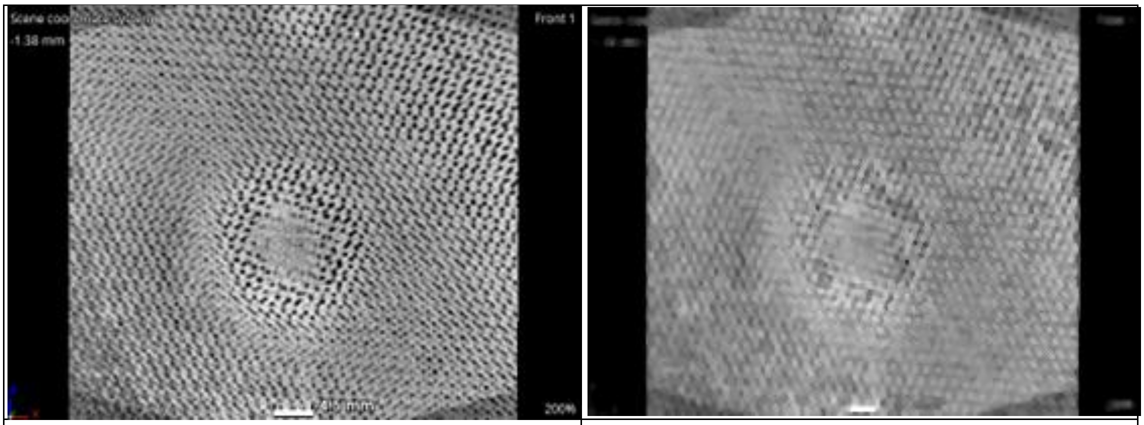

Unprocessed 2 J image

Processed 2 J image

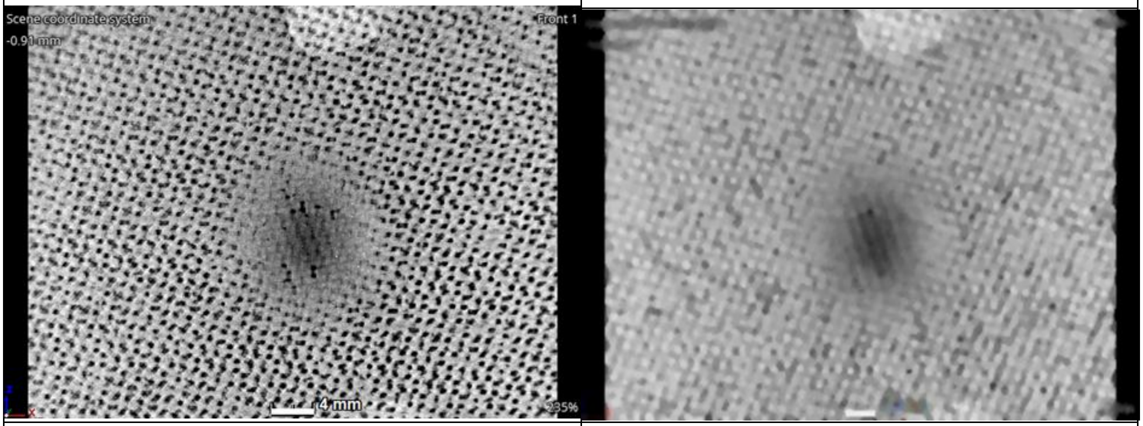

Unprocessed 3 J image

Processed 3 J image

Figure 5.24: Comparison of raw (unprocessed) and processed images

It was concluded that the median filter produced images that resembled the original ones. Interestingly, by visual means, the median filter was found to deliver images that closely resembled the original ones, albeit with a slight reduction in quality (Chipanga et al., 2024). This outcome supports the quality and accuracy of the images produced by the X-ray μ-CT. The images revealed both internal and external features with precision, demonstrating the effectiveness of the adjustments made to the X-ray μ-CT system. Figure 5.24 shows the comparison of reconstructed (raw) and processed images for 2 J and 3 J impact energies.

5.8 Concluding Remarks

The modelling of drop weight impact testing events was thoroughly detailed. The simulation was conducted using the Abaqus explicit solver, which was implemented with a user-defined subroutine. This subroutine was executed by linking Abaqus CAE software with the Intel Fortran Compiler. The damage model utilised the 3D Hashin Failure Criteria to capture damage initiation and propagation in both the fibre and matrix, with different failure modes being represented and evaluated independently. The interaction between laminates and the foam core was modelled using the cohesive zone method, enabled through a general contact algorithm. Boundary conditions mimicked the actual clamping system as specified in ASTM D7136/7136M-15, using a quarter model approach. The results and subsequent discussion confirm the successful application of the 3D Hashin Failure Criteria in capturing failure modes in sandwich composite structures, showing good agreement between experimental and numerical data. Additionally, the quality of reconstructed images was validated using ImageJ software.

CHAPTER 6
CONCLUSIONS AND RECOMMENDATIONS

6.1 Conclusions

This study aimed to investigate the phenomenon of impact damage and evaluate its effects on sandwich composite panels. As previously discussed, characterising impact damage involves assessing both the extent and nature of damage resulting from an impact event. Notably, the manufacturing characteristics of the structure played a critical role in influencing the specimens' response to impact and the subsequent damage assessment.

Sandwich panels were fabricated using autoclave processing, consisting of Glass Fiber Reinforced Polymer (GFRP) and Carbon Fiber Reinforced Polymer (CFRP) skins with Polyvinyl Chloride (PVC) foam cores. Specimens for mechanical testing were precisely sectioned using waterjet cutting technology, ensuring dimensional accuracy and minimal edge damage, essential for reliable material characterisation, particularly regarding mechanical properties. The experimental programme included three-point flexural testing and low-velocity drop-weight impact testing, which provided insights into both quasi-static and dynamic responses of the impacted specimens.

Visual inspections identified surface anomalies such as cracks, dents, and delaminations. To assess internal damage, X-ray micro-computed tomography (μCT) was employed. This non-destructive technique effectively detected barely visible impact damage (BVID) and revealed subsurface damage mechanisms across the full cross-sectional profile of the sandwich specimens, including the type, location, and extent of defects.

Damage severity was quantified by measuring the energy absorbed during impact, serving as an indicator of structural compromise. The volume of the damaged region was determined by calculating the projected area relative to the depth of indentation or penetration. At lower impact energy levels, the top skin exhibited localised indentation without visual delamination at the impact site due to the contact between the impactor and the top skin. However, delamination was observed in regions distal to the impact zone, supporting literature that suggests low-velocity impacts can induce global deformation patterns that undermine structural integrity.

The GFRP and CFRP skins experienced matrix micro-cracking due to tensile stresses, followed by fibre fracture as impact energy increased, leading to reduced load-bearing capacity. Delamination occurred both within interlaminar regions and at the skin–core interface. As impact energy increased, the PVC foam core exhibited progressive damage, including shear failure and cellular densification. The bottom skin showed morphological changes dependent on impact energy, ranging from minor surface deformation to near-perforation. These damage mechanisms were further validated through numerical modelling. Drop-weight impact events were simulated using the Abaqus explicit solver, with a user-defined subroutine facilitating implementation. The damage model employed the 3D Hashin failure criteria to capture damage initiation and propagation, revealing distinct failure modes in both the laminates and foam. The foam was modelled using the Crushable Plasticity model, which accounted for ductile and shear damage behaviours. The resulting damage included shear failure, cellular densification, and delamination at the laminate–foam interfaces.

ImageJ 2.9.0/1.54 h software was utilised to analyse the grayscale values around the impacted zone and to enhance image quality. A consistent decrease in grayscale values was observed with increasing depth of penetration at the impact site. This trend may offer valuable insights into the relationship between impactor characteristics and penetration depth during impact events, a finding that warrants further investigation to establish definitive conclusions.

Additionally, ImageJ was employed to improve the quality of the reconstructed images. An iterative filtering approach was adopted to remove outliers and identify filters that yielded the most significant enhancements. Among the filters applied, the median filter produced images that closely resembled the originals, albeit with a slight reduction in quality. This outcome reinforces the high quality and precision of the images generated by X-ray micro-computed tomography (μCT).

The conclusions drawn are highlighted below:

1. Low velocity can cause barely visible impact damage (BVID) in sandwich composite structures. Delamination was identified as the major failure mode of BVID. From the data analysed, both experimental and numerical, evidence was provided for the initiation and propagation of delamination. It was confirmed that the characterisation of BVID of delamination for the associated depths of indentation or penetration falls within the prescriptions as provided by the aeronautical maintenance guidelines (Easa, 2022).

2. The determination of BVID energy threshold levels is not based on a specific value of impact level but on the severity of damage inflicted on a given structure. Therefore, this determination should be done on a case-by-case basis.
3. It was found that within the realm of BVID, the size of the impacted zone was larger than the cross-sectional area of the impactor. The localised intra-laminar delamination may have caused this during the impact event.
4. Damage severity increases with increase in impact energy.
5. Damage morphology was influenced by the geometry of the impactor and the stacking sequence of the sandwich composite structure.
6. Not all non-destructive techniques are able to fully characterise the impact damages on sandwich composite structures. An attempt was made to use infrared thermography to detect impact damage with limited success, especially through the foam. However, X-ray micro-CT with an estimated resolution of up to 26 µm could detect not only the damage morphologies but also damage mechanisms.
7. Damage initiation was predicted by a sudden drop of force on the force-time curve. The decreased force results in reduced strength and stiffness of the composite sandwich structure. This diminishes the capacity of the structure to carry in-service loads, hence the need for structural health monitoring systems.
8. It was observed from the numerical data that damage accumulation increased exponentially in the last stage before failure. However, this observation could not be experimentally confirmed in the absence of a specialised camera to capture the impact event.
9. Numerical modelling using the 3D Hashin Criteria was able to predict the initiation and propagation of damage. This was implemented through a user-defined material subroutine incorporating ductile and shear damage of the PVC foam core. There is good agreement between numerical and experimental results.
10. Validation of numerical modelling with experimental work covered aspects such as mechanical responses exhibited on force-time, energy-time, and displacement-time curves, just to mention a few.
11. Validation of the reconstructed micro-CT images was accomplished by using ImageJ software through comparison with processed images.

6.2 Recommendations

1. As was already mentioned in the previous work by Chipanga et al. (2024), there is a need to further improve micro-CT resolution and sensitivity, especially for analysing small objects, by developing novel X-ray sources, detectors, algorithms and image reconstruction techniques.
2. Coupling micro-CT systems with mechanical testing rigs could allow observations to be made during testing and simultaneously offer insights into material properties and failure mechanisms.

6.3 Future Work

1. Carry out Compression After Impact (CAI) tests to measure the residual compressive strength of the composite structures. This measurement is crucial for estimating the remaining service life of the impacted coupons. CAI testing also provides insight into the residual strength of coupons affected by Barely Visibly Impact Damage (BVID).
2. Conduct Bending After Impact (BAI) tests to evaluate the residual flexural strength after impact. The measurements are compared against values obtained from pristine, undamaged samples.
3. Investigate the influence of fatigue on the performance of the panels to perhaps come up with more accurate models for predicting their respective fatigue lives.
4. Development of hybrid techniques through combining micro-CT with other non-destructive testing methods, such as ultrasonics, acoustic emission, or thermography, to provide complementary data for comprehensive analyses.
5. Develop techniques to couple micro-CT systems with mechanical test rigs to allow in-situ observations of material behaviour and evolution of damage mechanisms.
6. Integrate machine learning algorithms with computational models to improve predictive capabilities and reduce computational costs.

REFERENCES

Ahmed, A., & Wei, L. 2015. The Low-Velocity Impact Damage Resistance of the Composite Structures - a Review. *Rev. Adv. Mater. Sci,* 40, 127–145.

Akatay, A., Bora, M. Ö., Fidan, S., & Çoban, O. 2018. Damage characterization of three-point bended honeycomb sandwich structures under different temperatures with cone beam computed tomography technique. *Polymer Composites*, 39(1), 46–54. https://doi.org/10.1002/pc.23900

Almond, D. P., Angioni, S. L., & Pickering, S. G. 2017. Long pulse excitation thermographic non-destructive evaluation. *NDT and E International*, 87, 7–14. https://doi.org/10.1016/j.ndteint.2017.01.003

Anderson, T., & Madenci, E. 2000. Experimental investigation of low-velocity impact characteristics of sandwich composites. *Composite Structures*, 50(3), 239–247. https://doi.org/10.1016/S0263-8223(00)00098-2

Ashby, M. F., & Ashby, M. F. 2011. Case Studies: Hybrids. *Materials Selection in Mechanical Design*, 341–366. https://doi.org/10.1016/B978-1-85617-663-7.00012-6

Avilés, F., Couoh-Solis, F., Carlsson, L. A., Hernández-Pérez, A., & May-Pat, A. 2011. Experimental determination of torsion and shear properties of sandwich panels and laminated composites by the plate twist test. *Composite Structures*, 93(7), 1923-1928. https://doi.org/10.1016/j.compstruct.2011.02.001

Birman, V., & Kardomateas, G. A. 2018. Review of current trends in research and applications of sandwich structures. *Composites Part B: Engineering*, 142, 221–240. https://doi.org/10.1016/j.compositesb.2018.01.027

Carranza, I., Crocombe, A. D., Mohagheghian, I., Smith, P. A., Sordon, A., Meeks, G., & Santoni, C. 2019. Characterising and modelling the mechanical behaviour of polymeric foams under complex loading. *Journal of Materials Science*, 54(16), 11328–11344. https://doi.org/10.1007/s10853-019-03673-8

Chai, G. B., & Zhu, S. 2011. A review of low-velocity impact on sandwich structures. Proceedings of the Institution of Mechanical Engineers, Part L: *Journal of Materials: Design and Applications,* 225(4), 207-230. https://doi.org/10.1177/1464420711409985

Chen, D. H. 2011. Bending deformation of honeycomb consisting of regular hexagonal cells. *Composite Structures*, 93(2), 736–746. https://doi.org/10.1016/j.compstruct.2010.08.006

Chen, Y., Hou, S., Fu, K., Han, X., & Ye, L. (2017). Low-velocity impact response of composite sandwich structures: Modelling and experiment [Article]. *Composite Structures*, *168*, 322–334. https://doi.org/10.1016/j.compstruct.2017.02.064

Chipanga, T. 2009. Determination of the accuracy of non-destructive residual stress measurement methods. https://api.semanticscholar.org/CorpusID:135925999

Chipanga, T., Nemraoui, O., & Ismail, F. 2024. Damage Assessment of Low-Velocity Impacted Sandwich Composite Structures Using X-Ray Micro-Computed Tomography. *Journal of Engineering*, 2024, 1–13. https://doi.org/10.1155/2024/6147948

Chrysafi, A. P., Athanasopoulos, N., & Siakavellas, N. J. 2017. Damage detection on composite materials with active thermography and digital image processing. *International Journal of Thermal Sciences*, 116, 242–253. https://doi.org/10.1016/j.ijthermalsci.2017.02.017

Chung, S., Ley, O., Godinez, V., & Bandos, B. 2011. Line scanning thermography for rapid nondestructive inspection of large-scale composites. *AIP Conference Proceedings*, 1335, 1029-1036. https://doi.org/10.1063/1.3592050

Ciampa, F., Mahmoodi, P., Pinto, F., & Meo, M. 2018. Recent advances in active infrared thermography for non-destructive testing of aerospace components. In *Sensors* 18(2), 609. https://doi.org/10.3390/s18020609

Cnudde, V., & Boone, M. N. 2013. High-resolution X-ray computed tomography in geosciences: A review of the current technology and applications. *Earth-Science Reviews*, 123, 1–17. https://doi.org/10.1016/j.earscirev.2013.04.003

Constantin, N., Sandu, M., Sandu, A., & Găvan, M. (2017). Damage Identification and Mechanical Assessment of Impacted Sandwich Composites. *Procedia Engineering*, *188*, 178–185. https://doi.org/10.1016/j.proeng.2017.04.472

Cucinotta, F., Guglielmino, E., Risitano, G., & Sfravara, F. (2016). Assessment of Damage Evolution in Sandwich Composite Material Subjected to Repeated Impacts by Means Optical Measurements. *Procedia Structural Integrity*, *2*, 3660–3667. https://doi.org/10.1016/j.prostr.2016.06.455

Dattoma, V., Marcuccio, R., Pappalettere, C., & Smith, G. M. 2001. Thermographic investigation of sandwich structure made of composite material. *NDT and E International*, 34(8), 515-520. https://doi.org/10.1016/S0963-8695(00)00082-7

Dear, J. P., Lee, H., & Brown, S. A. 2006. Impact damage processes in composite sheet and sandwich honeycomb materials. International *Journal of Impact Engineering*, 32(1–4), 130–154. https://doi.org/10.1016/j.ijimpeng.2005.02.005

Deng, J., Gong, X., Xue, P., Yin, Q., & Wang, X. (2023). A comprehensive analysis of damage behaviors of composite sandwich structures under localized impact. *Mechanics of Advanced Materials and Structures*, *30*(16), 3231–3244. https://doi.org/10.1080/15376494.2022.2070937

Deshpande, V. S., & Fleck, N. A. 2001. Multi-axial yield behaviour of polymer foams. In *Acta mater,* 49(10), 1859-1866. www.elsevier.com/locate/actamat

Devivier, C., Pierron, F., & Wisnom, M. R. 2012. Damage detection in composite materials using deflectometry, a full-field slope measurement technique. Composites Part A: *Applied Science and Manufacturing*, 43(10), 1650–1666. https://doi.org/10.1016/j.compositesa.2011.11.009

Diamanti, K., & Soutis, C. 2010. Structural health monitoring techniques for aircraft composite structures. *Progress in Aerospace Sciences*, 46(8), 342-352. https://doi.org/10.1016/j.paerosci.2010.05.001

du Plessis, A., Broeckhoven, C., Guelpa, A., & le Roux, S. G. 2017. Laboratory x-ray micro-computed tomography: A user guideline for biological samples. In *GigaScience,* 6(6), 1-11. Oxford University Press. https://doi.org/10.1093/gigascience/gix027

Duchene, P., Chaki, S., Ayadi, A., & Krawczak, P. 2018. A review of non-destructive techniques used for mechanical damage assessment in polymer composites. In *Journal of Materials Science,* 53(11), 7915–7938. https://doi.org/10.1007/s10853-018-2045-6

Easa. 2022. *Easy Access Rules for Acceptable Means of Compliance for Airworthiness of Products, Parts and Appliances* (AMC-20) (Amendment 23) (PDF). http://eur-lex.europa.eu/

Ehrhart, B., Valeske, B., & Bockenheimer, C. 2013. *Non-destructive evaluation (NDE) of aerospace composites: Methods for testing adhesively bonded composites*. In *Non-Destructive Evaluation (NDE) of Polymer Matrix Composites: Techniques and Applications* (pp. 220–237). https://doi.org/10.1533/9780857093554.2.220

Farooq, U., & Gregory, K. 2009. Finite element simulation of low velocity impact damage morphology in quasi-isotropic composite panels under variable shape impactors. *European Journal of Scientific Research*, *25*(4), 636-648.

Foo, C. C., Chai, G. B., & Seah, L. K. 2008. A model to predict low-velocity impact response and damage in sandwich composites. *Composites Science and Technology*, 68(6), 1348–1356. https://doi.org/10.1016/j.compscitech.2007.12.007

Freeman, B., Schwingler, E., Mahinfalah, M., & Kellogg, K. 2005. The effect of low-velocity impact on the fatigue life of Sandwich composites. *Composite Structures*, 70(3), 374–381. https://doi.org/10.1016/j.compstruct.2004.09.027

Funari, M. F., Spadea, S., Lonetti, P., & Lourenço, P. B. 2021. On the elastic and mixed-mode fracture properties of PVC foam. *Theoretical and Applied Fracture Mechanics*, 112(4), 102924. https://doi.org/10.1016/j.tafmec.2021.102924

Gdoutos, E. E., & Daniel, I. M. 2004. Failure mechanisms of composite sandwich structures. *Engineering*, 16(4), 345–364. http://jtc.sagepub.com/cgi/doi/10.1177/0892705703016004005

Gryzagoridis, B. J., Findeis, D., & Chipanga, T. 2011. Shearography - in identifying the presence and subsequent measurement of residual stresses. *Insight - Non-Destructive Testing and Condition Monitoring*, 53(5), 245–247. https://doi.org/10.1784/insi.2011.53.5.245

Gryzagoridis, J., Oliver, G., & Findeis, D. 2015. On the equivalent flexural rigidity of sandwich composite panels. *Insight: Non-Destructive Testing and Condition Monitoring,* 57(3), 140–143. https://doi.org/10.1784/insi.2014.57.3.140

Hashin, Z. 1980. Failure Criteria for Unidirectional Fiber Composites. ASME. *J. Appl. Mech*. June 1980; 47(2): 329–34.

Huang, S. J., Lin, H. L., & Liu, H. W. 2007. Electronic speckle pattern interferometry applied to the displacement measurement of sandwich plates with two "fully potted" inserts. *Composite Structures*, 79(2), 157-162. https://doi.org/10.1016/j.compstruct.2005.07.008

Hung, Y. Y., Chen, Y. S., Ng, S. P., Liu, L., Huang, Y. H., Luk, B. L., Ip, R. W. L., Wu, C. M. L., & Chung, P. S. 2009. Review and comparison of shearography and active thermography for non-destructive evaluation. *Materials Science and Engineering R: Reports*, 64(5–6), 73–112. https://doi.org/10.1016/j.mser.2008.11.001

Hung, Y. Y., Yang, L. X., & Huang, Y. H. 2013. Non-destructive evaluation (NDE) of composites: Digital shearography. In *Non-Destructive Evaluation (NDE) of Polymer Matrix Composites: Techniques and Applications* (pp. 84–115). https://doi.org/10.1533/9780857093554.1.84

Ibrahim, I. D., Jamiru, T., Sadiku, R. E., Kupolati, W. K., Agwuncha, S. C., & Ekundayo, G. 2015. The use of polypropylene in bamboo fibre composites and their mechanical properties - A review. *Journal of Reinforced Plastics and Composites*, 34(16), 1347–1356. https://doi.org/10.1177/0731684415591302

Jang, B. W., & Kim, C. G. 2017. Real-time detection of low-velocity impact-induced delamination onset in composite laminates for efficient management of structural health. *Composites Part B: Engineering*, 123, 124–135. https://doi.org/10.1016/j.compositesb.2017.05.019

Katunin, A., Dragan, K., & Dziendzikowski, M. 2015. Damage identification in aircraft composite structures: A case study using various non-destructive testing techniques. *Composite Structures*, 127, 1–9. https://doi.org/10.1016/j.compstruct.2015.02.080

Koloor, S. S. R., Karimzadeh, A., Yidris, N., Petrů, M., Ayatollahi, M. R., & Tamin, M. N. 2020. An energy-based concept for yielding of multidirectional FRP composite structures using a mesoscale lamina damage model. Polymers, 12(1), 157. https://doi.org/10.3390/polym12010157

Krzyzak, A., Mazur, M., Gajewski, M., Drozd, K., Komorek, A., & Przybyłek, P. 2016. Sandwich Structured Composites for Aeronautics: Methods of Manufacturing Affecting Some Mechanical Properties. *International Journal of Aerospace Engineering,* Volume 2016. https://doi.org/10.1155/2016/7816912

Ley, O., & Godinez, V. 2013. Non-destructive evaluation (NDE) of aerospace composites: Application of infrared (IR) thermography. In *Non-Destructive Evaluation (NDE) of Polymer Matrix Composites: Techniques and Applications* (pp. 309–334). https://doi.org/10.1533/9780857093554.3.309

Li, D. H., Liu, Y., & Zhang, X. 2014. Low-velocity impact responses of the stiffened composite laminated plates based on the progressive failure model and the layerwise/solid-elements method. *Composite Structures*, 110(1), 249–275. https://doi.org/10.1016/j.compstruct.2013.12.011

Li, G., Fang, Y., Hao, P., & Li, Z. 2017. Three-point bending deflection and failure mechanism map of sandwich beams with second-order hierarchical corrugated truss core. *Journal of Sandwich Structures and Materials*, 19(1), 83–107. https://doi.org/10.1177/1099636215622052

Maierhofer, C., Myrach, P., Reischel, M., Steinfurth, H., Röllig, M., & Kunert, M. 2014. Characterizing damage in CFRP structures using flash thermography in reflection and transmission configurations. *Composites Part B: Engineering*, 57, 35–46. https://doi.org/10.1016/j.compositesb.2013.09.036

Mostafa, N. H., Ismarrubie, Z. N., Sapuan, S. M., & Sultan, M. T. H. 2017. Fibre prestressed polymer-matrix composites: A review. In *Journal of Composite Materials,* 51(1), 39–66). https://doi.org/10.1177/0021998316637906

Noury, P. M., Shenoi, R. A., & Sinclair, I. 1998. On mixed-mode fracture of PVC foam. In *International Journal of Fracture,* 92, 131–151. https://doi.org/10.1023/A:1007495223740

Olsson, R. 2000. Mass criterion for wave-controlled impact response of composite plates. *Composites Part A: Applied Science and Manufacturing*, 31(8), 879–887. https://doi.org/10.1016/S1359-835X(00)00020-8

Olsson, R. 2003. Closed form prediction of peak load and delamination onset under small mass impact. *Composite Structures,* 59(3), 341–349. https://doi.org/10.1016/S0263-8223(02)00244-1

Pathipaka, R. K., Namala, K. K., Sunkara, N., & Bandaru, C. R. (2020). Damage characterization of sandwich composites subjected to impact loading. *Journal of Sandwich Structures and Materials*, *22*(7), 2125–2138. https://doi.org/10.1177/1099636218792717

Phadnis, V. A., Roy, A., & Silberschmidt, V. V. 2016. Dynamic damage in FRPs: From low to high velocity. In *Dynamic Deformation, Damage and Fracture in Composite Materials and Structures* (pp. 1939–222). https://doi.org/http://dx.doi.org/10.1016/B978-0-08-100080-9.00008-7

Qiu, A., Fu, K., Lin, W., Zhao, C., & Tang, Y. 2014. Modelling low-speed drop-weight impact on composite laminates. *Materials and Design*, 60, 520–531. https://doi.org/10.1016/j.matdes.2014.04.041

Razali, N., Sultan, M. T. H., Mustapha, F., Yidris, N., & Ishak, M. R. 2014. Impact Damage on Composite Structures – A Review. *The International Journal of Engineering and Science,* 3(7), 8–20. www.theijes.com

Reifsnider K.L., Henneke E.G., Stinchcomb W.W. 1980. *The Mechanics of Vibrothermography*. Springer. https://doi.org/https://doi.org/10.1007/978-1-4684-3857-4_12

Richardson, M. O. W., & Wisheart, M. J. 1996. Review of low-velocity impact properties of composite materials. *Composites Part A: Applied Science and Manufacturing*, 27(12), 1123–1131. https://doi.org/10.1016/1359-835X(96)00074-7

Robinson, P., & Davies, G. A. O. 1992. Impactor mass and specimen geometry effects in low velocity impact of laminated composites. *International Journal of Impact Engineering*, 12(2), 189–207. https://doi.org/10.1016/0734-743X(92)90408-L

Rolland, H., Saintier, N., Wilson, P., Merzeau, J., & Robert, G. 2017. In situ X-ray tomography investigation on damage mechanisms in short glass fibre reinforced thermoplastics: Effects of fibre orientation and relative humidity. *Composites. Part B, Engineering,* 109, 170–186. https://doi.org/10.1016/j.compositesb.2016.10.043

Růžek, R., Lohonka, R., & Jironč, J. 2006. Ultrasonic C-scan and shearography NDI techniques evaluation of impact defects identification. *NDT and E International*, 39(2), 132–142. https://doi.org/10.1016/j.ndteint.2005.07.012

Saeid, A. A., & Donaldson, S. L. 2016. Experimental and finite element evaluations of debonding in composite sandwich structure with core thickness variations. *Advances in Mechanical Engineering*, 8(9), 1–18. https://doi.org/10.1177/1687814016667418

Safri, S. N. A., Sultan, M. T. H., Jawaid, M., & Jayakrishna, K. 2018. Impact behaviour of hybrid composites for structural applications: A review. *Composites Part B: Engineering,* 133, 112–121. https://doi.org/10.1016/j.compositesb.2017.09.008

Salvo, L., Cloetens, P., Maire, E., Zabler, S., Blandin, J. J., Buffi E Ere C, J. Y., Ludwig, W., Boller, E., Bellet, D., & Josserond, C. N.d. X-ray micro-tomography an attractive characterisation technique in materials science. www.elsevier.com/locate/nimb

Sánchez-Sáez, S., Barbero, E., & Navarro, C. 2008. Compressive residual strength at low temperatures of composite laminates subjected to low-velocity impacts. *Composite Structures,* 85(3), 226–232. https://doi.org/10.1016/j.compstruct.2007.10.026

Schoeman, L., Williams, P., du Plessis, A., & Manley, M. 2016. X-ray micro-computed tomography (μCT) for non-destructive characterisation of food microstructure. In *Trends in Food Science and Technology*, 47, 10–24. https://doi.org/10.1016/j.tifs.2015.10.016

Singhal, T., Kim, E., Kim, T. Y., & Yang, J. 2017. Weak bond detection in composites using highly nonlinear solitary waves. *Smart Materials and Structures*, 26(5), 055011. https://doi.org/10.1088/1361-665X/aa6823

Sjögren, A., Krasnikovs, A., & Varna, J. 2001. Experimental determination of elastic properties of impact damage in carbon fibre/epoxy laminates. Composites - Part A: *Applied Science and Manufacturing*, 32(9), 1237–1242. https://doi.org/10.1016/S1359-835X(01)00058-6

Tomblin, J., Lacy, T., Smith, B., Hooper, S., Vizzini, A., & Lee, S. 1999. Review of Damage Tolerance for Composite Sandwich Airframe Structures. *Bericht,* 71. https://doi.org/DOT/FAA/AR-99/49

Topac, O. T., Gozluklu, B., Gurses, E., & Coker, D. 2017. Experimental and computational study of the damage process in CFRP composite beams under low-velocity impact. *Composites Part A: Applied Science and Manufacturing*, 92, 167–182. https://doi.org/10.1016/j.compositesa.2016.06.023

Ude, A. U., Ariffin, A. K., & Azhari, C. H. (2013). Impact damage characteristics in reinforced woven natural silk/epoxy composite face-sheet and sandwich foam, coremat and honeycomb materials [Article]. *International Journal of Impact Engineering*, *58*, 31–38. https://doi.org/10.1016/j.ijimpeng.2013.03.003

Wicaksono, S., & Chai, G. B. 2013. A review of advances in fatigue and life prediction of fibre-reinforced composites. In Proceedings of the Institution of Mechanical Engineers, Part L: *Journal of Materials: Design and Applications*, 227(3), 179–195. https://doi.org/10.1177/1464420712458201

Xiao, W., Li, Y., Hu, Y., Song, Z., Cai, W., & Li, X. 2024. Analytical study on the dynamic mechanical behaviours of foam-core sandwich plate under repeated impacts. *Thin-Walled Structures*, 196, 111480. https://doi.org/10.1016/j.tws.2023.111480

Xie, H., Fang, H., Li, X., Wan, L., Wu, P., & Yu, Y. 2021. Low-velocity impact damage detection and characterization in composite sandwich panels using infrared thermography. *Composite Structures*, 269, 114008. https://doi.org/10.1016/j.compstruct.2021.114008

Xu, S., & Chen, P. H. 2013. Prediction of low velocity impact damage in carbon/epoxy laminates. *Procedia Engineering*, 67, 489–496. https://doi.org/10.1016/j.proeng.2013.12.049

Yamashita, M., & Gotoh, M. 2005. Impact behaviour of honeycomb structures with various cell specifications—numerical simulation and experiment. *International Journal of Impact Engineering,* 32(1), 618-630*.* https://doi.org/10.1016/j.ijimpeng.2004.09.001

Zenkert, D. 2009. Damage tolerance of naval sandwich panels. Major Accomplishments in Composite Materials and Sandwich Structures: *An Anthology of ONR Sponsored Research*, 279–303. https://doi.org/10.1007/978-90-481-3141-9_11

Zhang, X., Xu, F., Zang, Y., & Feng, W. (2020). Experimental and numerical investigation on damage behavior of honeycomb sandwich panel subjected to low-velocity impact. *Composite Structures*, *236*. https://doi.org/10.1016/j.compstruct.2020.111882

Zhou, G., Hill, M., Loughlan, J., & Hookham, N. 2006. Damage characteristics of composite honeycomb sandwich panels in bending under quasi-static loading. *Journal of Sandwich Structures and Materials,* 8(1), 55-90. https://doi.org/10.1177/1099636206056888

Zhu, F., Lu, G., Ruan, D., & Wang, Z. 2010. Plastic Deformation, Failure and Energy Absorption of Sandwich Structures with Metallic Cellular Cores. *International Journal of Protective Structures*, 1(4), 507–541. https://doi.org/10.1260/2041-4196.1.4.507

Zhu, S., & Chai, G. B. 2013. Damage and failure mode maps of composite sandwich panel subjected to quasi-static indentation and low velocity impact. *Composite Structures,* 101, 204–214. https://doi.org/10.1016/j.compstruct.2013.02.010

Zhu, Y., & Sun, Y. 2021. Low-velocity impact response of multilayer foam core sandwich panels with composite face sheets. *International Journal of Mechanical Sciences*, 209, 106704. https://doi.org/10.1016/j.ijmecsci.2021.106704

APPENDICES

Appendix A: MATLAB Plots Coding for Impact Tests_CFRP & GFRP

```
[D,F,D1,F1,D2,F2]=textread('Data_CFRP2.txt','%f %f %f %f %f %f','headerlines',1);
%l = length(setpoint)-1;
%N = 0:l;
%  t=t/40;

plot(D,F,'b-','linewidth',2)
 hold on
 %subplot (D1,F1)
  %plot (D1,F1)
  hold on
%plot(t,x9,'r-.','linewidth',2)
% % %
xlabel('Deflection[mm]')
 ylabel('Force [N]')
% title(' ')
% %
%plot(D1,F1,'r-','linewidth',2)
% hold of
%plot(D2,F2,'m-','linewidth',2)
%  legend('ACE1','AEC2');
%  h=legend;
%  set(h,'edgecolor','white');
%  box on
% grid on

% set(gca,'FontSize',LableFontsize,'LineWidth',AxisLineWidth)
% set(get(gca,'xlabel'),'fontsize',LableFontsize)
% set(get(gca,'ylabel'),'fontsize',LableFontsize)
% set(gcf,'Units',
'inches');set(gcf,'Position',[position,position,FigureWidth,FigureWidth*Proportion
])
```

```
function createfigure1(X1, Y1)
%CREATEFIGURE1(X1, Y1)
%  X1:  vector of plot x data
%  Y1:  vector of plot y data

% Create figure
figure('WindowState','maximized');

% Create axes
axes1 = axes;
hold(axes1,'on');

% Create plot
plot(X1,Y1,'LineWidth',2);

% Create ylabel
ylabel({'Energy (J)'});

% Create xlabel
```

```
xlabel({'Time (ms)'});

% Create title
title({'Energy v Time for CFRP 100'});

% Uncomment the following line to preserve the X-limits of the axes
% xlim(axes1,[-10.0806451612903 49.9193548387097]);
% Uncomment the following line to preserve the Y-limits of the axes
% ylim(axes1,[0 4]);
box(axes1,'on');
hold(axes1,'off');
% Set the remaining axes properties
set(axes1,'FontName','Arial','FontSize',11,'XGrid','on','YGrid','on');
```

```
function createfigure(X1, Y1)
%CREATEFIGURE(X1, Y1)
%  X1:  vector of plot x data
%  Y1:  vector of plot y data


% Create figure
figure('WindowState','maximized');

% Create axes
axes1 = axes;
hold(axes1,'on');

% Create plot
plot(X1,Y1,'LineWidth',2);

% Create ylabel
ylabel({'Load (N)'});

% Create xlabel
xlabel({'Time (ms)'});

% Create title
title({'Load v Time for GFRP 100'});

% Uncomment the following line to preserve the X-limits of the axes
% xlim(axes1,[-10 50]);
% Uncomment the following line to preserve the Y-limits of the axes
% ylim(axes1,[-100 700]);
box(axes1,'on');
hold(axes1,'off');
```

Flexure Test Plots

```
Flexuredata= xlsread('Flexure Tests_Data
Analysis2.xlsx','CFRP_Specimens','A2:J21022');

% Data scaling factors
%d=(0:0.5:35)
%=(0:5:600)

% Specimen 1
d1=Flexuredata ('A2:A21022');
f1=Flexuredata ('B2:B21022');

plot(d1,f1,'r','linewidth',2)
%axis([0 35 0 600]);
title('Force versus Deflection')
xlabel('Deflection (mm)')
ylabel('Force (N)')
hold on

% Specimen 2
d2=Flexuredata ('C2:C21022');
f2=Flexuredata ('D2:D21022');

plot(d2,f2,'b','linewidth',2)
%axis([0 35 0 600]);
hold on

% Specimen 3
d3=Flexuredata ('E2:E21022');
f3=Flexuredata ('F2:F21022');

plot(d3,f3,'m','linewidth',2)
%axis([0 35 0 600]);
hold on

% Specimen 4
d4=Flexuredata ('G2:G21022');
f4=Flexuredata ('H2:H21022');

plot(d4,f4,'k','linewidth',2)
%axis([0 35 0 600]);
hold on

% Specimen 5
d5=Flexuredata ('I2:I21022');
f5=Flexuredata ('J2:J21022');

plot(d5,f5,'g','linewidth',2)
%axis([0 35 0 600]);
hold off
```

Appendix B: Constitutive Laws for Modelling

Continuum Damage Model

Degraded Compliance Matrix, S_d :

$$S_d = \begin{bmatrix} \frac{1}{d_f E_{11}} & -\frac{v_{21}}{E_{22}} & -\frac{v_{31}}{E_{33}} & 0 & 0 & 0 \\ -\frac{v_{12}}{E_{11}} & \frac{1}{d_m E_{22}} & -\frac{v_{32}}{E_{33}} & 0 & 0 & 0 \\ -\frac{v_{13}}{E_{11}} & -\frac{v_{23}}{E_{22}} & \frac{1}{E_{33}} & 0 & 0 & 0 \\ 0 & 0 & 0 & \frac{1}{d_f d_m G_{12}} & 0 & 0 \\ 0 & 0 & 0 & 0 & \frac{1}{d_f d_m G_{23}} & 0 \\ 0 & 0 & 0 & 0 & 0 & \frac{1}{d_f d_m G_{31}} \end{bmatrix}$$

Degraded Stiffness Matrix, C_d :

$$\begin{aligned} C_d &= \frac{1}{\Delta} \\ &= \begin{bmatrix} d_f E_{11}(1 - d_m v_{23} v_{32}) & d_f d_m E_{11}(v_{12} + v_{32} v_{13}) & d_f E_{11}(v_{13} + d_m v_{12} v_{23}) & 0 & 0 & 0 \\ 0 & d_m E_{22}\big(1 - d_f v_{13} v_{31}\big) & d_m E_{22}\big(v_{23} + d_f v_{21} v_{13}\big) & 0 & 0 & 0 \\ 0 & 0 & E_{33}\big(1 - d_f d_m v_{12} v_{21}\big) & 0 & 0 & 0 \\ 0 & 0 & 0 & \Delta d_f d_m G_{12} & 0 & 0 \\ 0 & 0 & 0 & 0 & \Delta d_f d_m G_{23} & 0 \\ 0 & 0 & 0 & 0 & 0 & \Delta d_f d_m G_{31} \end{bmatrix} \end{aligned}$$

$$\begin{cases} d_f = \big(1 - d_{ft}\big)\big(1 - d_{fc}\big) \\ d_m = (1 - S_{mt} d_{mt})(1 - S_{mc} d_{mc}) \\ \Delta = 1 - d_f d_m v_{12} v_{21} - d_m v_{23} v_{32} - d_f v_{13} v_{31} - 2 d_f d_m v_{21} v_{32} v_{13} \end{cases}$$

S_{mt} and S_{mc} are coefficients used to control the shear stiffness loss, respectively set at 0.9 and 0.5 in this study.

Appendix C: Modelling Data for Chapter 5_Abaqus VUMAT 3D Hashin Criteria Code

---

```
      subroutine vumat (
c Read only -
     1 nblock, ndir, nshr, nstatev, nfieldv, nprops, lanneal,
     2 stepTime, totalTime, dt, cmname, coordMp, charLength,
     3 props, density, strainInc, relSpinInc,
     4 tempOld, stretchOld, defgradOld, fieldOld,
     5 stressOld, stateOld, enerInternOld, enerInelasOld,
     6 tempNew, stretchNew, defgradNew, fieldNew,
c Write only -
     7 stressNew, stateNew, enerInternNew, enerInelasNew )
c
      include 'vaba_param.inc'
c
c 3D Orthotropic Elasticity with Hashin 3d Failure criterion
c
c The state variables are stored as:
c state(*,1) = material point status
c state(*,2:7) = damping stresses
c
c User defined material properties are stored as
c * First line:
c props(1) --> Young's modulus in 1-direction, E1
c props(2) --> Young's modulus in 2-direction, E2
c props(3) --> Young's modulus in 3-direction, E3
c props(4) --> Poisson's ratio, nu12
```

```
c props(5) --> Poisson's ratio, nu13
c props(6) --> Poisson's ratio, nu23
c props(7) --> Shear modulus, G12
c props(8) --> Shear modulus, G13
c
c * Second line:
c props(9) --> Shear modulus, G23
c props(10) --> beta damping parameter
c props(11) --> "not used"
c props(12) --> "not used"
c props(13) --> "not used"
c props(14) --> "not used"
c props(15) --> "not used"
c props(16) --> "not used"
c
c * Third line:
c props(17) --> Ultimate tens stress in 1-direction, sigu1t
c props(18) --> Ultimate comp stress in 1-direction, sigu1c
c props(19) --> Ultimate tens stress in 2-direction, sigu2t
c props(20) --> Ultimate comp stress in 2-direction, sigu2c
c props(21) --> Ultimate tens stress in 2-direction, sigu3t
c props(22) --> Ultimate comp stress in 2-direction, sigu3c
c props(23) --> "not used"
c props(24) --> "not used"
c
c * Fourth line:
c props(25) --> Ultimate shear stress, sigu12
```

```
c props(26) --> Ultimate shear stress, sigu13
c props(27) --> Ultimate shear stress, sigu23
c props(28) --> "not used"
c props(29) --> "not used"
c props(30) --> "not used"
c props(31) --> "not used"
c props(32) --> "not used"
c

      dimension props(nprops), density(nblock),
     1 coordMp(nblock,*),
     2 charLength(*), strainInc(nblock,ndir+nshr),
     3 relSpinInc(nblock, nshr), tempOld(nblock),
     4 stretchOld(nblock,ndir+nshr), defgradOld(nblock,ndir+nshr+nshr),
     5 fieldOld(nblock,nfieldv), stressOld(nblock,ndir+nshr),
     6 stateOld(nblock,nstatev), enerInternOld(nblock),
     7 enerInelasOld(nblock), tempNew(*),
     8 stretchNew(nblock,ndir+nshr), defgradNew(nblock,ndir+nshr+nshr),
     9 fieldNew(nblock,nfieldv), stressNew(nblock,ndir+nshr),
     1 stateNew(nblock, nstatev),
     2 enerInternNew(nblock), enerInelasNew(nblock)
*
      character*80 cmname
*
      parameter( zero = 0.d0, one = 1.d0, two = 2.d0, half = .5d0 )
*
      parameter(
```

```
     * i_svd_DmgFiberT = 1,
     * i_svd_DmgFiberC = 2,
     * i_svd_DmgMatrixT = 3,
     * i_svd_DmgMatrixC = 4,
     * i_svd_statusMp = 5,
     * i_svd_dampStress = 6,
c * i_svd_dampStressXx = 6,
c * i_svd_dampStressYy = 7,
c * i_svd_dampStressZz = 8,
c * i_svd_dampStressXy = 9,
c * i_svd_dampStressYz = 10,
c * i_svd_dampStressZx = 11,
     * i_svd_Strain = 12,
c * i_svd_StrainXx = 12,
c * i_svd_StrainYy = 13,
c * i_svd_StrainZz = 14,
c * i_svd_StrainXy = 15,
c * i_svd_StrainYz = 16,
c * i_svd_StrainZx = 17,
     *n_svd_required = 17)
*
      parameter(
     * i_s33_Xx = 1,
     * i_s33_Yy = 2,
     * i_s33_Zz = 3,
     * i_s33_Xy = 4,
     * i_s33_Yz = 5,
```

```
     * i_s33_Zx = 6 )
*
* Structure of property array
      parameter (
     * i_pro_E1 = 1,
     * i_pro_E2 = 2,
     * i_pro_E3 = 3,
     * i_pro_nu12 = 4,
     * i_pro_nu13 = 5,
     * i_pro_nu23 = 6,
     * i_pro_G12 = 7,
     * i_pro_G13 = 8,
     * i_pro_G23 = 9,
*
     * i_pro_beta = 10,
*
     * i_pro_sigu1t = 17,
     * i_pro_sigu1c = 18,
     * i_pro_sigu2t = 19,
     * i_pro_sigu2c = 20,
     * i_pro_sigu3t = 21,
     * i_pro_sigu3c = 22,
     * i_pro_sigu12 = 25,
     * i_pro_sigu13 = 26,
     * i_pro_sigu23 = 27 )
* Temporary arrays
      dimension eigen(maxblk*3)
```

```
*
* Read material properties
*
      E1 = props(i_pro_E1)
      E2 = props(i_pro_E2)
      E3 = props(i_pro_E3)
      xnu12 = props(i_pro_nu12)
      xnu13 = props(i_pro_nu13)
      xnu23 = props(i_pro_nu23)
      G12 = props(i_pro_G12)
      G13 = props(i_pro_G13)
      G23 = props(i_pro_G23)
*
      xnu21 = xnu12 * E2 / E1
      xnu31 = xnu13 * E3 / E1
      xnu32 = xnu23 * E3 / E2
*
*
* Compute terms of stiffness matrix
      gg = one / ( one - xnu12*xnu21 - xnu23*xnu32 - xnu31*xnu13
     * - two*xnu21*xnu32*xnu13 )
      C11 = E1 * ( one - xnu23*xnu32 ) * gg
      C22 = E2 * ( one - xnu13*xnu31 ) * gg
      C33 = E3 * ( one - xnu12*xnu21 ) * gg
      C12 = E1 * ( xnu21 + xnu31*xnu23 ) * gg
      C13 = E1 * ( xnu31 + xnu21*xnu32 ) * gg
      C23 = E2 * ( xnu32 + xnu12*xnu31 ) * gg
```

```
*
      f1t = props(i_pro_sigu1t)
      f1c = props(i_pro_sigu1c)
      f2t = props(i_pro_sigu2t)
      f2c = props(i_pro_sigu2c)
      f3t = props(i_pro_sigu3t)
      f3c = props(i_pro_sigu3c)
      f12 = props(i_pro_sigu12)
      f13 = props(i_pro_sigu13)
      f23 = props(i_pro_sigu23)
*
      beta = props(i_pro_beta)
*
* Assume purely elastic material at the beginning of the analysis
*
      if ( totalTime .eq. zero ) then
        if (nstatev.lt.n_svd_Required) then
          call xplb_abqerr(-2, 'Subroutine VUMAT requires the '//
     * 'specification of %I state variables. Check the '//
     * 'definition of *DEPVAR in the input file.',
     * n_svd_Required,zero,' ')
          call xplb_exit
        end if
        call OrthoEla3dExp(nblock,
     * stateOld(1,i_svd_DmgFiberT),
     * stateOld(1,i_svd_DmgFiberC),
     * stateOld(1,i_svd_DmgMatrixT),
```

```
     * stateOld(1,i_svd_DmgMatrixC),
     * C11, C22, C33, C12, C23, C13, G12, G23, G13,
     * strainInc,
     * stressNew )
        return
      end if
*
* Update total elastic strain
      call strainUpdate(nblock, strainInc,
     * stateOld(1,i_svd_strain), stateNew(1,i_svd_strain) )
*
* Stress update
      call OrthoEla3dExp(nblock,
     * stateOld(1,i_svd_DmgFiberT),
     * stateOld(1,i_svd_DmgFiberC),
     * stateOld(1,i_svd_DmgMatrixT),
     * stateOld(1,i_svd_DmgMatrixC),
     * C11, C22, C33, C12, C23, C13, G12, G23, G13,
     * stateNew(1,i_svd_strain),
     * stressNew )
*
* Failure evaluation
*
      call copyr ( nblock,
     * stateOld(1,i_svd_DmgFiberT), stateNew(1,i_svd_DmgFiberT) )
      call copyr ( nblock,
     * stateOld(1,i_svd_DmgFiberC), stateNew(1,i_svd_DmgFiberC) )
```

```
      call copyr ( nblock,
     * stateOld(1,i_svd_DmgMatrixT), stateNew(1,i_svd_DmgMatrixT) )
      call copyr ( nblock,
     * stateOld(1,i_svd_DmgMatrixC), stateNew(1,i_svd_DmgMatrixC) )
      nDmg = 0
      call eig33Anal(nblock, stretchNew, eigen)
      call Hashin3d ( nblock, nDmg,
     * f1t, f2t, f3t, f1c, f2c, f3c, f12, f23, f13,
     * stateNew(1,i_svd_DmgFiberT),
     * stateNew(1,i_svd_DmgFiberC),
     * stateNew(1,i_svd_DmgMatrixT),
     * stateNew(1,i_svd_DmgMatrixC),
     * stateNew(1,i_svd_statusMp),
     * stressNew, eigen)
* -- Recompute stresses if new Damage is occurring
      if ( nDmg .gt. 0 ) then
        call OrthoEla3dExp(nblock,
     * stateNew(1,i_svd_DmgFiberT),
     * stateNew(1,i_svd_DmgFiberC),
     * stateNew(1,i_svd_DmgMatrixT),
     * stateNew(1,i_svd_DmgMatrixC),
     * C11, C22, C33, C12, C23, C13, G12, G23, G13,
     * stateNew(1,i_svd_strain),
     * stressNew )
      end if
*
* Beta damping
```

```
      if ( beta .gt. zero ) then
        call betaDamping3d(nblock,
     * beta, dt, strainInc,
     * stressOld, stressNew,
     * stateNew(1,i_svd_statusMp),
     * stateOld(1,i_svd_dampStress),
     * stateNew(1,i_svd_dampStress) )
      end if
*
* Integrate the internal specific energy (per unit mass)
*
      call EnergyInternal3d(nblock, stressOld, stressNew,
     * strainInc, density, enerInternOld, enerInternNew )
*
      return
      end

***************************************************** ***********
* OrthoEla3dExp: Orthotropic elasticity - 3d *
***************************************************** ***********
      subroutine OrthoEla3dExp (nblock,
     * dmgFiberT, dmgFiberC, dmgMatrixT, dmgMatrixC,
     * C11, C22, C33, C12, C23, C13, G12, G23, G13,
     * strain, stress )
*
      include 'vaba_param.inc'
```

```
* Orthotropic elasticity, 3D case -
*
      parameter( zero = 0.d0, one = 1.d0, two = 2.d0)
      parameter(
     * i_s33_Xx = 1,
     * i_s33_Yy = 2,
     * i_s33_Zz = 3,
     * i_s33_Xy = 4,
     * i_s33_Yz = 5,
     * i_s33_Zx = 6,
     * n_s33_Car = 6 )
*
      dimension strain(nblock,n_s33_Car),
     * dmgFiberT(nblock), dmgFiberC(nblock),
     * dmgMatrixT(nblock), dmgMatrixC(nblock),
     * stress(nblock,n_s33_Car)
* -- shear fraction in matrix tension and compression mode
      parameter ( smt = 0.9d0, smc = 0.5d0 )
*
      do k = 1, nblock
* -- Compute damaged stiffness
         dft = dmgFiberT(k)
         dfc = dmgFiberC(k)
         dmt = dmgMatrixT(k)
         dmc = dmgMatrixC(k)
         df = one - ( one - dft ) * ( one - dfc )
*
```

```
        dC11 = (one - df) * C11
        dC22 = ( one - df ) * ( one - dmt ) * ( one - dmc ) * C22
        dC33 = ( one - df ) * ( one - dmt ) * ( one - dmc ) * C33
        dC12 = ( one - df ) * ( one - dmt ) * ( one - dmc ) * C12
        dC23 = ( one - df ) * ( one - dmt ) * ( one - dmc ) * C23
        dC13 = ( one - df ) * ( one - dmt ) * ( one - dmc ) * C13
        dG12 = (one - df)
     * * ( one - smt*dmt ) * ( one - smc*dmc ) * G12
        dG23 = (one - df)
     * * ( one - smt*dmt ) * ( one - smc*dmc ) * G23
        dG13 = (one - df)
     * * ( one - smt*dmt ) * ( one - smc*dmc ) * G13
* -- Stress update
        stress(k,i_s33_Xx) = dC11 * strain(k,i_s33_Xx)
     * + dC12 * strain(k,i_s33_Yy)
     * + dC13 * strain(k,i_s33_Zz)
        stress(k,i_s33_Yy) = dC12 * strain(k,i_s33_Xx)
     * + dC22 * strain(k,i_s33_Yy)
     * + dC23 * strain(k,i_s33_Zz)
        stress(k,i_s33_Zz) = dC13 * strain(k,i_s33_Xx)
     * + dC23 * strain(k,i_s33_Yy)
     * + dC33 * strain(k,i_s33_Zz)
        stress(k,i_s33_Xy) = two * dG12 * strain(k,i_s33_Xy)
        stress(k,i_s33_Yz) = two * dG23 * strain(k,i_s33_Yz)
        stress(k,i_s33_Zx) = two * dG13 * strain(k,i_s33_Zx)
      end do
*
```

```
      return
      end

****************************************************** ***********
*strainUpdate: Update total strain*
****************************************************** ***********
      subroutine strainUpdate (nblock,
     * strainInc, strainOld, strainNew )
*
      include 'vaba_param.inc'
*
      parameter(
     * i_s33_Xx = 1,
     * i_s33_Yy = 2,
     * i_s33_Zz = 3,
     * i_s33_Xy = 4,
     * i_s33_Yz = 5,
     * i_s33_Zx = 6,
     * n_s33_Car = 6 )
*
      dimension strainInc(nblock,n_s33_Car),
     * strainOld(nblock,n_s33_Car),
     * strainNew(nblock,n_s33_Car)
*
      do k = 1, nblock
        strainNew(k,i_s33_Xx)=strainOld(k,i_s33_Xx)
     * + strainInc(k,i_s33_Xx)
```

```
        strainNew(k,i_s33_Yy)=strainOld(k,i_s33_Yy)
     * + strainInc(k,i_s33_Yy)
        strainNew(k,i_s33_Zz)=strainOld(k,i_s33_Zz)
     * + strainInc(k,i_s33_Zz)
        strainNew(k,i_s33_Xy)=strainOld(k,i_s33_Xy)
     * + strainInc(k,i_s33_Xy)
        strainNew(k,i_s33_Yz)=strainOld(k,i_s33_Yz)
     * + strainInc(k,i_s33_Yz)
        strainNew(k,i_s33_Zx)=strainOld(k,i_s33_Zx)
     * + strainInc(k,i_s33_Zx)
      end do
*
      return
      end

************************************************************* ***********
* Hashin3d w/ Modified Puck: Evaluate Hashin 3d failure *
* criterion for fiber, Puck for matrix *
************************************************************* ***********
      subroutine Hashin3d ( nblock, nDmg,
     * f1t, f2t, f3t, f1c, f2c, f3c, f12, f23, f13,
     * dmgFiberT, dmgFiberC, dmgMatrixT, dmgMatrixC,
     * statusMp, stress, eigen)
*
      include 'vaba_param.inc'

      parameter( zero = 0.d0, one = 1.d0, half = 0.5d0, three =3.d0 )
```

```
      parameter(
     * i_s33_Xx = 1,
     * i_s33_Yy = 2,
     * i_s33_Zz = 3,
     * i_s33_Xy = 4,
     * i_s33_Yz = 5,
     * i_s33_Zx = 6,
     * n_s33_Car = 6 )
*
      parameter(i_v3d_X=1, i_v3d_Y=2, i_v3d_Z=3 )
      parameter(n_v3d_Car=3)
*
      parameter ( eMax = 1.00d0, eMin = -0.8d0 )
*
      dimension dmgFiberT(nblock), dmgFiberC(nblock),
     * dmgMatrixT(nblock), dmgMatrixC(nblock),
     * stress(nblock,n_s33_Car),
     * eigen(nblock,n_v3d_Car),
     * statusMp(nblock)
*
      f1tInv = zero
      f2tInv = zero
      f3tInv = zero
      f1cInv = zero
      f2cInv = zero
      f3cInv = zero
      f12Inv = zero
```

```
      f23Inv = zero
      f13Inv = zero
*
      if ( f1t .gt. zero ) f1tInv = one / f1t
      if ( f2t .gt. zero ) f2tInv = one / f2t
      if ( f3t .gt. zero ) f3tInv = one / f3t
      if ( f1c .gt. zero ) f1cInv = one / f1c
      if ( f2c .gt. zero ) f2cInv = one / f2c
      if ( f3c .gt. zero ) f3cInv = one / f3c
      if ( f12 .gt. zero ) f12Inv = one / f12
      if ( f23 .gt. zero ) f23Inv = one / f23
      if ( f13 .gt. zero ) f13Inv = one / f13
*
      do k = 1, nblock
        if ( statusMp(k).eq.one ) then
*
        lFail = 0
*
        s11 = stress(k,i_s33_Xx)
        s22 = stress(k,i_s33_Yy)
        s33 = stress(k,i_s33_Zz)
        s12 = stress(k,i_s33_Xy)
        s23 = stress(k,i_s33_Yz)
        s13 = stress(k,i_s33_Zx)
*
* Evaluate Fiber modes
        if ( s11 .gt. zero ) then
```

```
* -- Tensile Fiber Mode
        rft = (s11*f1tInv )**2 + (s12*f12Inv )**2 + (s13*f13Inv )**2
        if ( rft .ge. one ) then
          lDmg = 1
          dmgFiberT(k) = one
        end if
      else if ( s11 .lt. zero ) then
* -- Compressive Fiber Mode
        rfc = abs(s11) * f1cInv
        if ( rfc .ge. one ) then
          lDmg = 1
          dmgFiberC(k) = one
        end if
      end if
*
* Evaluate Matrix Modes
      if ( ( s22 + s33 ) .gt. zero ) then
* -- Tensile Matrix mode
        rmt = ( s11 * half * f1tInv )**2
     * + ( s22**2 * abs(f2tInv * f2cInv) )
     * + ( s12 * f12Inv )**2
     * + ( s22 * (f2tInv + f2cInv) )
        if ( rmt .ge. one ) then
          lDmg = 1
          dmgMatrixT(k) = one
        end if
      else if ( ( s22 + s33 ) .lt. zero ) then
```

```
* -- Compressive Matrix Mode
            rmc = ( s11 * half * f1tInv )**2
     * + ( s22**2 * abs(f2tInv * f2cInv) )
     * + ( s12 * f12Inv )**2
     * + ( s22 * (f2tInv + f2cInv) )
            if ( rmc .ge. one ) then
               lDmg = 1
               dmgMatrixC(k) = one
            end if
         end if
*
         eigMax=max(eigen(k,i_v3d_X),eigen(k,i_v3d_Y),eigen(k,i_v3d_Z))
         eigMin=min(eigen(k,i_v3d_X),eigen(k,i_v3d_Y),eigen(k,i_v3d_Z))
         enomMax = eigMax - one
         enomMin = eigMin - one
*
         if ( enomMax .gt. eMax .or.
     * enomMin .lt. eMin .or.
     * dmgFiberT(k).eq.one ) then
            statusMp(k) = zero
         end if
*
         nDmg = nDmk + lDmg
*
         end if
*
      end do
```

```
*
      return
      end


************************************************** **********
* beta Damping: Add beta damping *
************************************************** **********
      subroutine betaDamping3d (nblock,
     * beta, dt, strainInc, sigOld, sigNew,
     * statusMp, sigDampOld, sigDampNew )
*
      include 'vaba_param.inc'
*
      parameter(
     * i_s33_Xx = 1,
     * i_s33_Yy = 2,
     * i_s33_Zz = 3,
     * i_s33_Xy = 4,
     * i_s33_Yz = 5,
     * i_s33_Zx = 6,
     * n_s33_Car = 6 )
*
      dimension sigOld(nblock,n_s33_Car),
     * sigNew(nblock,n_s33_Car),
     * strainInc(nblock,n_s33_Car),
     * statusMp(nblock),
```

```
     * sigDampOld(nblock,n_s33_Car),
     * sigDampNew(nblock,n_s33_Car)
*
      parameter ( zero = 0.d0, one = 1.d0, two=2.0d0,
     * half = 0.5d0, third = 1.d0/3.d0 )
      parameter ( small = 1.d-16 )
*
      betaddt = beta / dt
*
      do k =1 , nblock
        sigDampNew(k,i_s33_Xx) = betaddt * statusMp(k) *
     * ( sigNew(k,i_s33_Xx)
     * - ( sigOld(k,i_s33_Xx) - sigDampOld(k,i_s33_Xx) ) )
        sigDampNew(k,i_s33_Yy) = betaddt * statusMp(k) *
     * ( sigNew(k,i_s33_Yy)
     * - ( sigOld(k,i_s33_Yy) - sigDampOld(k,i_s33_Yy) ) )
        sigDampNew(k,i_s33_Zz) = betaddt * statusMp(k) *
     * ( sigNew(k,i_s33_Zz)
     * - ( sigOld(k,i_s33_Zz) - sigDampOld(k,i_s33_Zz) ) )
        sigDampNew(k,i_s33_Xy) = betaddt * statusMp(k) *
     * ( sigNew(k,i_s33_Xy)
     * - ( sigOld(k,i_s33_Xy) - sigDampOld(k,i_s33_Xy) ) )
        sigDampNew(k,i_s33_Yz) = betaddt * statusMp(k) *
     * ( sigNew(k,i_s33_Yz)
     * - ( sigOld(k,i_s33_Yz) - sigDampOld(k,i_s33_Yz) ) )
        sigDampNew(k,i_s33_Zx) = betaddt * statusMp(k) *
     * ( sigNew(k,i_s33_Zx)
```

```
     * - ( sigOld(k,i_s33_Zx) - sigDampOld(k,i_s33_Zx) ) )
*
        sigNew(k,i_s33_Xx) = sigNew(k,i_s33_Xx)+sigDampNew(k,i_s33_Xx)
        sigNew(k,i_s33_Yy) = sigNew(k,i_s33_Yy)+sigDampNew(k,i_s33_Yy)
        sigNew(k,i_s33_Zz) = sigNew(k,i_s33_Zz)+sigDampNew(k,i_s33_Zz)
        sigNew(k,i_s33_Xy) = sigNew(k,i_s33_Xy)+sigDampNew(k,i_s33_Xy)
        sigNew(k,i_s33_Yz) = sigNew(k,i_s33_Yz)+sigDampNew(k,i_s33_Yz)
        sigNew(k,i_s33_Zx) = sigNew(k,i_s33_Zx)+sigDampNew(k,i_s33_Zx)
*
      end do
*
      return
      end

**************************************************** ***********
* EnergyInternal3d: Compute internal energy for 3d case *
**************************************************** ***********
      subroutine EnergyInternal3d(nblock, sigOld, sigNew,
     * strainInc, curDensity, enerInternOld, enerInternNew)
*
      include 'vaba_param.inc'
*
      parameter(
     * i_s33_Xx = 1,
     * i_s33_Yy = 2,
     * i_s33_Zz = 3,
     * i_s33_Xy = 4,
```

```
   * i_s33_Yz = 5,
   * i_s33_Zx = 6,
   * n_s33_Car = 6 )
*
    parameter( two = 2.d0, half = .5d0 )
*
    dimension sigOld (nblock, n_s33_Car), sigNew (nblock, n_s33_Car),
   * strainInc (nblock,n_s33_Car), curDensity (nblock),
   * enerInternOld(nblock), enerInternNew(nblock)
*
    do k = 1, nblock
      stressPower = half * (
   * ( sigOld(k,i_s33_Xx) + sigNew(k,i_s33_Xx) )
   * * ( strainInc(k,i_s33_Xx) )
   * + ( sigOld(k,i_s33_Yy) + sigNew(k,i_s33_Yy) )
   * * (strainInc(k,i_s33_Yy))
   * + ( sigOld(k,i_s33_Zz) + sigNew(k,i_s33_Zz) )
   * * (strainInc(k,i_s33_Zz))
   * + two * ( sigOld(k,i_s33_Xy) + sigNew(k,i_s33_Xy) )
   * * strainInc(k,i_s33_Xy)
   * + two * ( sigOld(k,i_s33_Yz) + sigNew(k,i_s33_Yz) )
   * * strainInc(k,i_s33_Yz)
   * + two * ( sigOld(k,i_s33_Zx) + sigNew(k,i_s33_Zx) )
   * * strainInc(k,i_s33_Zx) )
*
      enerInternNew(k) = enerInternOld(k) + stressPower/curDensity(k)
    end do
```

```
*
      return
      end

***************************************************** ***********
* CopyR: Copy from one array to another *
***************************************************** ***********
      subroutine CopyR(nCopy, from, to)
*
      include 'vaba_param.inc'
*
      dimension from(nCopy), to(nCopy)
*
      do k = 1, nCopy
        to(k) = from(k)
      end do
*
      return
      end

***************************************************** *******************
*****
* eig33Anal: Compute eigen values of a 3x3 symmetric matrix analytically *
***************************************************** *******************
*****
      subroutine eig33Anal( nblock, sMat, eigVal )
*
```

```
      include 'vaba_param.inc'
*
      parameter(i_s33_Xx=1,i_s33_Yy=2,i_s33_Zz=3 )
      parameter(i_s33_Xy=4, i_s33_Yz=5, i_s33_Zx=6 )
      parameter(i_s33_Yx=i_s33_Xy )
      parameter(i_s33_Zy=i_s33_Yz )
      parameter(i_s33_Xz=i_s33_Zx,n_s33_Car=6 )
*
      parameter(i_v3d_X=1, i_v3d_Y=2, i_v3d_Z=3 )
      parameter(n_v3d_Car=3)
*
      parameter ( zero = 0.d0, one = 1.d0, two = 2.d0,
     * three = 3.d0, half = 0.5d0, third = one / three,
     * pi23 = 2.094395102393195d0,
     * fuzz = 1.d-8,
     * preciz = fuzz * 1.d4 )
*
      dimension eigVal(nblock,n_v3d_Car), sMat(nblock,n_s33_Car)
*
      do k = 1, nblock
        sh = third*(sMat(k,i_s33_Xx)+sMat(k,i_s33_Yy)+sMat(k,i_s33_Zz))
        s11 = sMat(k,i_s33_Xx) - sh
        s22 = sMat(k,i_s33_Yy) - sh
        s33 = sMat(k,i_s33_Zz) - sh
        s12 = sMat(k,i_s33_Xy)
        s13 = sMat(k,i_s33_Xz)
        s23 = sMat(k,i_s33_Yz)
```

```
*
      fac = max(abs(s11), abs(s22), abs(s33))
      facs = max(abs(s12), abs(s13), abs(s23))
      if( facs .lt. (preciz*fac) ) then
        eigVal(k,i_v3d_X) = sMat(k,i_s33_Xx)
        eigVal(k,i_v3d_Y) = sMat(k,i_s33_Yy)
        eigVal(k,i_v3d_Z) = sMat(k,i_s33_Zz)
      else
        q = third*((s12**2+s13**2+s23**2)+half*(s11**2+s22**2+s33**2))
        fac = two * sqrt(q)
        if( fac .gt. fuzz ) then
          ofac = two/fac
        else
          ofac = zero
        end if
        s11 = ofac*s11
        s22 = ofac*s22
        s33 = ofac*s33
        s12 = ofac*s12
        s13 = ofac*s13
        s23 = ofac*s23
        r = s12*s13*s23
    * + half*(s11*s22*s33-s11*s23**2-s22*s13**2-s33*s12**2)
        if( r .ge.one-fuzz ) then
          cos1 = -half
          cos2 = -half
          cos3 = one
```

```
        else if( r .le. fuzz-one ) then
          cos1 = -one
          cos2 = half
          cos3 = half
        else
          ang = third * acos(r)
          cos1 = cos(ang)
          cos2 = cos(ang+pi23)
          cos3=-cos1-cos2
        end if
        eigVal(k,i_v3d_X) = sh + fac*cos1
        eigVal(k,i_v3d_Y) = sh + fac*cos2
        eigVal(k,i_v3d_Z) = sh + fac*cos3
      end if
    end do
*
    return
    end
```

Appendix D: Some Results from the Modelling Chapter

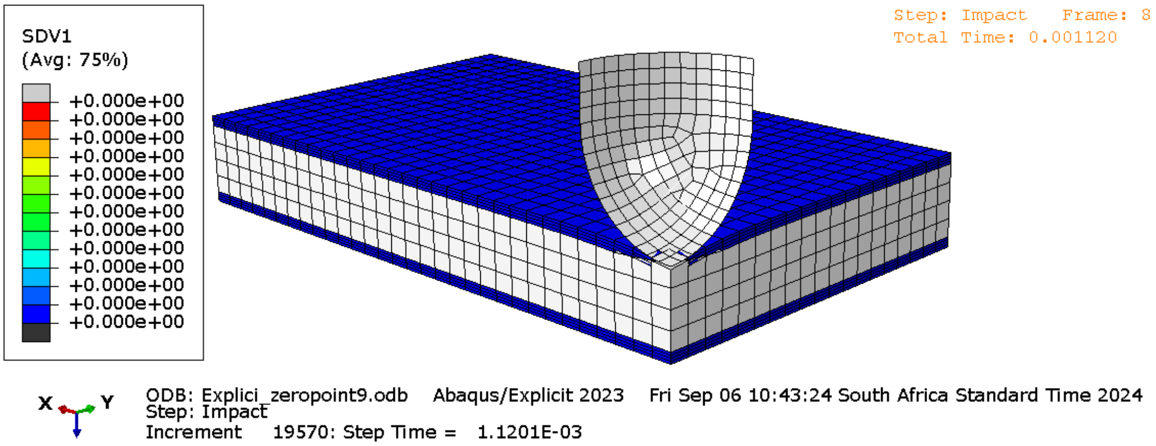

Figure D1: SDV1 at initial velocity

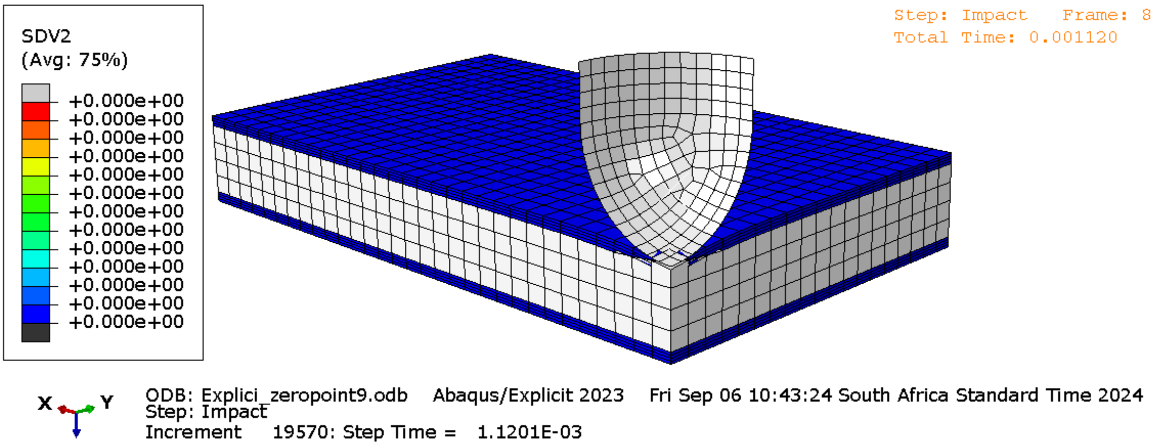

Figure D2: SDV2 at initial velocity

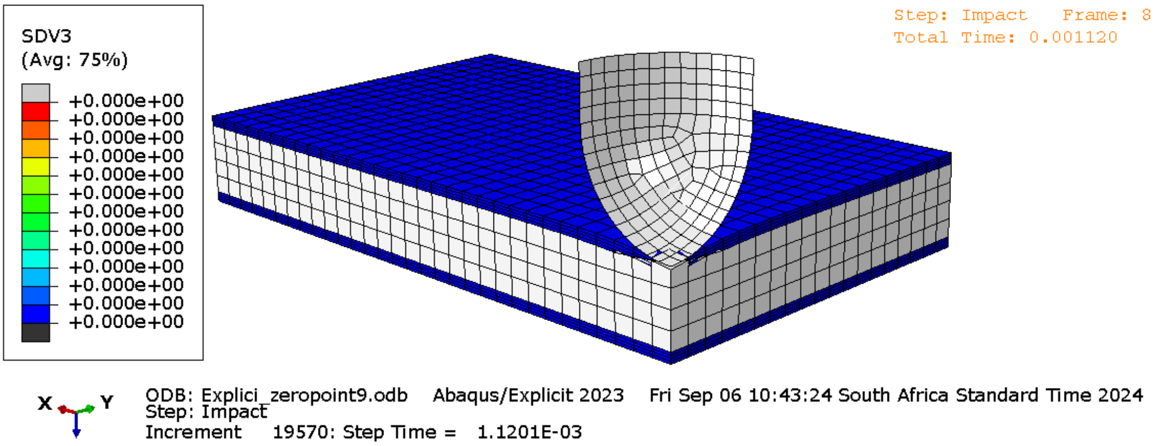

Figure D3: SDV3 at initial velocity

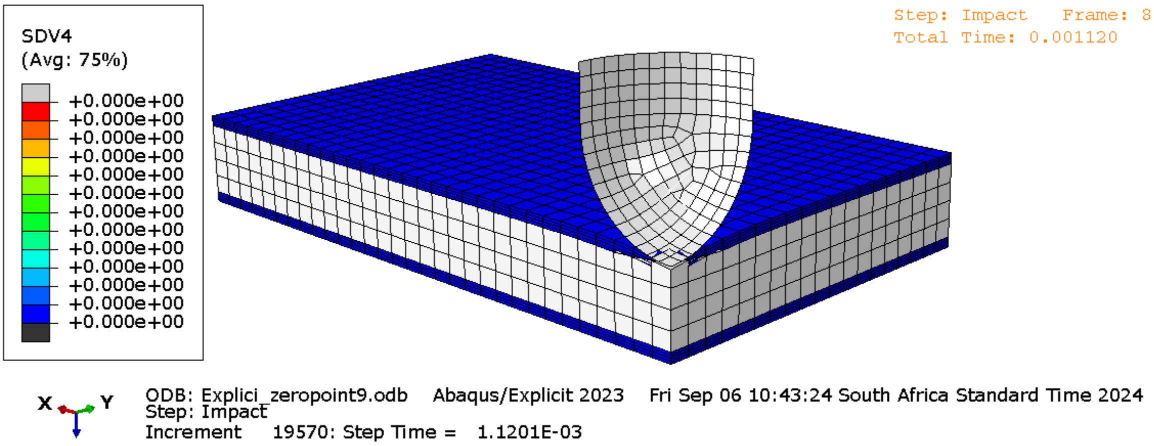

Figure D4: SDV4 at initial velocity

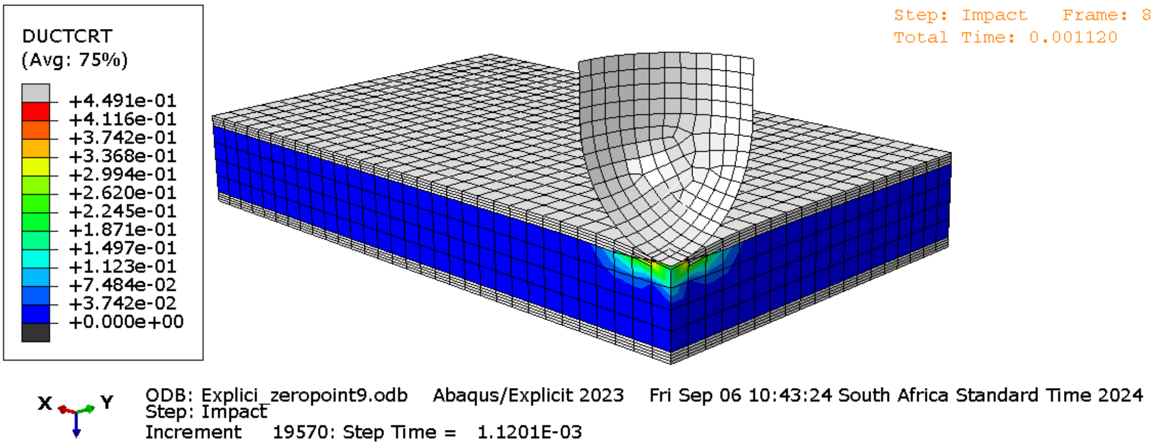

Figure D5: Ductile damage state of the foam core at initial velocity

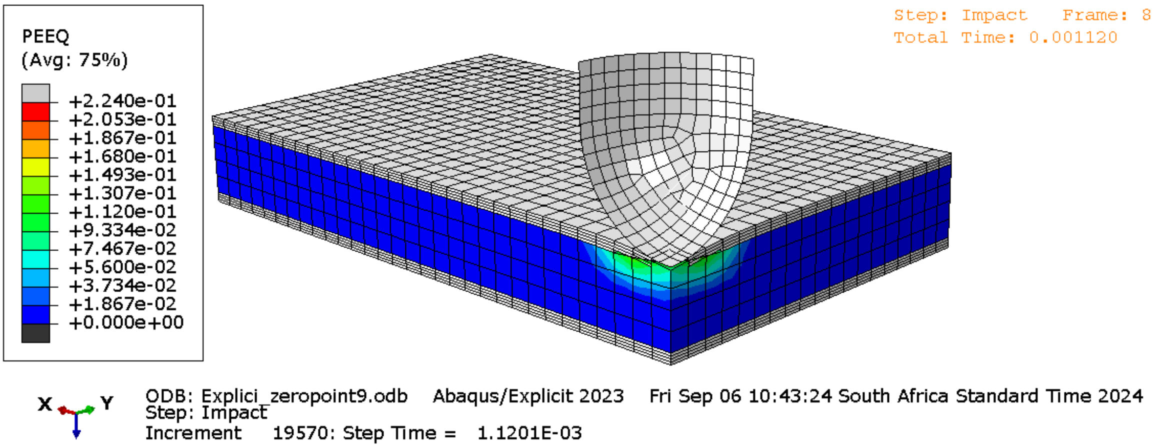

Figure D6: Plastic Strain Equivalent (PEEQ) of the foam core at initial velocity

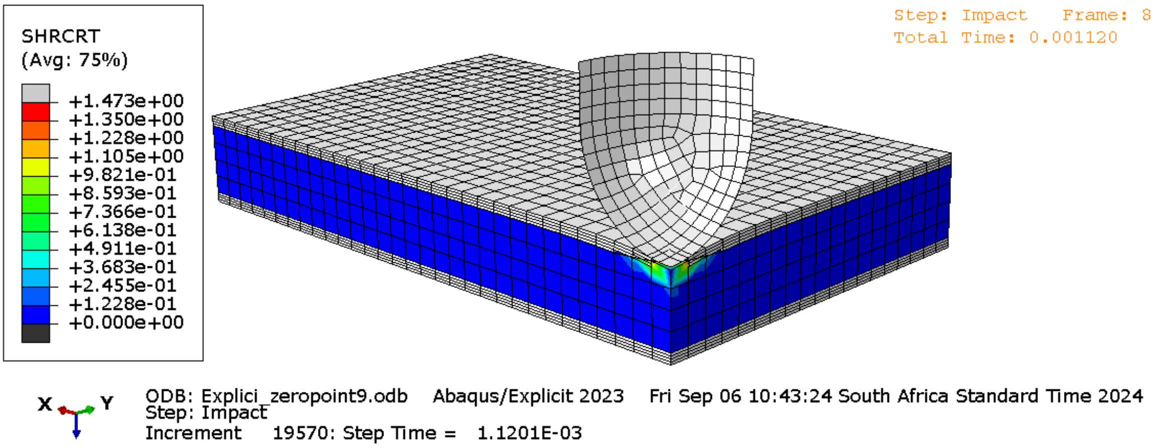

Figure D7: Shear damage state of the foam core at initial velocity

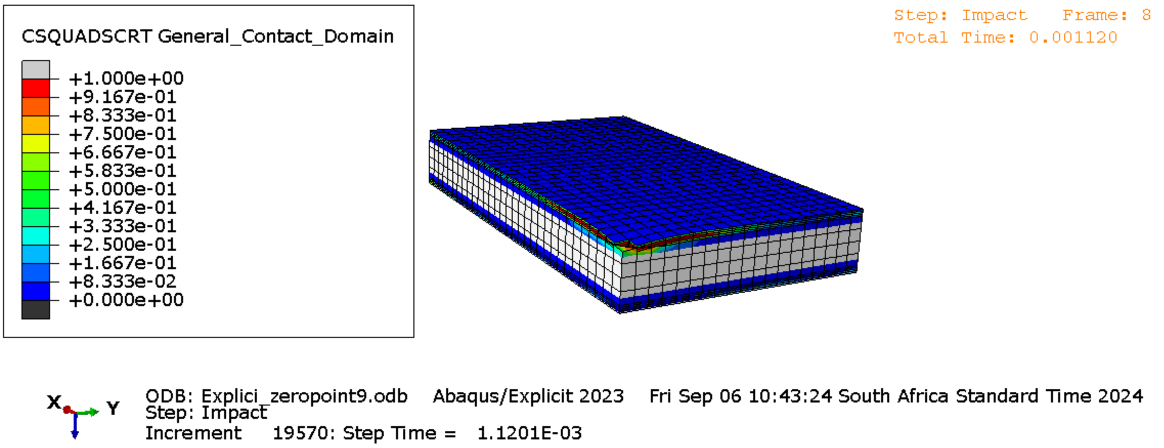

Figure D8: Cohesive failure state of the laminates at initial velocity

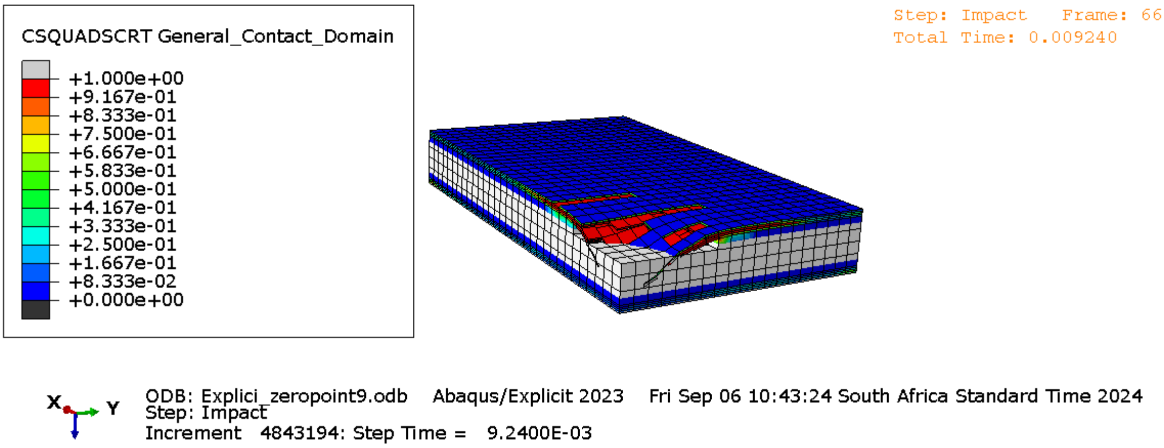

Figure D9: Damaged state with element deletion